UNIVERSITÀ
degli STUDI
di CATANIA

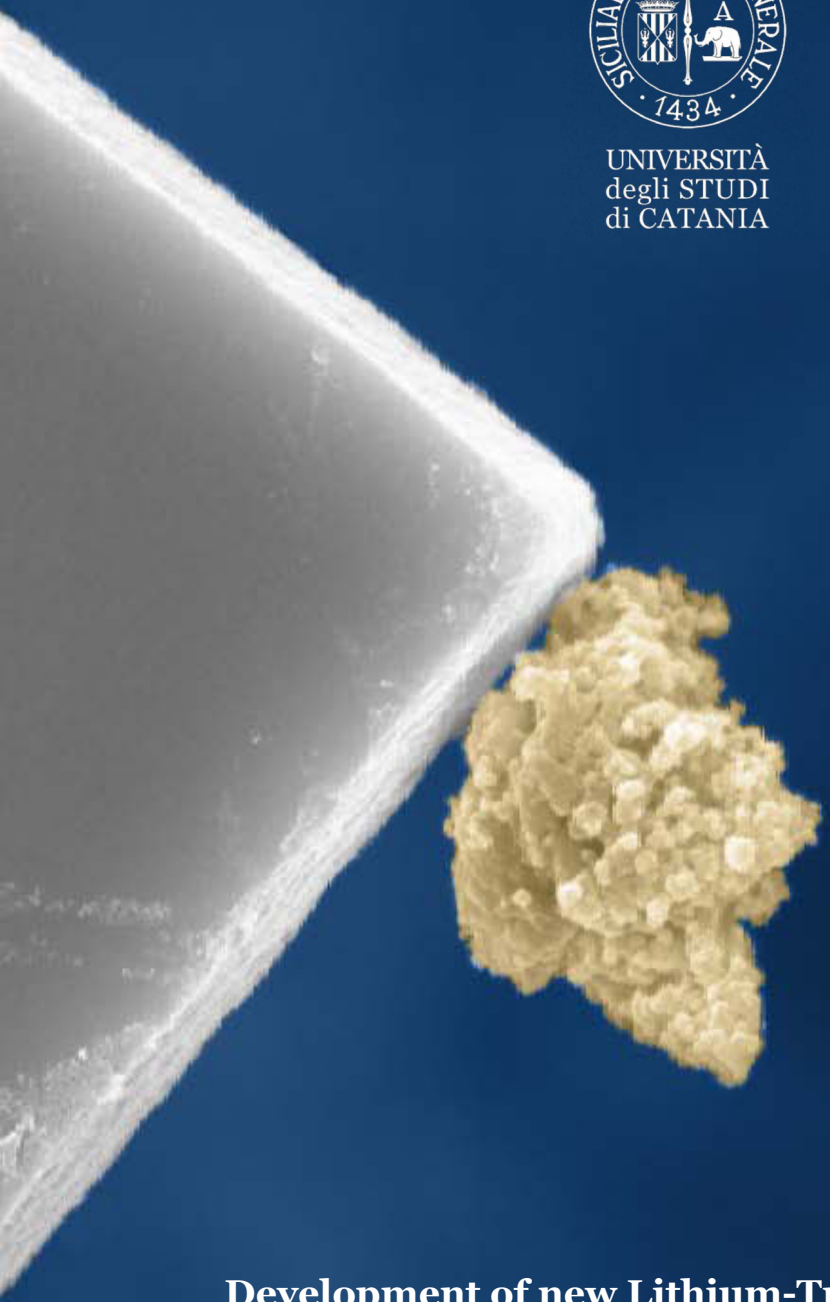

ENRICO GRECO
PhD Dissertation

Prof. Enrico Ciliberto
Supervisor

Prof. Salvatore Sortino
PhD Coordinator

Development of new Lithium-Transition Metals co-doped Nanotitania. A perspective for sustainable photocatalytic materials and a comparative study between benefits and health risks.

International PhD in Chemical Sciences - XXX Cycle
2014-2017

Froh, wie seine Sonnen fliegen
Durch des Himmels prächt'gen Plan,
Laufet, Brüder, eure Bahn,
Freudig, wie ein Held zum Siegen.

(Friedrich Schiller)

UNIVERSITÀ
degli STUDI
di CATANIA

Department of Chemical Sciences

International PhD in Chemical Sciences XXX Cycle

ENRICO GRECO

Development of new Lithium-Transition Metals co-doped Nanotitania. A perspective for sustainable photocatalytic materials and a comparative study between benefits and health risks.

PhD Dissertation

PhD Coordinator:
Prof. S. Sortino

Supervisor:
Prof. E. Ciliberto

ACADEMIC CYCLE 2014-2017

Doctor of Philosophy Dissertation
International PhD in Chemical Sciences, XXX Cycle, 2014-2017
Development of new Lithium-Transition Metals co-doped Nanotitania. A perspective for sustainable photocatalytic materials and a comparative study between benefits and health risks.
ENRICO GRECO

Department of Chemical Sciences,
Viale Andrea Doria, 6-I,
95125, Catania (CT) - Italy
Tel. +39 095 7395115
www.dipchi.unict.it

Archived on Open Access Institutional Archive of University of Catania using DSpace open source repository application http://dspace.unict.it/

Cover: *False colored SEM image of an agglomerate of titanium dioxide nanoparticles doped with lithium and cobalt on anatase crystal.* © Enrico Greco 2015

Reviewed and approved by:

Prof. Örjan Hansson (mid-term thesis review)
University of Gothenburg (Sweden), Department of Chemistry and Molecular Biology
orjan.hansson@chem.gu.se

Prof. Geoffrey Allen
University of Bristol (UK), School of Physics
g.c.allen@bristol.ac.uk

Prof. Renzo Bertoncello
University of Padua (Italy), Department of Chemical Sciences
renzo.bertoncello@unipd.it

Prof. Abdessadek Lachgar
Wake Forest University (US), Chemistry Department
lachgar@wfu.edu

Prof. Jing Shang
Peking University (China), College of Environmental Sciences and Engineering
shangjing@pku.edu.cn

Prof. Stéphane Viel
Aix-Marseille Université (France), Department of Chemistry - Institute of Radical Chemistry
s.viel@univ-amu.fr

Table of contents

Abstract

During this century, rapid population growth has led to an increased exploitation of oil and nuclear power to satisfy energy demands. This situation has created a growing tension between the deteriorating condition of the natural environment and the needs of society. Several research projects have sought to improve the situation through the development of innovative products and eco-friendly technologies: for example, the purification of the gaseous emissions emitted by industrial sources, or the manufacture of vehicles using sunlight as a renewable and clean energy. In addition, newly created materials are able to reduce air pollutants (organic and inorganic) through the process of photocatalysis, which consists

of using solid semiconductors able to oxidize harmful substances until complete mineralization. In this context, the production of photocatalytic building materials could constitute a very interesting solution, and become an integral part of the strategy to reduce environmental pollution. Titanium dioxide (TiO_2) is one of the most common photocatalytic materials. It can be used in many fields of application, including the building industry. The combination of titanium dioxide with cement makes it possible to obtain a binder that has both traditional properties, such as mechanical strength and durability, and new properties allowing the preservation of the environment and the conservation of the aesthetic value of the buildings. For instance, researchers have managed to create a material capable of accelerating the oxidation of the organic pollutants that are deposited on the external walls of the buildings.

This dissertation focused on the design, synthesis and characterization of a new family of titanium dioxide 1D, 2D and 3D nano-systems, doped with lithium and some transition metals in order to decrease the band gap and to enable visible light photoactivation even in indoor conditions.

All materials were studied by different techniques. Brunauer–Emmett–Teller (BET) method was used in order to obtain relative surface areas. When compared with the standard samples, the NPs samples showed an increment of the relative surface areas that was better than the increments observed in all the nanosheet samples (446 m^2/g^{-1}). The use of lithium, cobalt, cerium, and tungsten ions as dopants was evaluated through the UV-Vis absorption technique. The results showed both an increased absorption in the visible range and a decrease of band gap for the doped samples in comparison to the sample of pure TiO_2.

We used several methods to evaluate the photocatalytic efficiency of all the nanoparticles and nanosheets we produced. The Li-Co and Li-Ce doped nanoparticles showed very good results both in water solution and in gas phase. The photocatalytic activity of our nanosystems was comparable with the standard samples under UVb light, but the doped NPs, in particular those doped with Au@TiLi(5) and TiLi(5)Co(5), showed better results under visible light than the control samples. In conclusion, the NP and nanosheet materials we produced may be very good candidates for use under visible light.

Our new synthesis method achieved very interesting results. It allowed us to obtain nanoparticles, nanosheets, xerogels, and aerogels covered with Li^+ ions in place of the H^+ ion at the surface in order to maintain them in a good dispersion in solution. In effect, it has been shown that lithium ions are able to maintain nanoparticles in dispersion by electrostatic repulsion. Furthermore, it has been shown that lithium ions have a higher mobility than H^+ ions at the surface of nanoparticles. Lithium can also be considered as a dopant because it reduces the energy gap of the system.

In order to evaluate the toxicity of the NPs, a comparative study on human lung cells and E. coli cells was carried out in vitro. All the analyzed nanoparticles exhibited different photocatalytic activities for human cells and bacteria, in particular under irradiation. Some transition metal ions doped nanoparticles exhibited cytotoxicity even in absence of illumination, a phenomenon that was probably caused by their dopant content. The use of such systems could constitute a risk for human health; however, once inhaled, the lack of illumination within the human body could reduce such a risk, and for TiLi and Au@TiLi(5) groups the danger is virtually absent. The toxicity on Escherichia coli cells is significantly higher in almost all

cases. In the case of the TiLiCo group, in particular, there is a high contrast between the low toxicity for human cells and the high toxicity for *Escherichia coli*. This can suggest the possible use of this material as a bactericide in biological contaminated contexts. These nanosystems are very effective as photocatalysts or bactericidal systems, but require the inclusion of an adequate nano-filtration device at the exit of the reaction chambers to prevent the dispersion of nanoparticles in the environment.

Finally, I can say that the production of the new Li-M co-doped TiO_2 family, active under visible light, represents a remarkable advancement in this area of research.

Preface

In recent years, global population has contributed to the rising demand for housing units, energy, food, and soil. According to demographic forecasts made by the United Nations, the world population could reach 9.8 billion people by 2050, mostly clustered in urban areas [1]. This demographic boom will increase the demand for basic goods. The building materials industry is highly energy intensive; its large consumption of fossil fuels contributes to the release of many pollutants, including CO_2 SO_X NO_X, particulates and heavy metals [2]. Consequently, along with transportation and energy sectors, the construction industry is identified as one of the major contributors to greenhouse gas (GHG) emissions and pollutants [3]. Therefore, in the next few years, new energy

strategies, together with new materials, and new process designs, will have to be devised in order to take up these new challenges.

In architecture, great strides have been made towards the functionality of materials. In this field, the primary objective is the development and use of smart materials that require less energy to be produced, assembled, and maintained. Promising results have already been achieved concerning the use of photocatalyzers, which constitute self-cleaning and self-healing materials [4].

The development and application of nano-engineered surface treatments on outdoor materials will become a useful tool for smart systems to better preserve and maintain architectural surfaces. So far, strategies and routes to reach these goals have often employed new nanotechnologies. Titanium dioxide nanoparticles can be used as transparent, self-cleaning coatings applied directly on pre-existing surfaces, limiting cleaning actions and maintenance processes, thus reducing their costs. This self-cleaning ability is due to photo-induced hydrophilicity on treated surfaces. However, the high band gap of the anatase phase titanium dioxide (TiO_2) nanoparticles greatly reduces the efficiency of these systems due to the low content of UV radiation in the sun light [5].

Superhydrophilic, superhydrophobic, antifogging, and antireflective materials can be combined together to create materials with new properties [6], [7], [8].

Self-healing materials are able to partially or completely heal damage inflicted on them (in particular, crack formation) *in situ*, and to such a degree that the original functionality is restored – not necessarily the outer or inner microstructure [9], [10], [11]. The healed functionalities range from mechanical properties to aesthetics, barrier function, conductivity, optical properties, etc. Such materials would greatly improve the reliability and durability of buildings by reversing the deterioration process, once or multiple times. Self-healing ability is not limited to a specific class of materials; it is applicable to concrete, polymers (including their composites), metals, and ceramics.

Objectives

The main objectives of this project are:

(1) to study and provide a new generation of adaptive high-performance materials that can be used for various applications in

technology and buildings,

(2) to elucidate fundamental cross-disciplinary, material-independent principles and *green* design strategies,

(3) to apply this knowledge to new approaches in green design strategies in different material classes.

The research program will be devoted to the investigation of the basic principles for all classes of building materials, and for the application of new principles for the synthesis/fabrication of photocatalytic nanomaterials with anti-pollution effects. Interdisciplinary integration of the different material classes will occur in three cross-sectional areas:

- Investigation of fundamental principles

  This research will focus on the chemical and physical processes that are susceptible to lead to local healing without the subsequent intentional addition of new substances. Such processes will include chemical reactions (including, but not limited to polymerizations, redox reactions, and cross-linking reactions), phase transitions (e.g. martensitic transformation), flow and sinter processes, as well as stress relaxation.

- Production of materials (synthesis/fabrication and characterization)

  The synthesis and fabrication of different nanomaterials (1D, 2D, 3D), based on the fundamental concepts mentioned above, will be investigated. The use of bio-inspired structural models for the design of synthetic self-healing materials could be one of the challenges dealt with here. One of the main goals of this research is to investigate methods for optimizing the properties of materials (e.g. mechanical properties, conductivity, or optical properties), extending their durability, and improving their reliability under static and cyclic stress (i.e. mechanical stress, outdoor and other harmful environmental conditions). Some examples of further new systems could be: nanoparticles of TiO_2 used as hydrophilic and antipollution additive in concrete, mortars and glass; nanoparticles of $Sr(OH)_2$ used for the elimination of sulphates in indoor and outdoor materials; synthesis of superhydrophobic and superhydrophilic switching materials, using functionalized silica nanoparticles with azobenzene containing hydrophobic groups or different chains; αFe_2O_3 and γFe_2O_3 nanoparticles used as fillers for concrete and mortars in order to increase their mechanical properties,

workability, and durability; functionalized SiO_2 for the improvement of the compressive strength of self-compacting concrete.

- Targeting the requirements of potential applications.

  The second part of the research will focus on the practical requirements needed for any real world application of the concepts we mentioned earlier. Basic, common concepts will be used to design new nanomaterials for potential application in construction. The study of healing and cleaning processes will take into consideration the requirements and constraints associated with a potential application, the elaboration of strategies to ensure the production of such material is sustainable, and the selection of the material properties required for the active reduction of the pollutants.

During the first year of the PhD, we focused on points 1 and 2. After a long period of study of all the procedures that had been used so far, we proceeded to make the first set of synthesis of doped-TiO_2 NPs. We also performed all the characterizations needed to obtain information about the usability of these materials for our purposes.

During the second year of the PhD we focused on points 2 and 3. Once we had completed the study of the first set of doped-TiO_2 NPs, we made a new set with different syntheses, together with a set of doped-TiO_2 nanosheets, a set of doped-TiO_2 xerogel, and a set of doped-TiO_2 aerogel. All the materials were thoroughly studied; we also investigated their photocatalytic efficiency both in liquid and in gas phases.

During the third year, in order to validate the method, we produced a new set of NP synthesis, a set of Aerogel material, and a set of core-shell NPs. Some new synthesis modifications were experimented and the kinetics of photocatalytic processes were investigated. An in vitro comparative study about the cytotoxicity on human tissue and bacteria cells was carried out to determine any possible effect these materials might have when used in public environments, and any related risks.

During these three years, we have achieved these objectives through several national and international collaborations: in particular, in phase one, with the CNR-IMC of Rome (Dr. Donatella Capitani group and Dr. Valeria Di Tullio), the French CNRS (Dr. Fabio Ziarelli), the University of Aix-Marseille, France (Prof. Stephàne Viél group), the

Department of Environmental Sciences and Engineering of Peking University in Beijing, China (Prof. Jing Shang group), and the Department of Chemistry of University of South Florida in Tampa, United States of America (Prof. Ioannis Gelis group).

Introduction

During this century, rapid population growth has led to an increased exploitation of oil and nuclear power for energy purposes, creating a growing tension between the deteriorating condition of the natural environment and the needs of society [1]. Several research projects have sought to improve the situation through the development of innovative processes and eco-friendly technologies: for example, the purification of the gaseous emissions emitted by industrial sources, or the manufacture of vehicles using sunlight as a renewable and clean energy. In addition, newly created materials are able to reduce air pollutants (organic and inorganic) through the process of photocatalysis, which consists of using solids semiconductors able to oxidize harmful substances until complete mineralization [12] [13] [14] [15]. In this context, the photocatalysis

applied to building materials could become a very interesting solution, becoming an integral part of the strategy to reduce environmental pollution. Titanium dioxide (TiO_2) is one of the most common photocatalytic materials. It can be used in many fields of application, including the building industry. The combination of titanium dioxide with cement makes it possible to obtain a binder that has both traditional properties, such as mechanical strength and durability, and new properties allowing for the preservation of the environment and the conservation of the aesthetic value of the buildings. For instance, researchers have managed to create a material capable of accelerating the oxidation of the organic pollutants that are deposited on the external walls of the buildings [16]. Many environment friendly concrete formulations have been designed to degrade the numerous chemicals present in the air, which attack the respiratory system and leave discernible traces on buildings and monuments. The first large scale application took place in September 2002 in Milan, as 6000 square meters of road surface with a vehicle traffic rate of 1200 units/h were covered with a photo-catalytic cement. A reduction of up to 50% of the concentration of nitrogen oxides could be observed at street level during a sunny summer day, at a wind speed of less than 0.7 m/s [17]

[18]. The same results were achieved in Japan [19] and Bergamo (Italy) [20]. From 2003 to 2014, similar experiments occurred in Paris (France) [21], Athens (Greece) [22] [23], Copenhagen (Denmark) [24], Antwerp (Belgium) [25] and in particular in Rome (Italy), with the realization of the *Dives in Misericordia Church*. This building, designed by Richard Meier, consists of four large shells made of reinforced white concrete enriched with titanium, which provide a total volume of more than 20.000 m^3 [26]. Remarkably, only slight differences in color between the inner and the outer concrete walls of the building could be observed six years after the inauguration of the building [23]. Other examples of the use of titanium enriched concrete in the city of Rome include residential buildings [26] [27], as well as the *Umberto I* pilot city tunnel [28].

This type of innovative construction materials and coatings have the potential to contribute substantially to the attainment of the objective of the EU (within the EU strategy Europe2020 [29] and application of the Kyoto protocol [30] and Paris Agreement [31]) to reduce NO_x levels less than 20 ppb by 2020.

Titanium Dioxide

Titanium dioxide is an oxide semiconductor that has the appearance of a colorless crystalline powder. In natural conditions, three different mineral polymorphs exist: anatase [32], rutile [33] and brookite [34]. Anatase and rutile are the most commonly forms used in research and real-life applications. Not only are they widespread and easy to obtain, but they also possess the best photocatalytic properties. All phases of TiO_2 can be described as consisting of an arrangement of the same "building blocks": TiO_6 octohedra, where a single Ti atom is surrounded by a distorted octahedron of six O atoms. The three forms of TiO2 differ by the arrangement and the orientation of the various chains of octahedra (fig. 1).

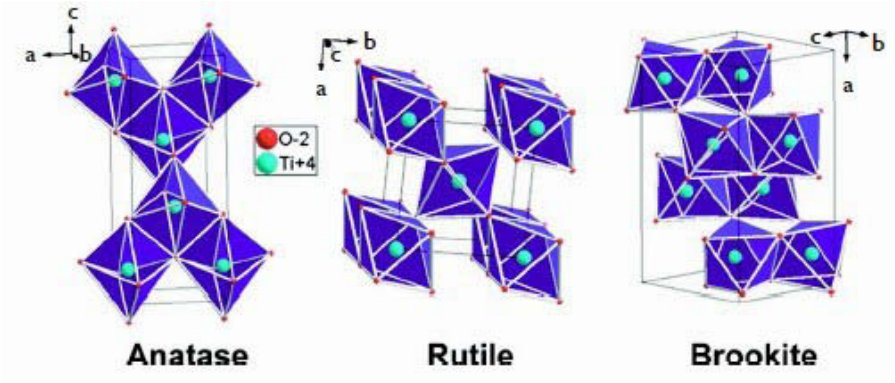

Fig. 1: Polymorphic forms of titanium dioxide: anatase, rutile and brookite.

Brookite (fig. 2) has an orthorhombic structure, each octahedron sharing three sides with neighboring units [34]. It turns into rutile at about 750° C. Its mechanical properties are similar to those of the rutile phase, but it is less common, and is seldom used commercially. Pure brookite is very difficult to synthesize, which makes it difficult to study its properties.

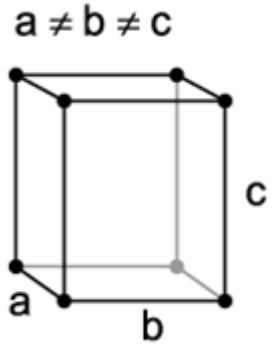

Fig. 2: Brookite structure.

Rutile (fig. 3) is the most thermodynamically stable form in natural conditions. It has a tetragonal structure in which each atom of Ti is coordinated to six O atoms by four equatorial and two longer apical bonds, forming a slightly distorted octahedron [33]. Each octahedron shares eight corners and two sides with other

octahedral units; forming a linear chain that runs parallel to the *c* axis of the unit cell, composed of two units of TiO_2.

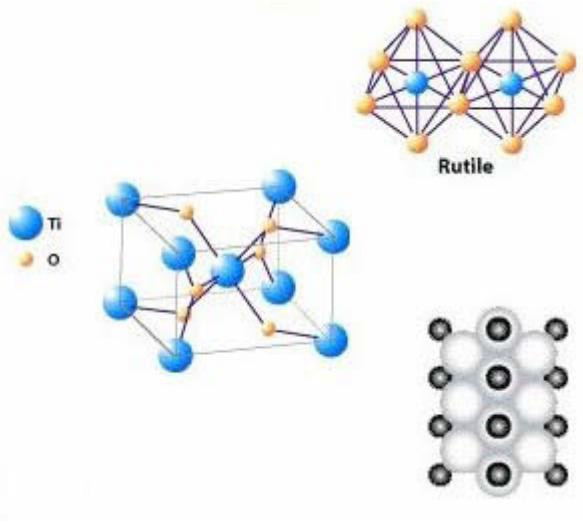

Fig. 3: Rutile structure.

Anatase (fig. 4) has a tetragonal structure; Ti and O atoms are arranged in a similar fashion to rutile [32]. However, the distortion of the TiO_6 octahedron is more pronounced. Each octahedron shares four corners and four sides with four other octahedra, forming a “Z” shaped structure perpendicular to the *c* axis. Each unit cell consists of four units of TiO_2.

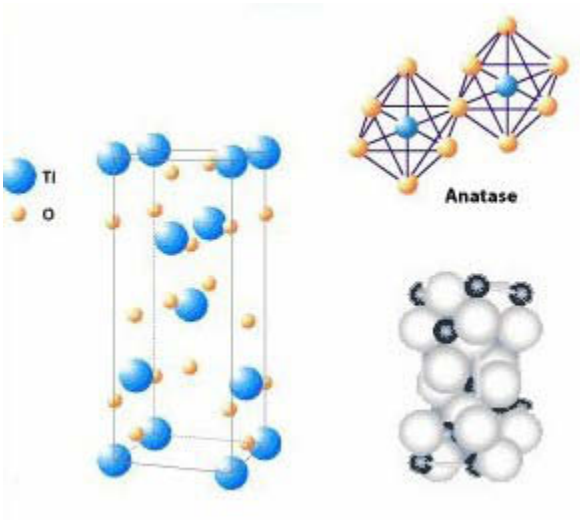

Fig. 4: Anatase structure.

Compared to rutile, anatase (fig. 5) has a closer packed structure, as the contraction of its C axis involves a contraction of the volume by about 9%. The different geometrical arrangement of the two polymorphs is reflected by their different density, with a value of 4.250 g/cm^3 for rutile and 3.899 g/cm^3 for anatase.

At all temperatures (fig. 6), at pressures up to 60 kbars, rutile is more stable than anatase, and as such, is thermodynamically favored [35].

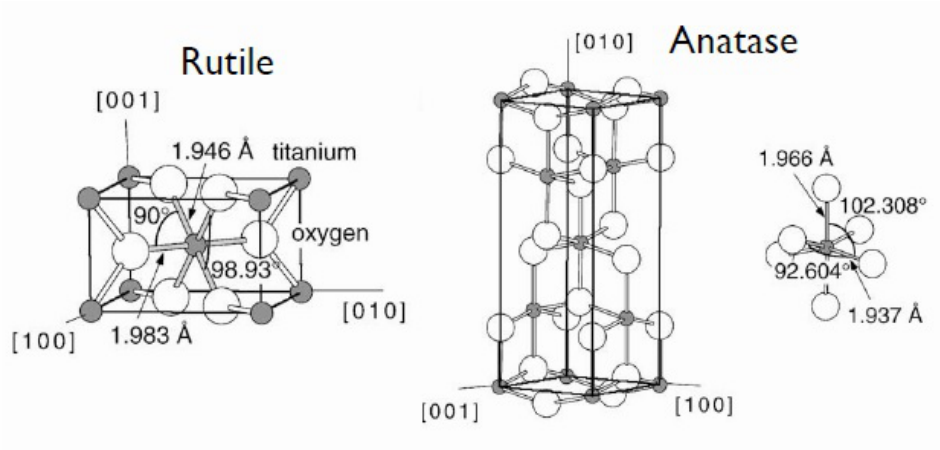

Fig. 5: Bulk structure of rutile and anatase. The tetragonal bulk unit cell of rutile has the dimensions a = b=4.857 Å, c = 2.953 Å and the one of anatase a = b = 3.782 Å, c = 9.502 Å. In both structures, slightly distorted octahedra constitute the basic building units [36].

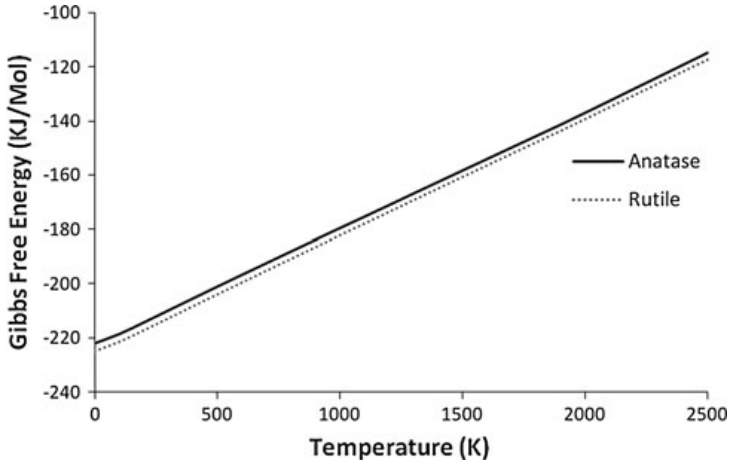

Fig. 6: Gibbs free energy for anatase and rutile versus temperature [35].

However, some synthesis techniques, which involve the use of high temperatures, have produced particles of anatase [37]. From a structural point of view, this may be due to the fact that the short-range order TiO_6 octahedra prefer the anatase phase during the formation of crystal structures, as it is less restrictive than the rutile phase, and more affine to the amorphous phase. From a thermodynamic point of view, this phenomenon is attributed to the fact that anatase, despite generally having an amount of Gibbs free energy higher than rutile, seems to have a lower amount of surface energy [35]. Since smaller particles, with a higher surface/volume ratio, make a relatively more important contribution to the total energy surface, it can be assumed that below a certain critical threshold, the size of the particles becomes a decisive factor, leading to reverse stability [38].

Lazzeri et al. [39] conducted a theoretical study on the structure and the energetic properties of some of the surfaces of anatase and rutile. In particular, in anatase, the only exposed surfaces are (101) and (001), the first being the most stable and representing more than 94% of the surface. In rutile, the exposed surfaces are (110), (101), and (100). (110) is the most stable of the three, and

constitutes more than 56% of the total surface. The crystallographic surfaces of rutile and anatase are schematized in fig. 7.

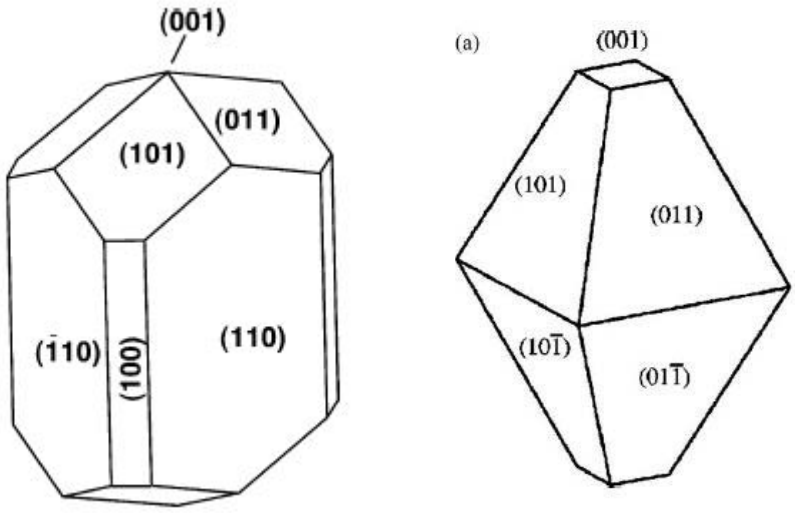

Fig. 7: Crystal surfaces of Rutile (left) and Anatase (right) [39].

Fig. 8 shows how variables such as temperature and pressure determine the existence of TiO_2 as rutile, anatase, or a mixture of both [40].

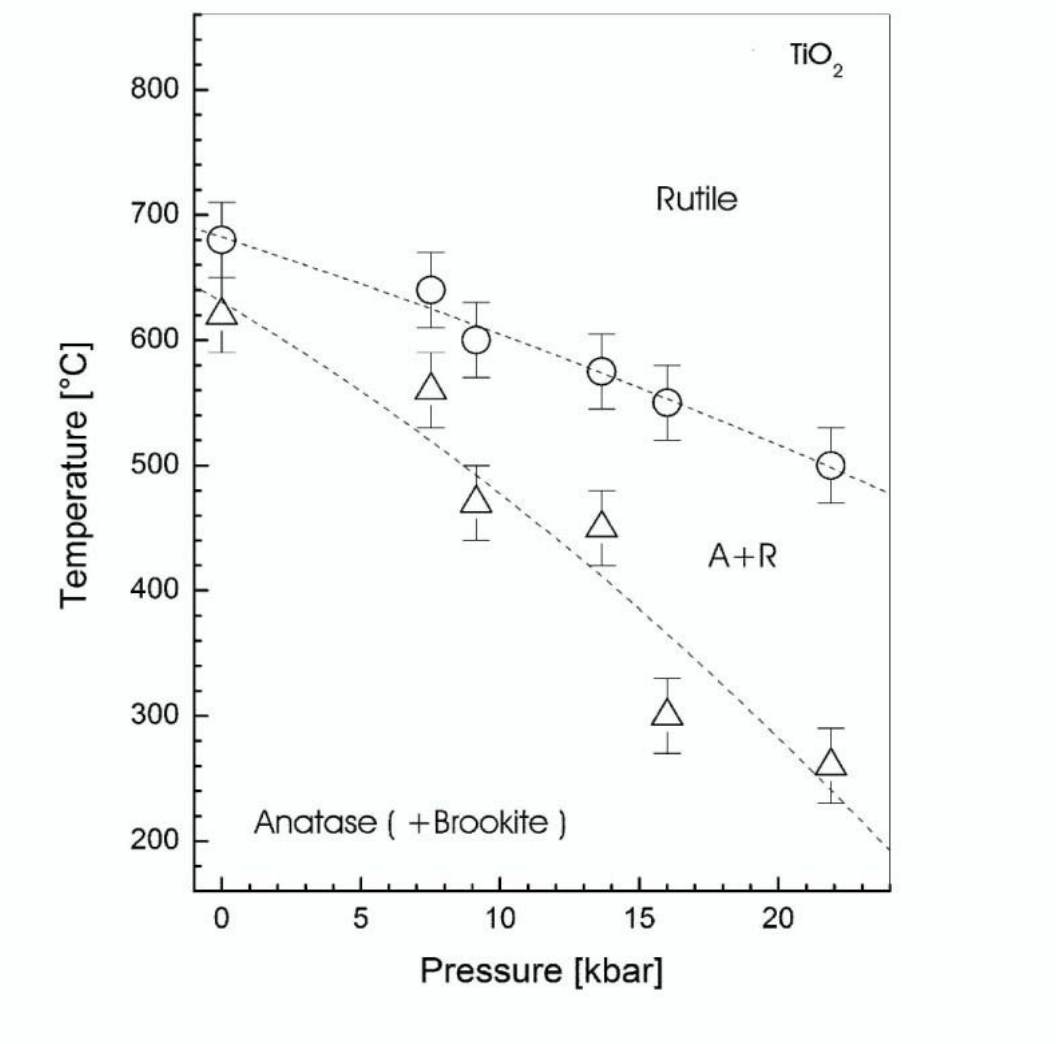

Fig. 8: The pressure–temperature phase diagram of nanocrystalline TiO_2 sol–gel powders [40].

Heterogeneous Photocatalysis

Photocatalysis is defined as the acceleration of the speed of a photoreaction due to the presence of a catalyst [14] [12] [41]. In fact, the oxidation of most of the hydrocarbons would proceed rather slowly in the absence of catalytic active substances. A photocatalyst decreases the activation energy of a given reaction. A system consists of heterogeneous photocatalytic semiconductor particles (called photocatalysts), which are in close contact with half of the reaction liquid or gas. When exposed to light, the catalysts enter an excited state, and are able to start chain processes such as redox reactions and molecular transformations [42] [43] (fig. 9).

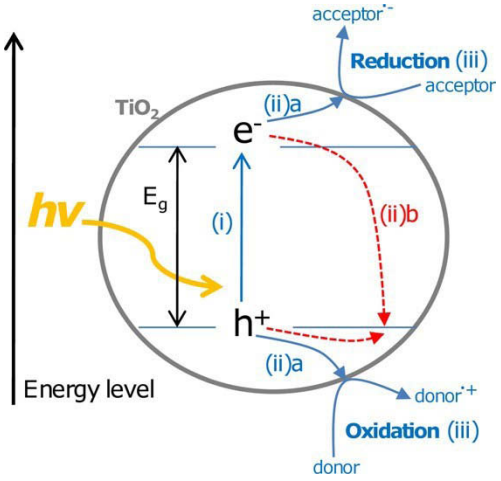

Fig. 9: Photon absorption mechanism by a particle of semiconductor: photon absorption and charge separation (i), migration of charges to the surface (ii)a or recombination of the charges (ii)b, redox reactions on the surface obtaining reducing and oxidizing species (iii) [43].

The figure above (fig. 10) depicts a simplified reaction scheme of photocatalysis. Due to their electronic structure, which is characterized by a full valence band (VB) and an empty conduction band (CB), semiconductors (metal oxides or sulfides such as ZnO, TiO_2 and ZnS) can act as sensitizers for photo-induced redox processes. The difference between the lowest energy level (LUMO) of the CB and the highest energy level (HOMO) of the VB is the so-called "energy gap" E_g. It corresponds to the minimum amount of light energy required to make the material conductive.

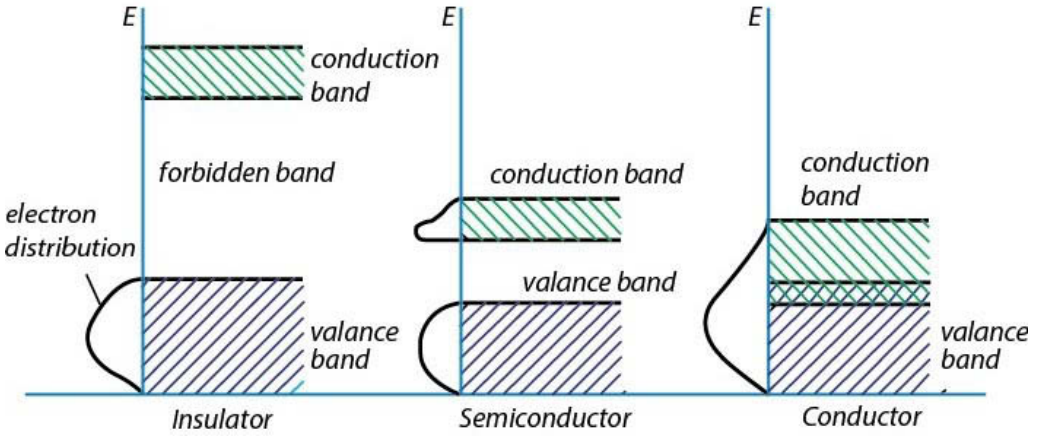

Fig. 10: Energy gap and the valence band and conduction of a semiconductor.

Mobile charge carriers can be generated by three different mechanisms: thermal excitation, photoexcitation, and doping. If the

energy gap is sufficiently small (<0.5 eV), then the thermal excitation can promote an electron from the valence band to the conduction band [44] (fig. 11). Likewise, the promotion of the electron to the conduction band can occur by absorption of a photon of light, photoexcitation, provided that hv> E_g. The third mechanism of generation of mobile charge carriers is doping. Such a charge transfer presents non-equilibrium conditions, which leads to the reduction or the oxidation of the species absorbed on the surface of the semiconductor.

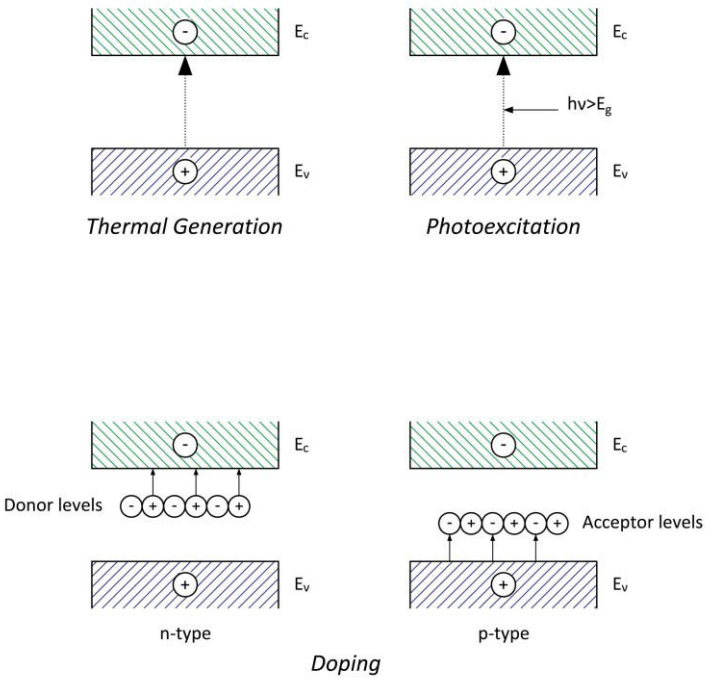

Fig. 11: The three mechanisms of generation of the charge carriers.

If the photon energy *hv* is greater than the value of E_g (energy gap), an electron (e^-) is promoted from the valence band to the conduction band, leaving behind a vacancy (h^+). In semiconductors, some of these pairs of photoexcited electron-hole spread on the surface of the catalytic particle, and take part in the chemical reaction with the molecules absorbed: donor (*D*) or acceptor (*A*) (1). TiO_2 is a semiconductor with an energy gap equal to E_g = 3.2 eV [45]; when irradiated by a photon with an amount of energy greater than E_g (shorter wavelength of 388 nm), a TiO_2 electron is able to overcome the energy gap, and is promoted from the valence band to the conduction. Consequently, the primary process is the generation of a charge carrier.

$$TiO_2 + h\nu \rightleftarrows h_{vb}^+ + e_{cb}^- \quad (1)\ [46]$$

The following reactions [46] [47] [14] [13] illustrate how the vacancies can oxidize the molecules of the donor *D* (2), while the electrons of the conduction band can reduce the molecules of the electron acceptor *A* (3).

$$D + h_{vb}^+ \rightarrow {}^{\bullet}D^+ \quad (2)$$

$$A + e_{cb}^- \rightarrow {}^{\bullet}A \quad (3)$$

A feature of semiconductors metal oxides is the strong oxidizing power of their vacancies h^+, which can react with water absorbed on their surface, as shown in reaction (4). This leads to the formation of a highly reactive hydroxyl radical ($^{\bullet}OH$). Both electron vacancies and hydroxyl radicals are strong oxidizing agents, and as such they may be used to oxidize most organic contaminants.

$$H_2O_{ads} + h_{vb}^{+} \rightarrow {}^{\bullet}OH_{ads} + H_{ads}^{+} \quad (4)$$

Reaction (5) shows how the oxygen in the air acts as an electron acceptor, leading to the formation of a super-oxide anion.

$$O_2 + e_{cb}^{-} \rightarrow {}^{\bullet}O_2{}^{-} \quad (5)$$

Superoxide anions are highly reactive particles, capable of oxidizing organic materials. For this reason, the use of TiO_2 is very important for the purification of water and air. For thermodynamic reasons, vacancies can only be created or be filled when the level of the electric potential of the acceptor species is lower than the level of the conduction band of the semiconductor, or when the level of the electric potential of the donor is higher than the level of the valence

band of the semiconductor. The limit of the bands of different semiconductors is shown in the figure below (fig. 12) [48].

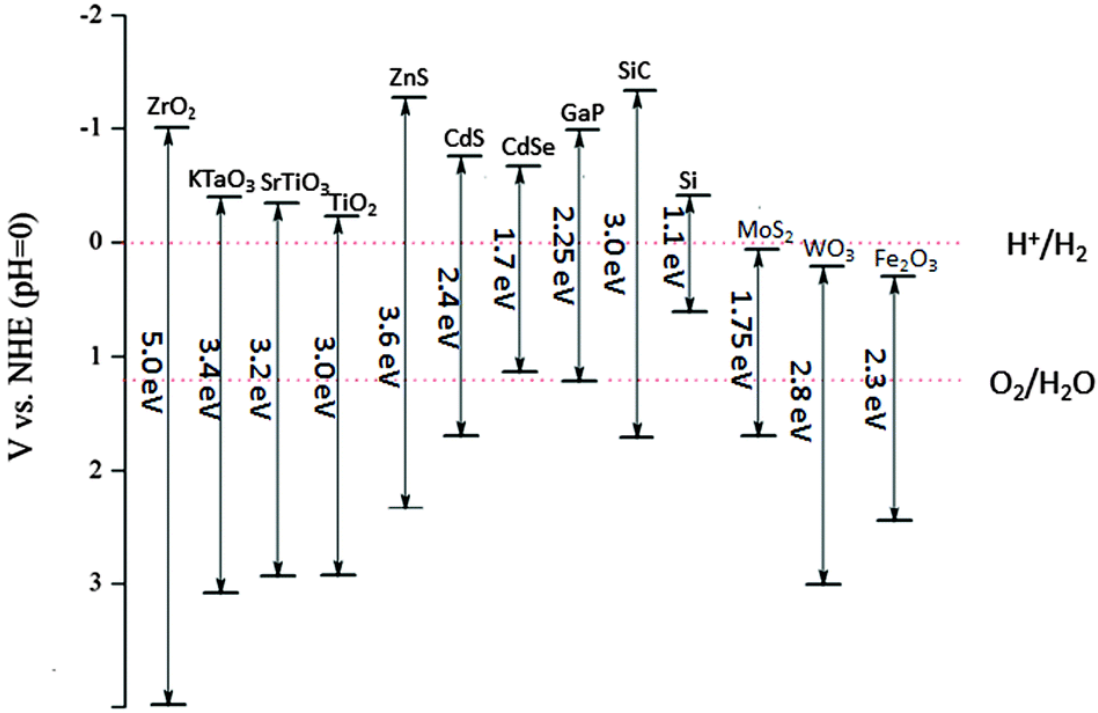

Fig. 12: Limit value bands of different semiconductors [48].

In TiO_2, electrons and vacancies do not combine immediately but trigger photocatalytic reactions at the surface of the particles, as shown in fig. 13.

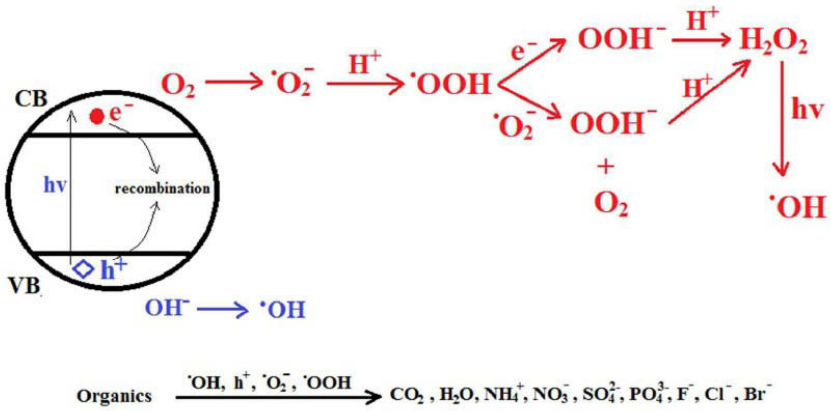

Fig. 13: Oxidation-reduction processes on TiO_2 NPs [49].

The water absorbed at the surface of the titanium oxide is oxidized by the vacancy and creates a hydroxyl radical (•*OH*) (6). Later on, this radical reacts with organic matter. If oxygen is present during this reactive process, the radicals present among the organic compounds and oxygen molecules start a chain reaction [reactions from (2) to (5)]. Finally, the organic materials decompose into carbon dioxide and water. Meanwhile, the electron deoxidizes and generates super oxide ions ($^{\bullet}O^{2-}$) as shown in reaction (7).

$$OH_{ads}^- + h_{vb}^+ \rightarrow {}^{\bullet}OH_{ads} \quad (6)$$

$$O_2 + e_{cb}^- \rightarrow {}^{\bullet}O_2{}^- \quad (7)$$

The surface of TiO_2 is covered with hydroxyl groups when it comes into contact with water: in effect, two distinct hydroxyl groups are formed when water is dissociated at the surface of pure TiO_2 (figs. 14 a, b, c).

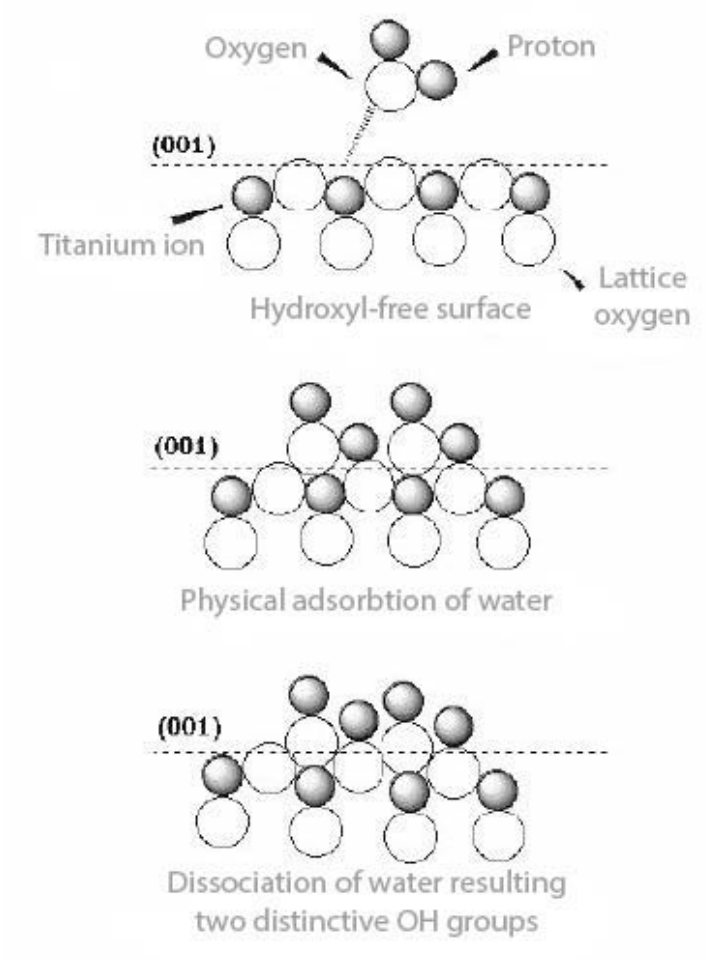

Figs. 14 a, b, c: Hydroxyl groups produced on the surface of TiO_2.

Another very interesting property of titania is their super-hydrophilicity [8] [6], which manifests itself at the surface of the material after exposure to UV light. Super-hydrophilic and hydrophobic behaviors are the two main ways to create self-cleaning materials. Wetting a solid with the water, where the air is the surrounding medium, is dependent on the relationship existing between the surface tensions at the interface (air-water, water-solid, solid-to-air). The relationship between these two voltages determines a contact angle ϑ.

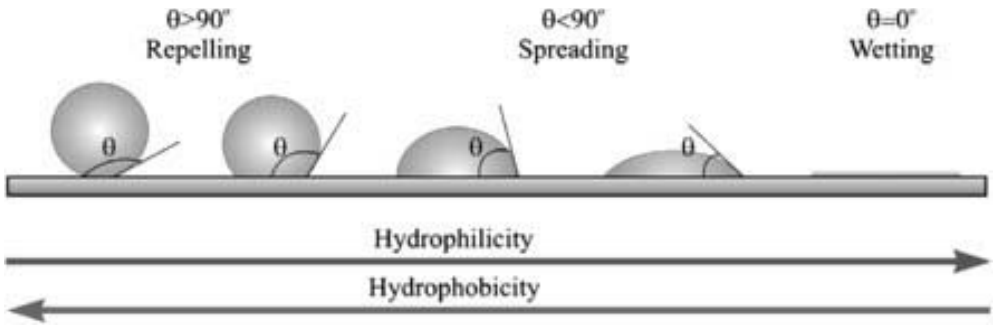

Fig. 15: Water drop shapes and contact angle values at solids of different hydrophobicity [50].

If ϑ is zero, then the wettability is complete, but if it has a value of 180° it is not. The higher the contact angle, the lower the adhesion

is (fig. 15). To create hydrophilic surfaces, one must decrease ϑ, which increases the efficiency of adhesion. The water-repelling property that characterizes the surfaces of plants has long been known.

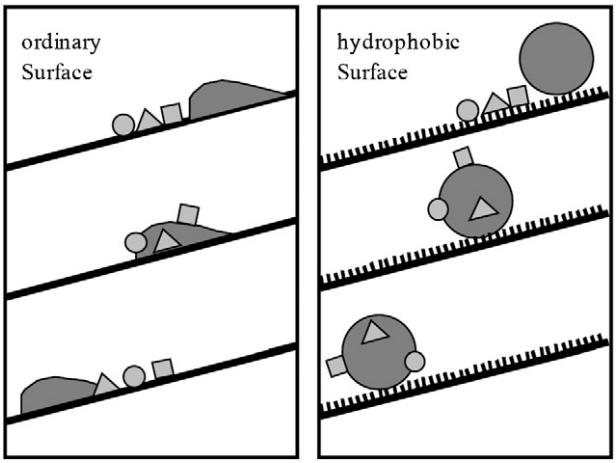

Figs. 16 a, b: "Lotus" effect, respectively, on an ordinary surface and on a hydrophobic surface [51].

Recently, the correlation between microstructure, wettability, and pollutants has been the object of several studies, with a particular focus on lotus leaves (also known as *Lotus effect* figs. 16 a, b) [52] [53] [54]. The micro-irregularities of its surface show contact angles higher than 130°; as a consequence the adhesion of water is notably reduced. Transferring such microstructures to artificial materials

could allow the development of hydrophobic surfaces. When water comes in contact with such surfaces, it is immediately contracted into droplets. Then, the particles of pollutants adhere to the surface of the droplets, and are removed when these roll away [51].

If the TiO_2 in the crystalline form of anatase is exposed to UV light, one can obtain very low (<1 °) contact angles. These materials have the rare property of attracting rather than repelling water. This characteristic is defined as super-hydrophilicity [53] [54]; water remains static at the surface, instead of forming droplets. The material remains super-hydrophilic for about two days after the end of the exposure to light [53]. Furthermore, UV illumination of the titanium dioxide leads to the formation of powerful agents that have the ability to oxidize and decompose many types of bacteria, as well as organic and inorganic materials [55] [56]. Super-hydrophilicity derives from the production of electrons and vacancies following the irradiation of the material by ultraviolet light, but the reactions that take place are different from those induced by photocatalysis. The electrons, in fact, reduce the cation Ti^{4+} to Ti^{3+}, while vacancies oxidize the anions O^{2-}. This process results in the ejection of an oxygen atom, creating the so-called "oxygen hole" (8-9).

$$Ti^{4+} + e^{-} \rightarrow Ti^{3+} \quad (8)$$

$$2O^{2-} + 4h^{+} \rightarrow O_2 \uparrow \quad (9)$$

The oxygen vacancies are replaced by dissociated water molecules, OH groups, which makes the surface hydrophilic. The increased exposure of the surface to UV radiation makes the contact angle between water and the surface smaller. After about thirty minutes of exposure under a UV light source of moderate intensity, the contact angle tends to approach zero, which means that the water has a tendency to cover the surface completely. A schematic representation of photoinduced hydrophilic conversion is depicted in fig. 17 [57].

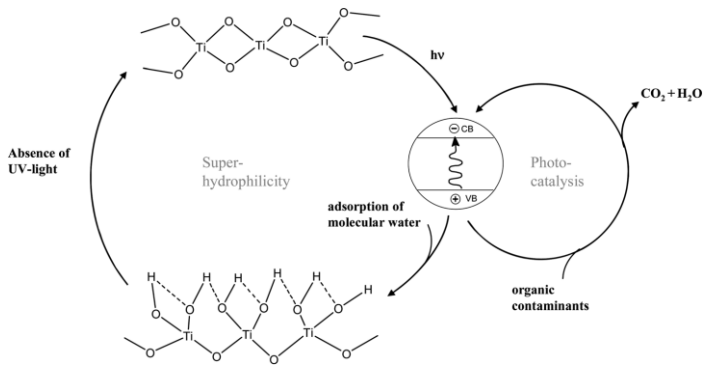

Fig. 17: Representation of the mechanism of photoinduced hydrophilicity [57].

Main uses of photocatalysis for sustainable architecture

The previously described mechanisms of photocatalysis on titanium dioxide materials have been widely studied, and several applications have been developed during the last two decades:

• air purification: a substantial reduction of organic volatile compounds (VOCs) and inorganic substances originating from human activities that cause air pollution, such as industrial production, cars, and home heating, was documented both in indoor and outdoor contexts [58] [59];

• deodorant: decomposing organic toxic gases that are a source of domestic discomfort (thiols/mercaptans, formaldehyde, and odors from fungal growths) [44] [60] [61] [62];

• antimicrobial action: the strong oxidizing power of photocatalysts was studied on both gram negative and gram positive bacterial strains (Escherichia coli, Staphylococcus aureus, Pseudomonas aeruginosa) [63], algae (Chlorella vulgaris) [64], and fungi (Candida Albicans) [65]. TiO_2 photocatalysis has strong bactericidal properties, due to the damage caused to the cell membrane caused by lipid peroxidation [56]. It has been evidenced that titania have stronger antibacterial effects than any other antimicrobial agent,

because the photocatalytic reaction works even when cells are covering the surface, and when bacteria are actively propagating [55];

• anti-fogging and other surface properties: when exposed to UV illumination, the photochemically-active TiO_2 can potentially convert a hydrophobic surface to a superhydrophilic surface, creating a water contact angle of $\vartheta=0°$ [66]. Once UV illumination is switched off, the TiO_2 film tends to lose its superhydrophilic qualities. A permanent superhydrophilic state has been obtained by assembling TiO_2 NPs with polyethylene glycol (PEG) [67], figs. 18 a, b.

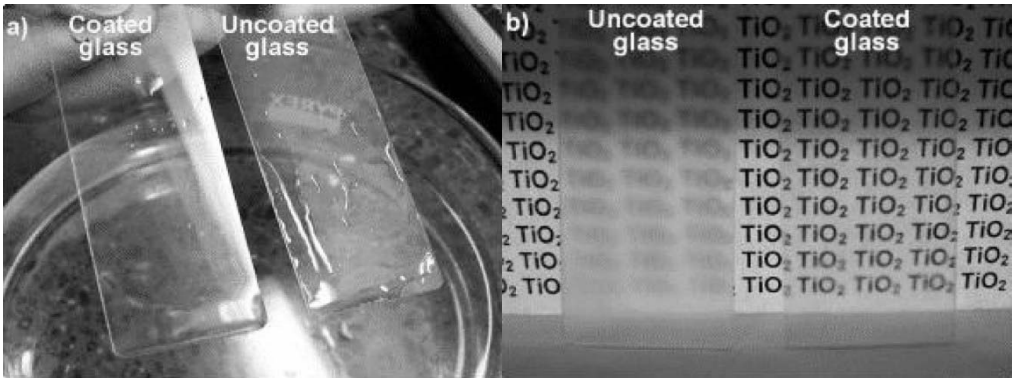

Figs. 18 a, b: Comparison of (a) wetting behavior and (b) antifogging properties between a TiO_2 coated and uncoated glass slide [67].

One of the objectives of this project is to develop a self-cleaning material surface coated with our doped titania material, which would show a total lack of water repellency and exhibit photocatalytic properties under visible light at the same time. It could be possible to use, for example, a coated mirror or glass in indoor environments without any blurring of the surface caused by water steam or vapor. On the coated surface, the water would become a thin, highly uniform layer, which would prevent it from fogging.

Most of outer building walls are fouled by the exhaust gases of vehicles and micro-organisms, whose growth is favored by the accumulations of fat and atmospheric dust. If these surfaces were coated with photocatalytic material, the dust would be washed away by the rain, and it would be possible to preserve the aesthetic characteristics of the buildings, at the same time to improve the quality of life and of the environment.

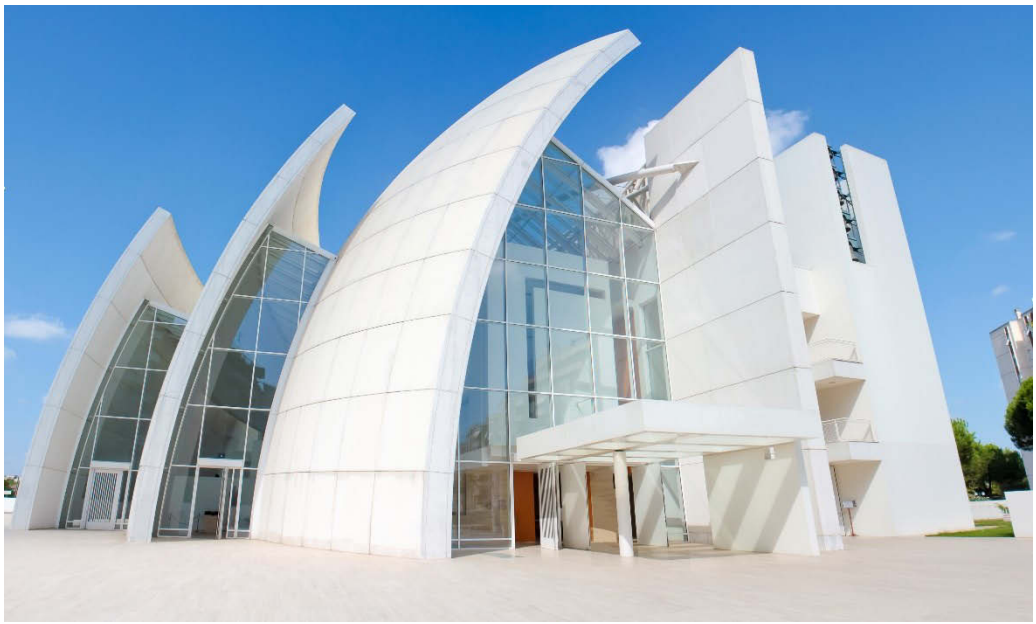

Fig. 19: Dives in Misericordia *church in Rome, Tor Tre Teste district, it was designed by Richard Meier architect for the Jubilee 2000, and built between 1998 and 2003. ©Getty images*

Experimental and Comments

Synthesis methods

The choice of the synthesis method for the production of nanoparticles is of fundamental importance regarding their characteristics and the application for which they are designed. In effect, through the synthesis method, we are able to control basic parameters such as the crystalline phase, the size, the crystallinity, and the chemical properties of the surface, which all are related to the photocatalytic activity.

Concerning the use of the material as a photocatalyst, the main features to be achieved to obtain a satisfactory efficiency were a

high surface area and the ability to relocate the e^-/h^+ pair, so as to reduce the processes of recombination of the charge carriers. The strong tendency of nanoparticles to aggregate in solution if there is a surface protection, which allows the dispersion, constitutes the main obstacle to be overcome in order to provide a material with these desired characteristics. To date, most methodologies are based on the use of organic surfactants, such as oleic acid [68] and polyethylene glycol [69], to obtain the dispersion of the particles in the solution [37] [70] [71] [72] [73]. The use of such organic compounds, however, causes a partial passivation of the surface, triggering the loss of active sites, and the consequent reduction of the catalytic activity [37] [73] [74]. In addition, normal processes of synthesis, such as sol-gel, require a calcination treatment at high temperature to transform the amorphous-phase in anatase-phase, which causes the growth of the size of the grains, and further decreases the relative surface area [75] [76] [77].

These reasons have led the research towards the study of a synthesis method that would allow us to obtain nanoparticles dispersed in aqueous solution at low temperature.

During the first phase of work, we used a sol-gel synthesis method such as reported in the literature [78], which allows the direct synthesis of nanoparticles of anatase dispersed in water at low temperature without the use of organic surfactants and treatments of calcination, and, subsequently, we modified this procedure in order to fit better to our purposes. Dispersion in solution is obtained by electrostatic repulsion. Synthesis of nanoparticles by sol-gel involves the hydrolysis of precursors of titanium and condensation of the formed species. These processes, which use alkoxides as precursors, have been well studied, and many works on this subject can be found in the literature [79]. The reaction between titanium alkoxides and water proceeds through a nucleophilic substitution mechanism, and can be represented by the following equilibrium reactions:

$$M(OR)_n + H_2O \rightarrow M(OR)_{n-1}(OH) + ROH \quad (10)$$

$$2M(OR)_{n-1}OH \rightarrow (OR)_{n-1}MOM(OR)_{n-1} + H_2O \quad (11)$$

$$M(OR)_{n-1}(OH) + M(OR)_n \rightarrow (OR)_{n-1}MOM(OR)_{n-1} + ROH \quad (12)$$

Hydrolysis (10) and condensation (11-12) reactions can take place in acidic or basic environment. Their succession leads to the formation of the gel.

The nature of the alkoxides strongly influences the magnitude of the reaction, since the difference in polarity between M and O has an influence on the nature of their bond, and, therefore, on the kinetics of the three reactions. Another important factor is the nature of the R group: it also influences the polarity of the M-O bond, and affects the solubility of the alkoxide molecules.

Other influencing parameters are the temperature, the pH, and the possible use of catalysts. An acidic catalyst increases the rate of the hydrolysis reaction (13):

$$(OR)_n M(OR) + H_3O^+ \rightarrow (OR)_n M(OH) + ROH + H^+ \quad (13)$$

Conversely, a basic catalyst increases the condensation rate:

$$(OR)_n M(OH) + OH^- \rightarrow (OR)_n MO^- + H_2O \quad (14)$$

$$(OR)_n MO^- + (OR)_n M(OR) + H_2O \rightarrow \rightarrow (OR)_n MOM(OR)_n + ROH + OH^- \quad (15)$$

The type of catalysis influences the speed of the reactions, and the structure of the products obtained (14-15). As a consequence of the extreme sensitivity to water of these precursors in the conventional synthetic routes, a minimum amount of water has been used together with an organic solvent that inhibits the hydrolysis. This method, however, involves obtaining amorphous phase particles at a low temperature, and a post synthesis heat treatment must be applied to obtain the crystalline phase [37] [80].

In addition, the selection of a solvent removal method is also critical for the final outcome [81] [82].

At the end of the condensation phase, the gel will be in wet form; if water is used as the solvent, we will have a structure called hydrogel. If the solvent is removed by evaporation in an oven or under vacuum, the gel structure collapses, increasing its density and forming a xerogel [83]. If the removal of the solvent occurs by extraction with supercritical fluids, no collapse will occur, and a low-density structure called aerogel will form [83].

On the contrary, our synthesis method uses a reaction environment with an excess of water for all the doped and non-doped NPs, nanosheets, xerogels, and aerogels, and an alcoholic environment

with a very small amount of water for all the syntheses indicated with the suffix *–prop* (2-propanol). The precursor is added to an excess amount of water so that the process of hydrolysis is rapid and leads to an intermediate, totally hydrolyzed compound (16) before the condensation phase (17). The reactions that occur are the following:

$$Ti(OC_4H_9)_4 + 4H_2O \rightarrow Ti(OH)_4 + 4C_4H_9OH \quad (16)$$

$$mTi(OH)_4 \rightarrow (TiO_2)m + 4mH_2O \quad (17)$$

In this case, Ti exists in the form of $[Ti(OH)_n(H_2O)_{6-n}]^{(4-n)+}$, which is crucial for the formation of the octahedral units of TiO_6 [84]. As it is known, the anatase phase is obtained when an octahedron shares its edges with four other units [36]. Therefore, more O^{2-} ions should be removed from TiO_6 in the case of formation of the anatase phase, which means that one needs to remove more H_2O molecules during the formation phase.

In our main synthesis process, the pH is maintained around 1.3, which means that there is a high concentration of protons in the reaction. In this situation, the hydroxyl group of the Ti-OH is

protonated, and it generates a large amount of Ti-OH^{2+}, which promotes the loss of water molecules when condensation occurs. In addition, the surface of the anatase nanoparticles obtained under these conditions are covered with H^+ ions, and all of them are all positively charged. This involves the electrostatic repulsion between particles, and allows the maintenance of the same effect during the dispersion. The mechanism is shown schematically in fig. 20.

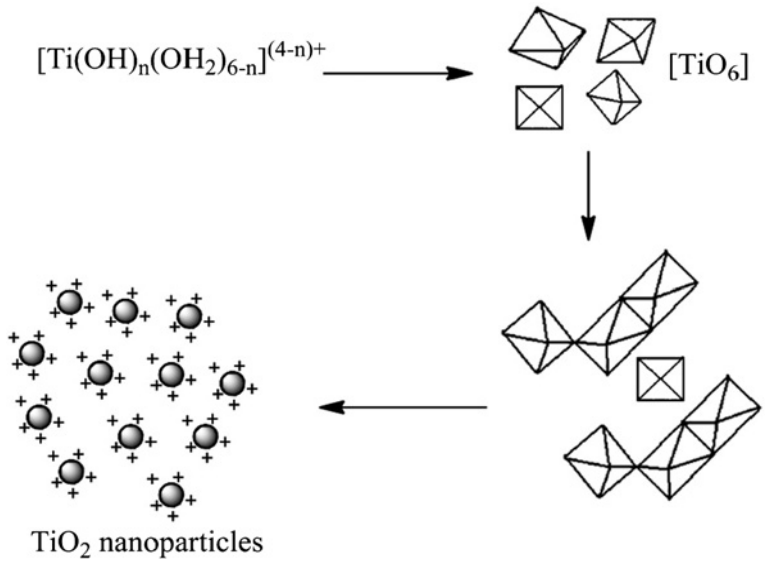

Fig. 20: Schematic illustration of the synthesis of TiO_2 nanoparticles dispersed in water.

In order to maintain the high concentration of positive charges in the environment during the reaction, while at the same time eliminating the use of H^+ sources, we replaced nitric acid with a lithium salt.

Thus, the surface of the nanoparticles always maintains a positive charge by avoiding aggregation, and the lithium ions also enter the lattice as a dopant. Other metals, acting as dopants and co-dopants, were inserted during the different stages of the syntheses, as explained later.

After the synthesis of the first group of nanoparticles, we published this new sol-gel method, which includes the use of Li^+ instead of H^+ [85]

Doping

The main purpose of titanium dioxide doping is to lower the energy gap in order to activate photocatalysis processes using visible light radiation. These materials can be used more effectively under solar light, or in indoor environments with a low quantity of UV radiation. Doping a material means inserting different species within the crystalline lattice so as to modify its electronic structure.

The dopants of a semiconductor may either be *n-type* (negative) or *p-type* (positive). N-dopants are dopants that possess one or more

electrons in excess of the substituted atom, introducing a negative charge that will be free to move across the material.

In contrast, a *p-type* dopant has less electrons than the atom it replaces, thus introducing a positive potential hole into the material.

In order to maintain the crystalline structure of the semiconductor (in the case of bulk materials), it is preferable that the doping species be placed near the surface of the material, as such a location is more beneficial when one deals with nanoparticles rather than larger structures [86].

Doping the material can be done by replacing Ti^{4+} ion with metal ions [87], as well as by replacing oxygen with anions [88].

In cationic doping, the dopant often ends up within the TiO_2 lattice, where it acts as a recombination center e^-/h^+; such a situation must be avoided. Consequently, making the doping process occur at the surface is equally important in this case. A high concentration of the dopant is another factor increasing the number of e^-/h^+ recombination cases, and should be avoided too.

The equation (18)

$$\mathrm{W} = \frac{2\varepsilon\varepsilon_0\psi}{\mathrm{eN_d}} \qquad (18)$$

where *W* represents the thickness of the space-charge layer, ψ is the surface potential, and N_d is the number of doping atoms, gives us the correlation for this phenomenon: when *W* is approximately equal to the penetration depth of the adsorbed photons in the solid, the photogenic electrons and the positive potential hole are sufficiently separated to make a recombination phenomenon improbable [89].

It is therefore necessary to find the right concentration of dopant, since too low a concentration may not bring any benefit, but a concentration that is too high may even inhibit the photocatalytic activity of the semiconductor [90].

Metal ion dopants like Co^{3+}, Ce^{3+}, Li^{+} influence the photoreactivity of TiO_2 by acting as electron (19) or hole (20) traps, and by altering the e^-/h^+ pair recombination rate through the following process [87] [91] [92] [93] [94]:

$$M^{n+} + e_{cb}^{-} \rightarrow M^{(n-1)+} \quad (19)$$

$$M^{n+} + h_{vb}^{+} \rightarrow M^{(n+1)+} \quad (20)$$

where the energy level for $M^{n+}/M^{(n-1)+}$ lies below the conduction band edge (E_{cb}) and the energy level for $M^{n+}/M^{(n+1)+}$ above the

valence band edge (E_{vb}). The introduction of such energy levels in the band gap induces a red shift in the band gap transition, and the visible light absorption through a charge transfer between a dopant and CB (or VB) or a *d-d* transition in the crystal field. According to the energy level reported by Choi et al. [87], Co^{3+} can act as both hole and electron traps.

Although it is widely accepted that the photoreactivities of doped TiO_2 are related to the dopant trap site, the fact that the trapped charges should be transferred to the interface to start the photoreactions is often neglected. In this context, the energetics of the charge release and migration in the lattice as well as the charge-trapping energetics are equally important. A general photochemical charge-pair generation (21-23), charge-trapping (24-27), charge release and migration (28-29), recombination (30-35) and interfacial charge transfer (36-37) in the presence of metal ion dopants can be explained as follows [87]:

$$TiO_2 + h\nu \rightarrow e_{cb}^- + h_{vb}^+ \quad (21)$$

$$M^{n+} + h\nu \rightarrow M^{(n+1)+} + e_{cb}^- \quad (22)$$

$$M^{n+} + h\nu \rightarrow M^{(n-1)+} - h_{vb}^+ \quad (23)$$

$$Ti^{4+} + e_{cb}^{-} \rightarrow Ti^{3+} \quad (24)$$

$$M^{n+} + e_{cb}^{-} \rightarrow M^{(n-1)+} \quad (25)$$

$$M^{n+} + h_{vb}^{+} \rightarrow M^{(n+1)+} \quad (26)$$

$$OH^{-} + h_{vb}^{+} \rightarrow OH^{\bullet} \quad (27)$$

$$M^{(n-1)+} + Ti^{4+} \rightarrow M^{n+} + Ti^{3+} \quad (28)$$

$$M^{(n+1)+} + OH^{-} \rightarrow M^{n+} + OH^{\bullet} \quad (29)$$

$$e_{cb}^{-} + h_{vb}^{+} \rightarrow TiO_2 \quad (30)$$

$$Ti^{3+} + OH^{\bullet} \rightarrow Ti^{4+} + OH^{-} \quad (31)$$

$$M^{(n-1)+} + h_{vb}^{+} \rightarrow M^{n+} \quad (32)$$

$$M^{(n-1)+} + OH^{\bullet} \rightarrow M^{n+} \quad (33)$$

$$M^{(n+1)+} + e_{cb}^{-} \rightarrow M^{n+} \quad (34)$$

$$M^{(n+1)+} + Ti^{3+} \rightarrow M^{n+} + Ti^{4+} \quad (35)$$

$$e_{cb}^{-} \left(or\ M^{(n+1)+},\ Ti^{3+}\right) + A \rightarrow A^{-} \quad (36)$$

$$h_{vb}^{+} \left(or\ M^{(n-1)+},\ OH^{\bullet}\right) + D \rightarrow D^{+} \quad (37)$$

Where M^{n+} is a metal ion dopant, *A* is an electron acceptor, and *D* is an electron donor.

Some other general trends are apparently related to the electronic configuration of the dopants. All dopants with a closed-shell electronic configuration (Li^{+}, Mg^{2+}, Al^{3+}, Zn^{2+}, Ga^{3+}, Zr^{4+}, Nb^{5+}, Sn^{4+}, Sb^{5+}, and Ta^{5+}) have little effect on the observed photoreactivity [95] [96] [97]. Thus, the stability of a closed electronic shell makes electron (or hole) trapping unfavorable. The second prerequisite for being an effective dopant may involve the possibility of charge detrapping and migration to the surface of previously trapped charges. It is also important to notice that all energetic considerations are valid only for dopants located close to the surface site at which the interfacial charge transfer occurs. Since the diameter of the exciton in nanosized TiO_2 is approximately 20 Å, the prerequisites are met within a nanosecond of excitation [87].

A nano-sized particle represents an unusual case with respect to electron transfer at the semiconductor-liquid interface compared to their bulk-phase counterparts. A distinctive feature of nano-sized semiconductors is the lack of appreciable band bending. The total potential drop occurring within a nanoparticle is given by (38) [98]:

$$\Delta\varphi = kT/6e(\frac{r_0}{L_D})^2 \quad (38)$$

where r_0 is the radius of the particle, and L_D is the Debye length. For a particle of 3 nm diameter with 0.5 at.% of dopants, $\Delta\varphi$ is calculated to be 0.01 V. Considering that the magnitude of the potential drop across the space-charge layer should not be less than 0.1 V for an efficient e^-/h^+ separation [99], the small potential drop for nano-sized TiO_2 (0.01 V) constitutes an insufficient driving force for the charge pair separation within a particle. Moreover, in nano-sized particles, the wave function of the charge carrier spreads over the entire semiconductor cluster [100]. As a result, both electrons and holes are readily available at the interface. Oxidation reactions by VB holes and reduction reactions by CB electrons can thus occur concurrently, thereby satisfying the condition of electro-neutrality on a semiconductor particle, in which an e^- reacts (36) for each reacted h^+ (37).

Finally, the photo-reactivities of doped TiO_2 can vary widely in function of the specific dopant. The origin of these different photo-reactivities appears to be related to the effectiveness of the dopants in trapping charge carriers and mediating interfacial charge transfer. This idea is supported by the transient absorption decays of the trapped electron [87]. The trapped electron in TiO_2 colloids gives rise to a broad absorption band (400-1000 nm) with a nominal maximum

around 600 nm [101], while the trapped hole exhibits a broad absorption (400-800 nm) band with λ_{max}=475 nm [102]. The overlap of absorption bands near 600 nm seems to be negligible over the nanosecond time-frame because electron trapping is much faster (τ ≈ 30 ps) than the hole trapping (τ ≈ 250 ns) [103]. However, this overlap may not be negligible at the microsecond time scale, and the presence of metal ion dopants provides more traps sites for holes, in addition to the original surface traps sites ($OH^{\cdot}$) (39-40) [87] [103]:

$$e_{cb}^{-} \rightarrow e_{trap}^{-} \left(as\ M^{(n-1)+}\ or\ Ti^{3+}\right) \qquad \tau \approx 30\ \text{ps} \quad (39)$$

$$h_{vb}^{+} \rightarrow h_{trap}^{+} \left(as\ M^{(n+1)+}\ or\ OH^{\bullet}\right) \qquad \tau \approx 250\ \text{ns} \quad (40)$$

$$e_{trap}^{-} + h_{vb}^{+} \rightarrow TiO_2 \qquad \tau \approx 30\ \text{ns} \quad (41)$$

$$e_{trap}^{-} + h_{trap}^{+} \rightarrow TiO_2 \qquad slow\ (microsecond\ domain) \quad (42)$$

Considering that the mean lifetime of a single electron-hole pair in a TiO_2 particle (12 nm diameter) was determined to be 30 ns (41) [103], the appearance of a plateau in the absorption decay curves (microsecond domain) of the doped TiO_2 NPs [87] indicates a slow recombination process described by (42). The follow equation (43)

show that all the excited-state decays in the microsecond time region were fitted as double exponential [101] [104]:

$$A(t) = A_{\infty} + C_1 \exp(-k_1 t) + C_2 \exp(-k_2 t) \quad (43)$$

the A_{∞} (which represents the residual absorption by the trapped charge carriers that survive recombination over the nano to microsecond time domain) should be regarded as the relative absorption by both e^-_{trap} and h^+_{trap}, even though their proportions are unknown. The trapped charge carriers have a sufficiently long lifetime to reach the surface by detrapping (28-29) and electron tunneling. Consequently, the higher the A_{∞} value, the higher the observed photo-reactivity.

A metal ion dopant assumes the role of a direct mediator of the interfacial charge transfer. Given the size of nano-sized particles, the dopants are located within 10-20 Å from the surface. Under these conditions, all dopants can be considered as located in the surface region, where charge transfer to the interface is easily achieved. As the small nano-sized particles agglomerate upon heating, dopants that are isolated far from the surface stand a much lower chance of transferring trapped charge carriers to the interface. Choi et al. [87]

showed that a steady decrease in the photo-reactivity of doped TiO_2 was concomitant with an increase in sintering temperature. Because of particle agglomeration, dopants are more likely to act as recombination centers than as trap sites for possible charge transfer at the interface.

During the past twenty years, the role of Co^{2+} as a dopant for titania lattice have also received a huge amount of attention for its ferromagnetism property, which was reported for the first time by Matsumoto *et al.* [105]. However, few studies have been made about its role as co-dopant with Li^{+} for the bandgap lowering.

Bellardita et al. [106] clearly explained the role of W as a dopant: it works as *protector* of e^{-}, trapping the electrons according to the reaction (44):

$$W^{6+} + e^{-} \rightarrow W^{5+} \quad (44)$$

and then releasing them into contact with the oxygen forming the superoxide radical (45):

$$W^{5+} + O_2 \rightarrow W^{6+} + {}^{\bullet}O_2{}^{-} \quad (45)$$

However, tungsten behaviors could act as potential recombination centers, in accordance with the reactions 46-47:

$$W^{6+} + e^{-} \rightarrow W^{5+} \quad (46)$$

$$W^{5+} + h^{+} \rightarrow W^{6+} \quad (47)$$

showing that they are in competition with redox reactions to the interface.

Not all dopants exert a positive influence on the semiconductor. Some species such as Ga^{3+}, Cr^{3+},and Sb^{5+} always act as recombination sites due to the high recombination rate of the electrons contained within their orbits with the holes h^{+}, which is then canceled out before it can spread to the surface [89].

Unlike metal cations, anion doping does not behave as a recombination center; consequently, its only effect is to raise the energy level of the valence bandwidth by blending its oxygen 2p orbitals with the ones of the dopant, resulting in a decrease in band gap [107].

Co-doping (doping with more than one element) is another valid option for modifying a semiconductor. With the right combination of dopants, this route can sometimes be even more convenient than

just doping. In [108], a strongly improved photocatalytic activity due to co-doping with Fe^{3+} and Eu^{3+} is reported, which can be explained by the different behaviors of the ions, leading in both cases to an improvement of the photocatalysis. The behavior of this co-doping reaction is similar to the introduction of a n-dopant and a p-dopant into the lattice; in effect, Fe^{3+}, as discussed in [87], always acts as a trap for h^+:

$$Fe^{3+} + h^+ \rightarrow Fe^{4+} \quad (48)$$

while Eu^{3+} will act as a trap for electrons:

$$Eu^{3+} + e^- \rightarrow Eu^{2+} \quad (49)$$

therefore, the simultaneous action of the two dopants will drastically reduce the possibility of e^-/h^+ recombination.
Fe^{4+} and Eu^{2+} will then react at the interface, by forming species that are susceptible to degrade pollutants (50-51):

$$Eu^{2+} + O_2 \rightarrow Eu^{3+} + {}^{\bullet}O_2{}^- \quad (50)$$
$$Fe^{4+} + OH^- \rightarrow Fe^{3+} + OH^{\bullet} \quad (51)$$

Experimental procedures and analyses

The first group of syntheses of titanium dioxides nanoparticles (NPs) was carried out with an excess of water, using titanium tetrabutoxide (TBot) as a precursor, and with a molar ratio between precursor, water, isopropanol, and nitric acid equal to 1: 155: 1.5: 0.1. After having carefully washed and dried the glassware used during the synthesis, 3 ml of the precursor TBot (Sigma-Aldrich, ≥ 97%, MM = 340.32 g mol^{-1}, d = 1.00 g ml^{-1}) were placed, together with 0.96 ml of 2-propanol (Lab-Scan, ≥ 99.7%, d = 0.785 g mL^{-1}), in a dropping funnel. The funnel was then mounted above a 100 ml flask containing 24.7 ml of deionized water and 0.3 ml of nitric acid (Baker, 65%, d=1,40 g ml^{-1}), so as to obtain a pH of 1.3. The flask, placed within a magnetic stirrer, was placed into an oil bath so as to keep the temperature constant during all the time necessary for the synthesis. After reaching a temperature of 80° C, the tap funnel containing the solution of the precursor was opened, allowing the solution to drip slowly (1 ml min^{-1}) into the flask containing the aqueous solution, which had been kept under vigorous stirring for 24 hours. At the end of the process, the colloidal solution of anatase was allowed to cool down to room temperature. The particles

remained dispersed in the solution for several months without showing any noticeable sign of agglomeration. To obtain dry particles, the colloidal solution was first subjected to cycles of centrifugation (Beckman microfuge E^{TM}) at 14000 rpm for 30 minutes. At the end of each spin cycle, the supernatant solution was removed, and replaced with ultrapure water to proceed to additional washes through other spin cycles. After a number of three washes, a gel was formed, which was then dried under vacuum at 25° C, so as to obtain the nanoparticles in powder form. This synthesis represents the basis for subsequent modifications.

In order to remove nitric acid from the synthesis, we used two different lithium salts in substitution. The synthesis was then repeated with the same modalities and amounts previously used, but without using the acidic source of H^+. In this case, the nitric acid was replaced by a suitable amount of LiCl or $LiNO_3$.

In order to improve the photocatalytic properties of the particles of TiO_2, we made several other syntheses in which, besides the use of the lithium salt in place of the nitric acid, we added $CoCl_2$, CeO_2, and WCl_6 in different w/w percentages as dopants, as reported in table 1. The experimental procedure was the same as the one described

above, the only difference being that 1 – 3 – 5 % w/w of Li^{+} (as LiCl or $LiNO_3$) (respect to TBot), 1 – 3 – 5 % w/w of Co^{2+} (as $CoCl_2$) (respect to TBot), 1 – 3 – 5 % w/w of Ce^{4+} (as CeO_2) (respect to TBot), and 3 – 5 – 7 % w/w of W^{6+} (as WCl_6) (respect to TBot) were also added to the aqueous solution.

Fig. 21: Samples of nanoparticles of ND-TiO_2 (left) and TiLi(5)Co(5) (right).

Once the sol-gel suspensions had been obtained, we proceeded with a series of two-steps desolvation procedures under vacuum in order to obtain the nanosheets.

A 470° annealing was also applied for 2 hours, in order to dry the gel and obtain a transparent xerogel monolith.

The synthesis of Au@TiLi(5) NPs started with the synthesis of citrate-stabilized Au NPs based on the single-phase aqueous reduction of tetracholoauric acid ($HAuCl_4$) by sodium citrate. This procedure, initially developed by Turkevich et al. [109] and further refined by Frens [110], still remains the most commonly employed aqueous method. It is possible to control the size of Au NPs from 5 to 150 nm by simply varying the reaction conditions, such as sodium citrate to gold salt ratio [110], solution pH [111], and solvent [112]. In order to increase the quality (i.e. the size and the size distribution) of the particles, we followed the synthesis refined by Bastús et al. [113], as it provides higher monodispersity, higher concentrations, and a better control of the gold nanoparticles size distribution. In a second step, the Au nanoparticles were used as seed for the growth of the anatase phase, using our modified aqueous method and the alcoholic synthesis.

The concentration of the Au nanoparticles was determined in approximation using the plasmon resonance peak at the surface.
In accordance with what was described in [114], the average diameter of nanoparticles of gold was first determined by the formula:

$$d = e^{\frac{B_1 A_{prs}}{A_{450}} - B_2} \quad (52)$$

where B_1 and B_2 are the constants experimentally obtained in [114], which are respectively 3,00 e 2,20, A_{prs} is the absorbance value at the wavelength of the resonant plasmon, and A_{450} is the absorbance value at 450 nm (fig. 22).

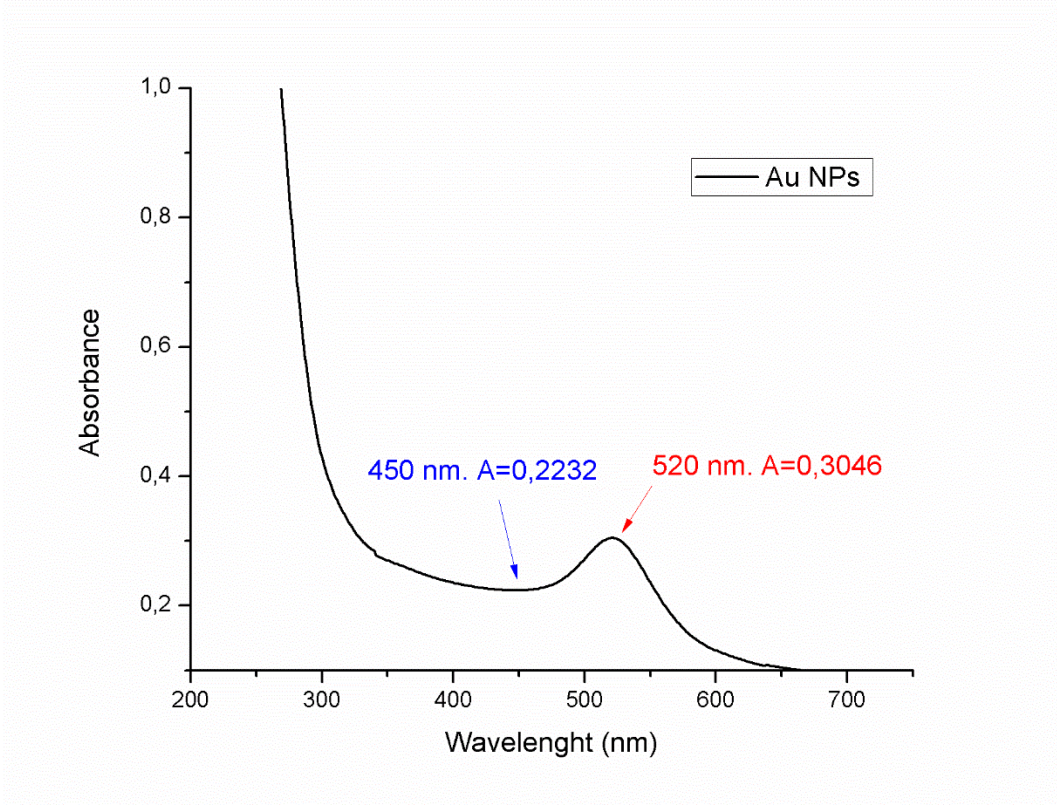

Fig. 22: Plasmon resonance of the Au NPs, solution diluted 10 times.

According to this equation, the value is 11 nm. It is then possible to calculate the concentration, always in accordance with formula 53 [114]:

$$C = \left(\frac{A_{spr}(5{,}89 \cdot 10^{-6})}{d^{c_2}\, e^{c_1}}\right) \quad (53)$$

where $c_1 \text{and}\ c_2$ are experimental constants with the value of -4,74 e 0,314, respectively.

The resulting concentration, expressed in molarity, is about $3 \cdot 10^{-3} M$.

Knowing the nano-gold solution concentration, the number of nanoparticles was obtained by dividing the total weight of the gold contained in the solution, which can be easily derived from the concentration, in order to estimate the average weight of each single nanoparticle in function of its diameter. From the number of cores to be coated, we calculated the amount of precursor needed to obtain the same number of TiO_2 nanoparticles with an approximate diameter of 100nm.

We used 1 ml of Titanium butoxide. The synthesis apparatus was the same as the previous ones: 100 ml of Millipore water was poured

into the balloon, in which 0.07g $LiNO_3$ was solubilized. When the temperature of the solution in the flask was near 80° C, the nano-Au suspension was added. Subsequently, the tap of the funnel charger was opened to drip Titanium (IV) butoxide.

The initially pinkish reaction mixture for the presence of gold then began to opacify, and the color of the solution quickly acquired a lilac hue, almost tending to gray.

Once the synthesis was completed, washes were performed in the same manner as for the precedent synthesis, and the solution was centrifuged and then dried in a drying oven (fig. 23).

Fig. 23: Au@TiLi(5) NPs.

Table 1: list of all the syntheses prepared.

Anatase TiO_2 and dopant precursor used during the preparation	**Name (as used in the text)**	**Number of Syntheses**
Not doped TiO_2 (control sample)	ND-TiO_2	7
TiO_2 + LiCl (Li 5% w/w) + HNO_3 (intermediate)	TiLiCl-acid intermediate	1
TiO_2 + LiCl (Li 1% w/w)	TiLiCl(1)	6
TiO_2 + LiCl (Li 3% w/w)	TiLiCl(3)	6
TiO_2 + LiCl (Li 5% w/w)	TiLiCl(5)	6
TiO_2 + $LiNO_3$ (Li 5% w/w) + HNO_3 (intermediate)	TiLiNO_3-acid intermediate	1
TiO_2 + $LiNO_3$ (Li 1% w/w)	TiLi(1)	6
TiO_2 + $LiNO_3$ (Li 3% w/w)	TiLi(3)	6
TiO_2 + $LiNO_3$ (Li 5% w/w)	TiLi(5)	6
TiO_2 + $LiNO_3$ (Li 5% w/w) + $CoCl_2$ (Co 1% w/w)	TiLi(5)Co(1)	6
TiO_2 + $LiNO_3$ (Li 5% w/w) + $CoCl_2$ (Co 3% w/w)	TiLi(5)Co(3)	6
TiO_2 + $LiNO_3$ (Li 5% w/w) + $CoCl_2$ (Co 5% w/w)	TiLi(5)Co(5)	6
TiO_2 + $LiNO_3$ (Li 5% w/w) + CeO_2 (Ce 1% w/w)	TiLi(5)Ce(1)	6
TiO_2 + $LiNO_3$ (Li 5% w/w) + CeO_2 (Ce 3% w/w)	TiLi(5)Ce(3)	6
TiO_2 + $LiNO_3$ (Li 5% w/w) + CeO_2 (Ce 5% w/w)	TiLi(5)Ce(5)	6
TiO_2 + LiCl (Li 5% w/w) + WCl_6 (W 3% w/w)	TiLi(5)W(3)	3
TiO_2 + LiCl (Li 5% w/w) + WCl_6 (W 5% w/w)	TiLi(5)W(5)	3
TiO_2 + LiCl (Li 5% w/w) + WCl_6 (W 7% w/w)	TiLi(5)W(7)	3

TiO_2 + $CoCl_2$ (Co 5% w/w) in 2-propanol	TiCo(5)-prop	2
TiO_2 + WCl_6 (W 5% w/w) in 2-propanol	TiW(5)-prop	2
TiO_2 + $LiNO_3$ (Li 5% w/w) nanosheets	TiLi(5)-nanosheets	3
TiO_2 + $LiNO_3$ (Li 5% w/w) + $CoCl_2$ (Co 5% w/w) nanosheets	TiLi(5)Co(5)-nanosheets	3
TiO_2 + (Li 5% w/w) + CeO_2 (Ce 5% w/w) nanosheets	TiLi(5)Ce(5)-nanosheets	3
TiO_2 + $LiNO_3$ (Li 5% w/w) xerogel	TiLi(5)-xerogel	1
TiO_2 + $LiNO_3$ (Li 5% w/w) + $CoCl_2$ (Co 5% w/w) xerogel	TiLi(5)Co(5)-xerogel	1
TiO_2 + (Li 5% w/w) + CeO_2 (Ce 5% w/w) xerogel	TiLi(5)Ce(5)-xerogel	1
TiO_2 + $LiNO_3$ (Li 5% w/w) + $CoCl_2$ (Co 5% w/w) aerogel	TiLi(5)Co(5)-aerogel	1
TiO_2 + WCl_6 (W 5% w/w) in 2-propanol aerogel	TiW(5)-prop-aerogel	1
Au@TiO_2 + (Li 5% w/w)	Au@TiLi(5)	1

All the materials obtained (table 1) by the different syntheses were subjected to characterization. In this study, we used as control samples the Degussa P25® (Evonik Degussa GmbH), which is the most common material used for photocatalysis studies [16] [115] [116], with an 80:20 anatase-rutile composition, and an average dimension of the particles of 25 nm.

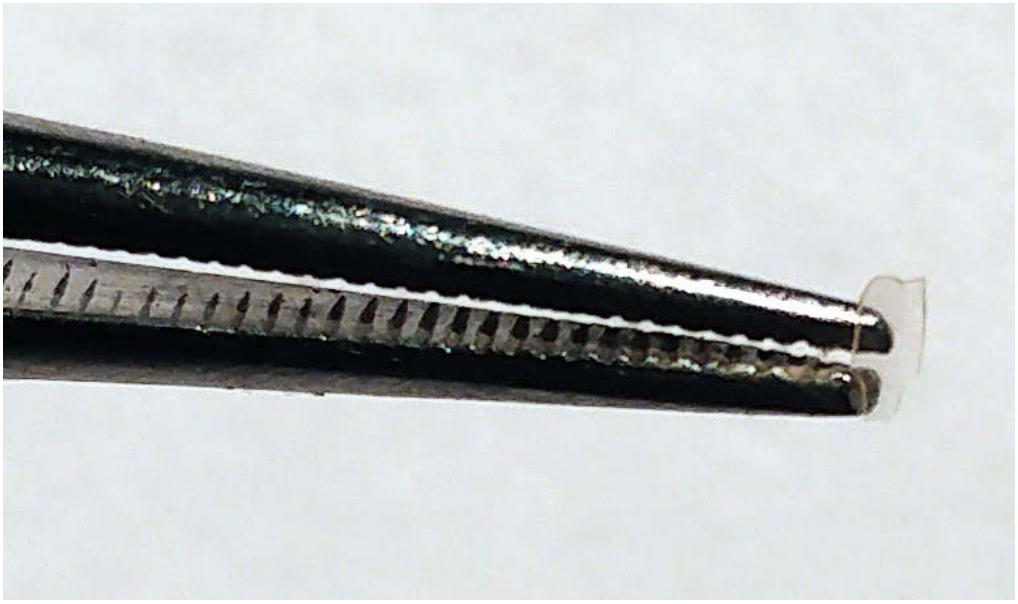

Fig. 24: TiLi(5)Co(5) doped nanosheet.

The XRD instrument used for the diffractometric measurements was a Bruker-AXS D8. The spectra were obtained with an 2θ angle between 20° and 70°, using the Kα radiation of Cu (1,542 Å), with a scanning speed of 1°/min.

Raman spectra were recorded using a micro-Raman spectrometer made up of an argon laser source Spectra-physics with λ = 514.5 nm, an optical microscope with objectives ranging from 10 to 100 x, and a CCD detector Jobin Yvon hr 460 cooled with liquid nitrogen.

Scanning Electron Microscopy images of the powdered sample were recorded with a microscope FEDSEM LEO Supra 55 VP, combined with a Carl Zeiss column GEMINI, and an Oxford EDX (Energy dispersive spectroscopy) analytical instrument, to obtain information about the quantitative distribution and the amount of the metallic species present in the samples.

Trasmission Electron Microscopy of the powered sample were recorded on a copper grid with a FEI Tecnai F20 Field Emission microscope, equipped with a Gatan Image Filter and an Edam EDX analytical instrument.

Nitrogen adsorption – desorption isotherms were measured at -196 °C by using a Micromeritics Tristar 3000 system. The samples were then degassed at 160 °C overnight on a vacuum line. To calculate the specific surface area, we used the standard multi-points Brunauer–Emmett–Teller (BET) method [117], with some further modifications [118] [119] [120]. The pore size distributions of the materials were derived from the adsorption branches of the isotherms, based on the Barrett–Joyner–Halenda (BJH) model [121].

Optical absorption spectra were recorded at room temperature with a Jasco V-650 UV-Vis-NIR spectrophotometer.

Samples for ^{7}Li MAS NMR spectroscopy analysis were prepared in a dry box in N_2 atmosphere, inserted in 4 mm zirconia rotors with a available volume reduced to 20 µl, and sealed with kel-F caps.

^{7}Li magic angle spinning (MAS) NMR (I=3/2, 92.6% abundance) spectra were recorded at 155.50 MHz on a Bruker Avance 400 spectrometer. The π/2 pulse width was 5.5 µs. Spectra were acquired with a time domain of 4 k data points, zero filled, and Fourier transformed with a size of 16 k data points. The spin-rate was kept at 5500 Hz. The ppm scale was created using LiCl as an external reference. The longitudinal relaxation time T_1 was measured using the saturation recovery pulse sequence. The measurement of the longitudinal relaxation times allowed the optimization of the recycle delay to be used for collecting ^{7}Li spectra. The transverse relaxation time T_2 was determined using the quadrupolar Carr-Purcell-Meiboom-Gill (QCPMG) pulse sequence.

Discussion

Phase characterization – XRD, Raman

X-ray diffraction was used to verify that the crystalline phase is anatase, as it was designed in the synthesis step. In figure 25, the diffractogram of a TiW(5)-prop sample is reported; its most intense peak assumes a value of 2θ = 25.32°, and was assigned to the lattice plane (101) of anatase. The presence of rutile cannot be proved with this technique, since the dimension of the nanoparticles make its peaks very broad. The peak situated at a value of 2θ = 54,18° could indicate the presence of a small percentage of rutile, probably formed during the synthesis phase, or through the conversion of the anatase phase to rutile resulting from light exposure.

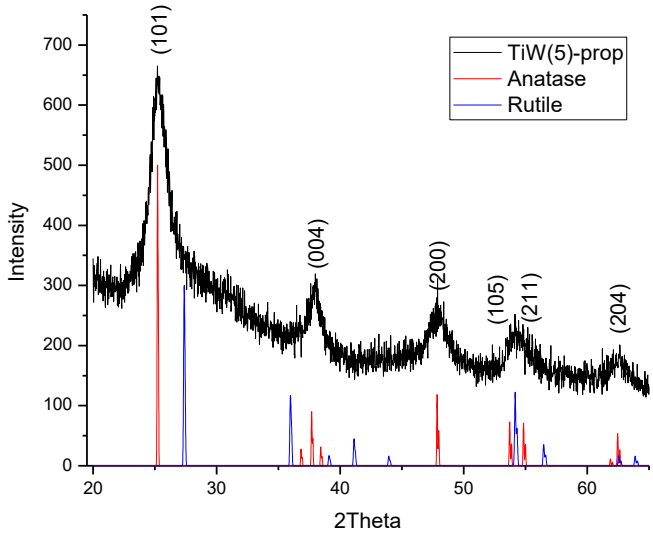

Fig. 25: Diffractogram of TiW(5)-prop compared to Anatase and Rutile.

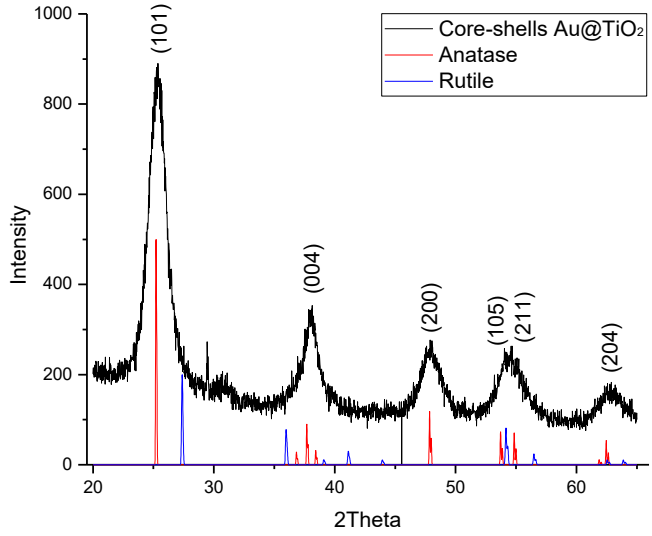

Fig. 26: Diffractogram of Au@TiLi(5) compared to Anatase and Rutile.

We analyzed all the materials, but no evidence of the doping species appeared on the diffractograms. The spectra of all the doped TiO_2 samples almost perfectly matched with the spectrum of pure Anatase TiO_2. Ionic radius is one of the most important factors determining the possibility of a dopant to enter the lattice of the crystal of TiO_2 in order to form a stable lattice. If the ionic radius of the dopant is too large or too small compared to Ti^{4+} (0,64 Å), the input of the dopant in the crystal leads to a distortion of similar proportion. This is not the case here, because the ionic radius of Co^{2+} (0.65 Å) is comparable with Ti^{4+}; in fact, no appreciable difference between the diffractograms could be be noticed at all.

However, we used these diffractograms to calculate the size of the nanoparticles, using Scherrer's equation (54) [122], as modified by Monshi et al. (55-57) [123], in order to reduce the error and obtain a more accurate value for *L*. The results are summarized in table 2, in comparison with other techniques.

$$\mathrm{L} = \frac{K\lambda}{\beta \cdot cos\vartheta} \qquad (54)$$

$$\beta = \frac{K\lambda}{L \cdot cos\vartheta} = \frac{K\lambda}{L} \cdot \frac{1}{cos\vartheta} \quad (55)$$

$$\ln\beta = \ln\frac{K\lambda}{L \cdot cos\vartheta} = \ln\frac{K\lambda}{L} + \ln\frac{1}{cos\vartheta} \quad (56)$$

$$e^{\ln\frac{K\lambda}{L}} = \frac{K\lambda}{L} \quad (57)$$

The modified Scherrer's equation provides the advantage of decreasing the sum of the absolute values of errors, $\sum(\pm\Delta\ln\beta)^2$, and of producing a single line running through all the points to give a unique value, $\ln\frac{K}{L}$, to the intercept.

In fig. 27, the Raman spectrum of the ND-TiO_2 is reported. Its comparison with the spectra of pure phases of rutile and anatase makes it clear that the spectra of the synthesis produced nanoparticles are comparable to those of the anatase phase. In effect, the bands of our sample are located at 417 cm^{-1}, 527 cm^{-1} and 645 cm^{-1}.

All peaks appear very wide; in particular, the 645 cm^{-1} peak shows a raising of the base line, which is probably due to the overlap of its signal with the signal of rutile, which is located to 610 cm^{-1}. The presence of a small amount of rutile does not constitute an issue,

since it has been shown that the best catalytic activity is obtained by using a mixture of anatase-rutile 4:1, as in the commercial product Degussa P25.

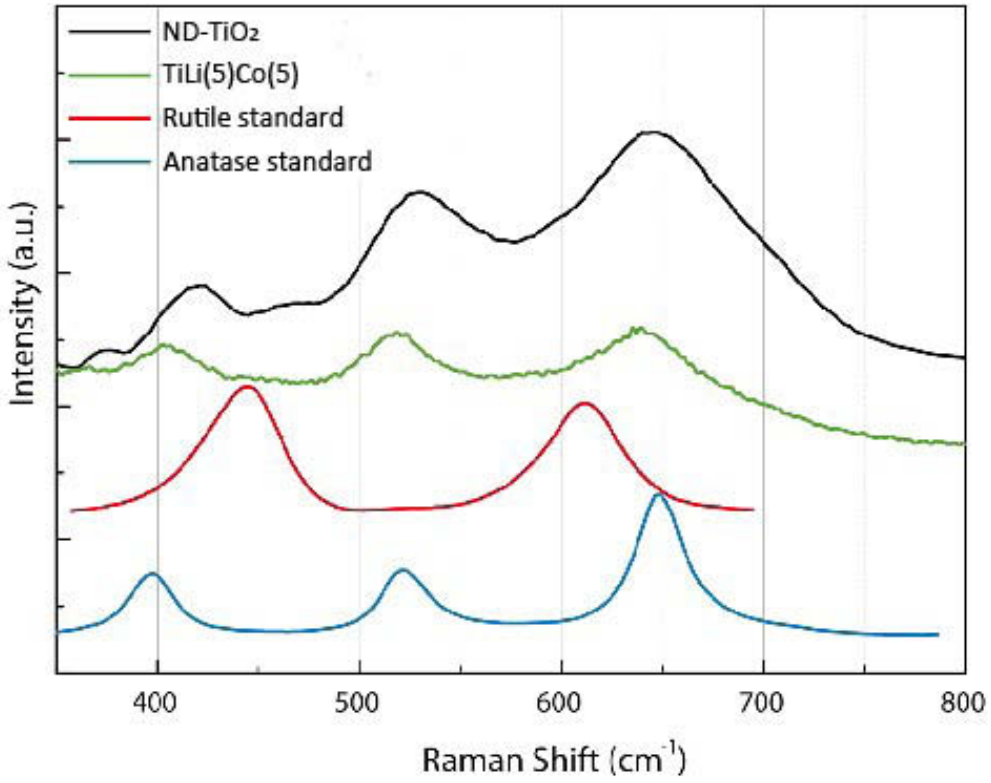

Fig. 27: Comparison of the Raman spectra of the ND-TiO_2 (black), TiLi(5)Co(5) (green), rutile (red) and anatase (blue).

Scanning Electron Microscopy

Electron microscopy characterization allowed us to determine the size and the morphology of the nanoparticles produced with the various synthesis procedures. The measurements were performed on powder samples. The preparation of the samples was sometimes difficult, because nanoparticles are well dispersed in aqueous solution, and tend to form aggregates when dried; consequently, it is very difficult to observe isolated nanoparticles. During the first phase, we used SEM to characterize the synthetized NPs. During the second phase, we chose to use TEM for the NPs, and SEM for the nanosheets.

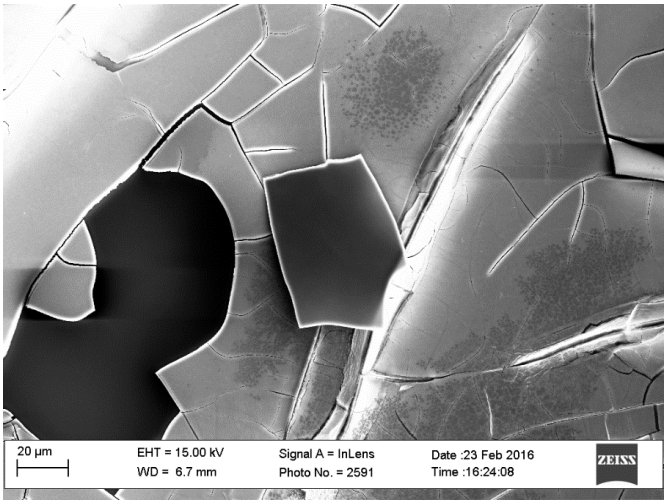

Fig. 28: TiLi(5)Ce(3)-NS nanosheets.

Figs. 28 and 29 show the very fragile structure of the nanosheets we obtained as described above.

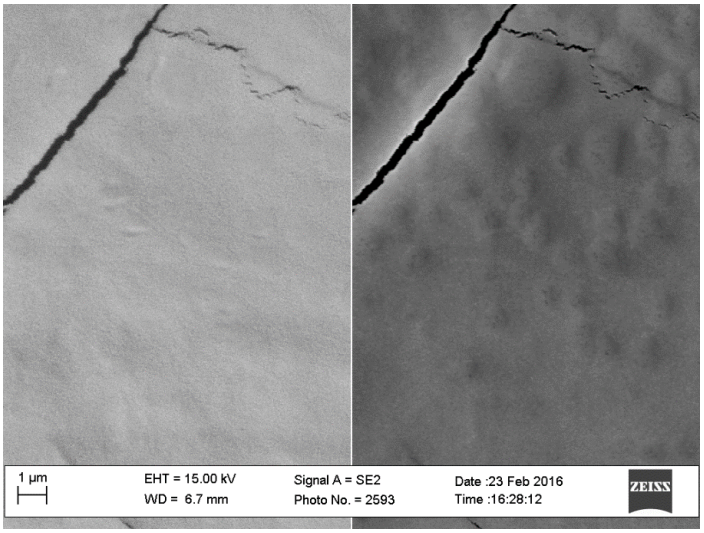

Fig. 29: TiLi(5)Ce(3)-NS nanosheets.

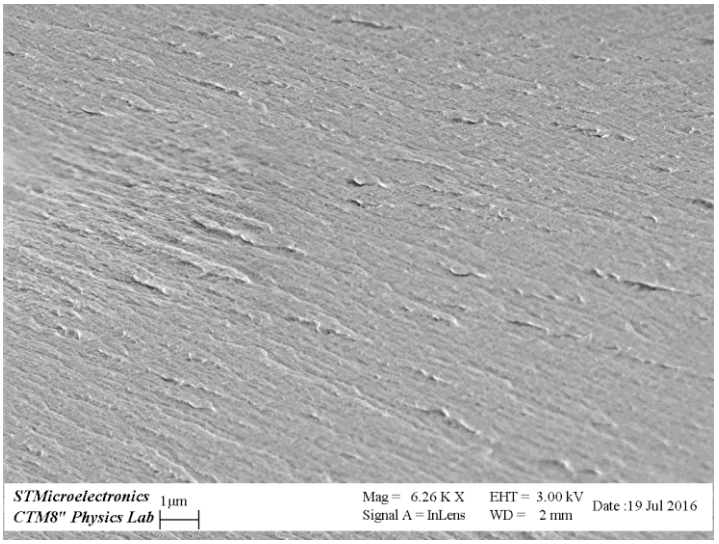

Fig. 30: TiLi(5)Co(5)-NS nanosheets.

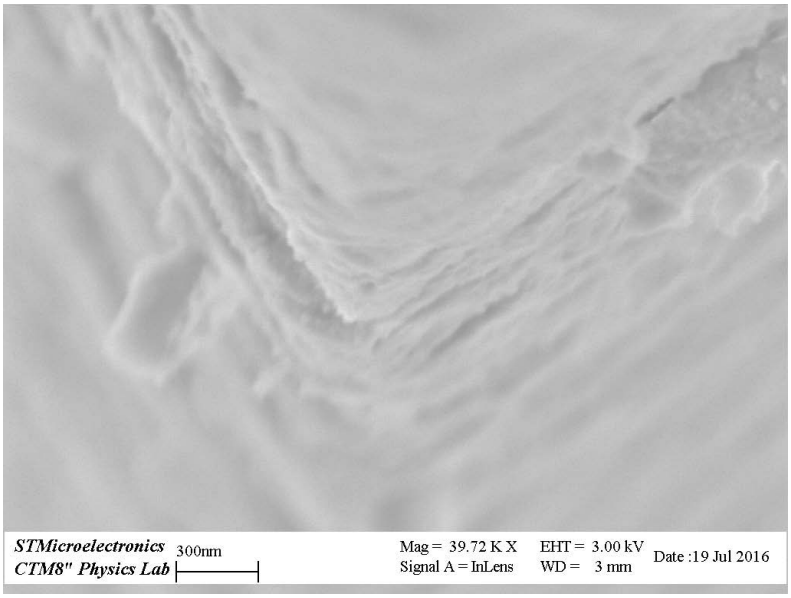

Fig. 31: TiLi(5)Co(5)-NS nanosheets.

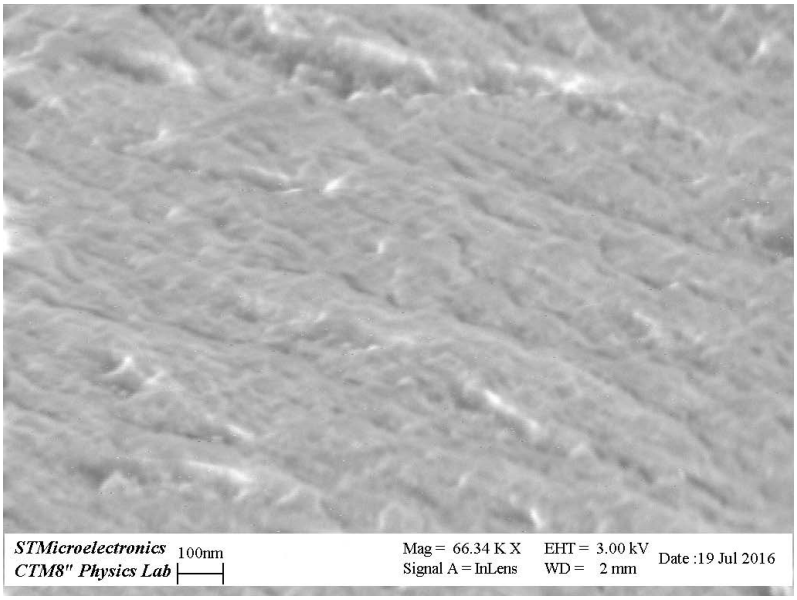

Fig. 32: TiLi(5)Co(5)-NS nanosheets.

Figs. 30, 31 and 32 show the layered structure of the nanosheets from an angular point of view, as well as the surface of the upper sheet. It is important to notice how the layers of this material are not too heavily packed, as this helps increasing the porosity and the relative surface area.

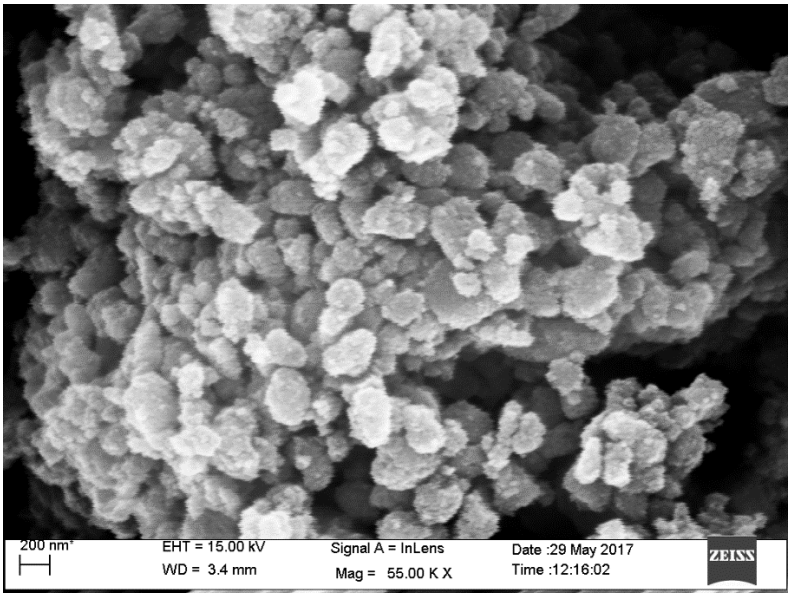

Fig. 33: TiLi(5)W(5) NPs

In fig. 33, small aggregates of particles, between 50 and 100 nm in size, can be observed on the TiLi(5)W(5) sample.

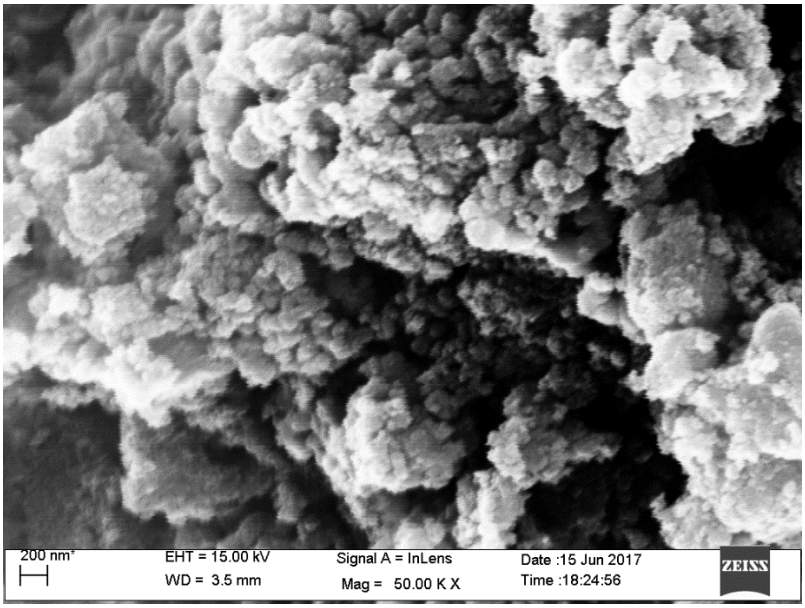

Fig. 34: Au@TiLi(5)

In fig. 34, aggregates of nanoparticles, approximatively 100-150 nm in size, can be noticed on the Au@TiLi(5) sample.

In figs. 35 a, b, c, and d, EDX 2D mapping shows the distribution of Ti, O and W on the TiLi(5)W(5) sample.

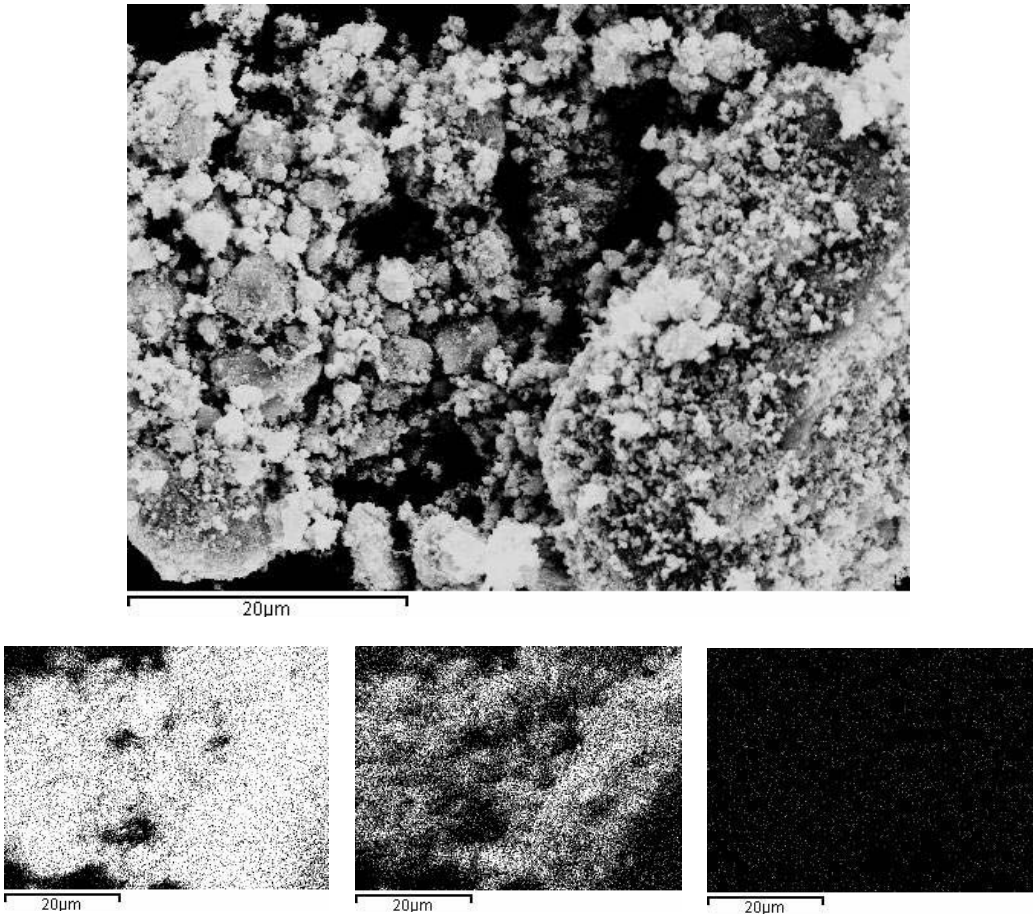

Fig. 35: TiLi(5)W(5) (a) and Titanium (b), Oxigen (c), Tungsten (d) mapping.

Fig. 35 d shows how the tungsten is equally spread over the entire sample, and does not show any sign of segregation.

Figs. 36 a, b shows clearly the nanoporosity in the sample of TiLi(5)Co(5)-aerogel at 80000 and 300000 magnifications.

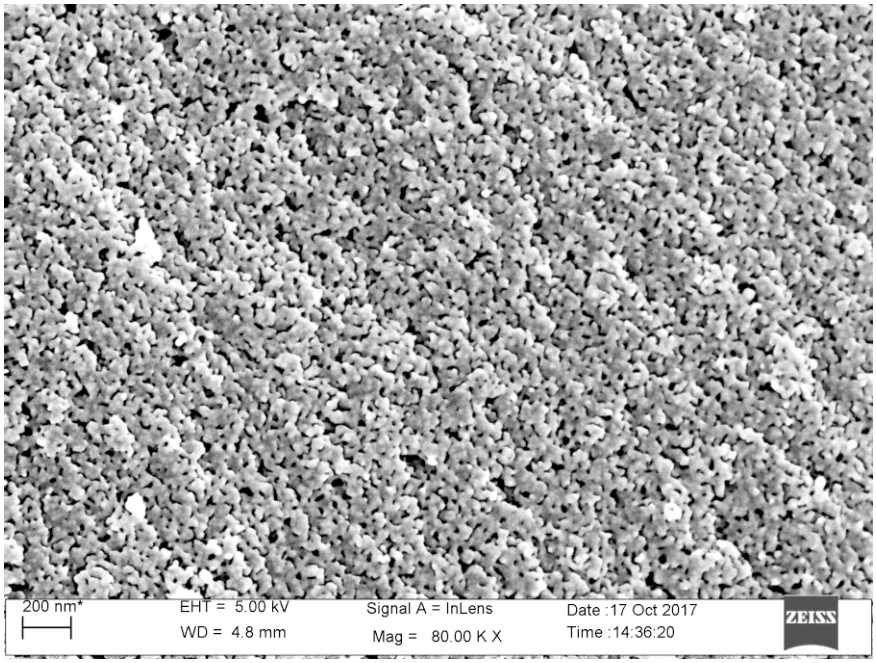

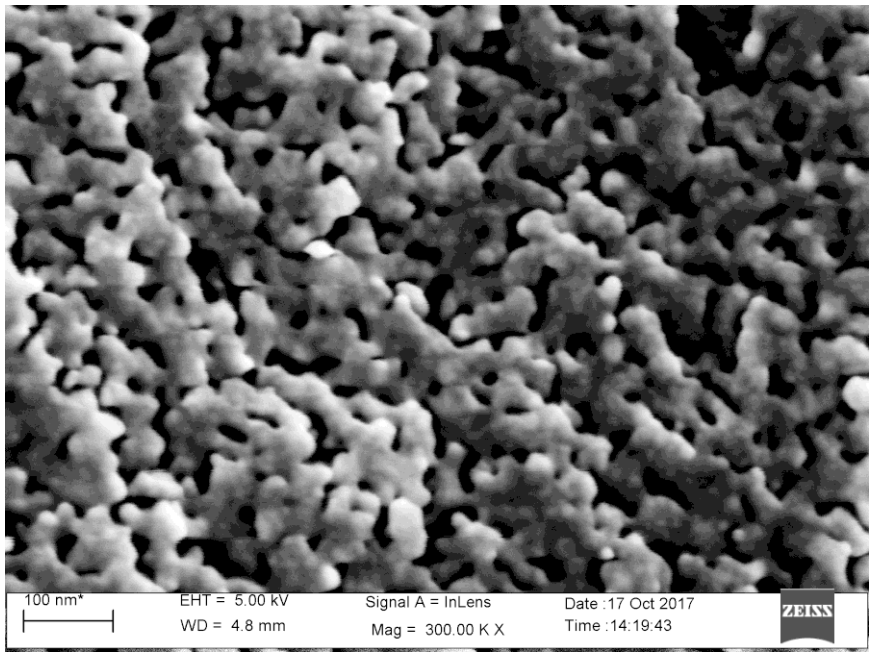

Figs. 36: TiLi(5)Co(5)-aerogel nanoporosity at 80000 (a) and 300000 (b) magnifications

Transmission Electron Microscopy

Figs. 37, 38 and 39 show the morphology of the synthetized NPs. It is possible to see that the dimensions are very uniform, and that the shapes are pseudo-octagonal in most cases. The presence of interference edges makes the nano-crystalline phase is clearly visible in figs. 37b-c, 38b and 39d-e-f. Is it also important to notice the net structure existing between the NPs, resulting from the fact that each NP shares one or more of its facets with another NP.

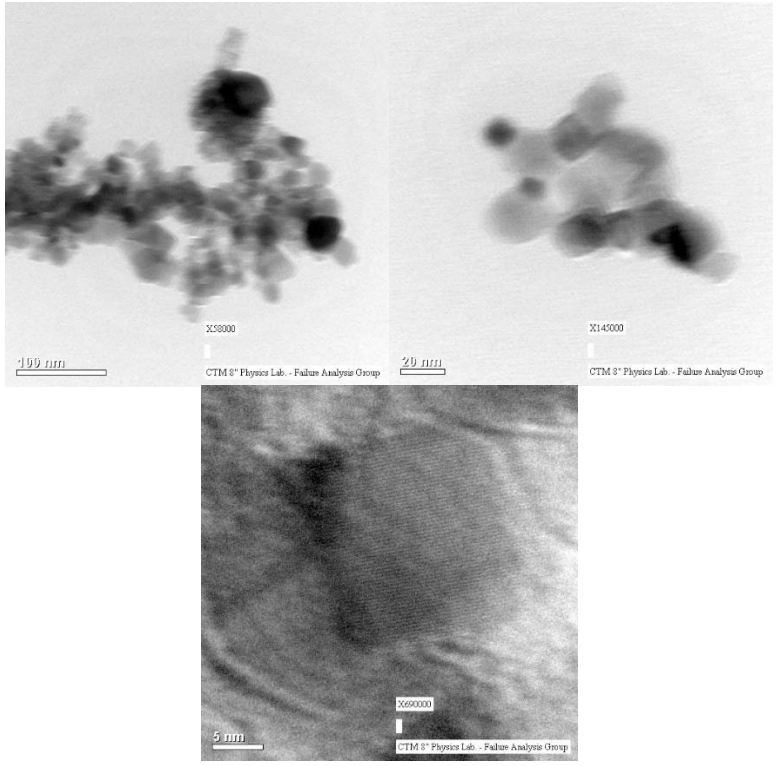

Figs. 37 a, b, c: TiLi(5) NPs.

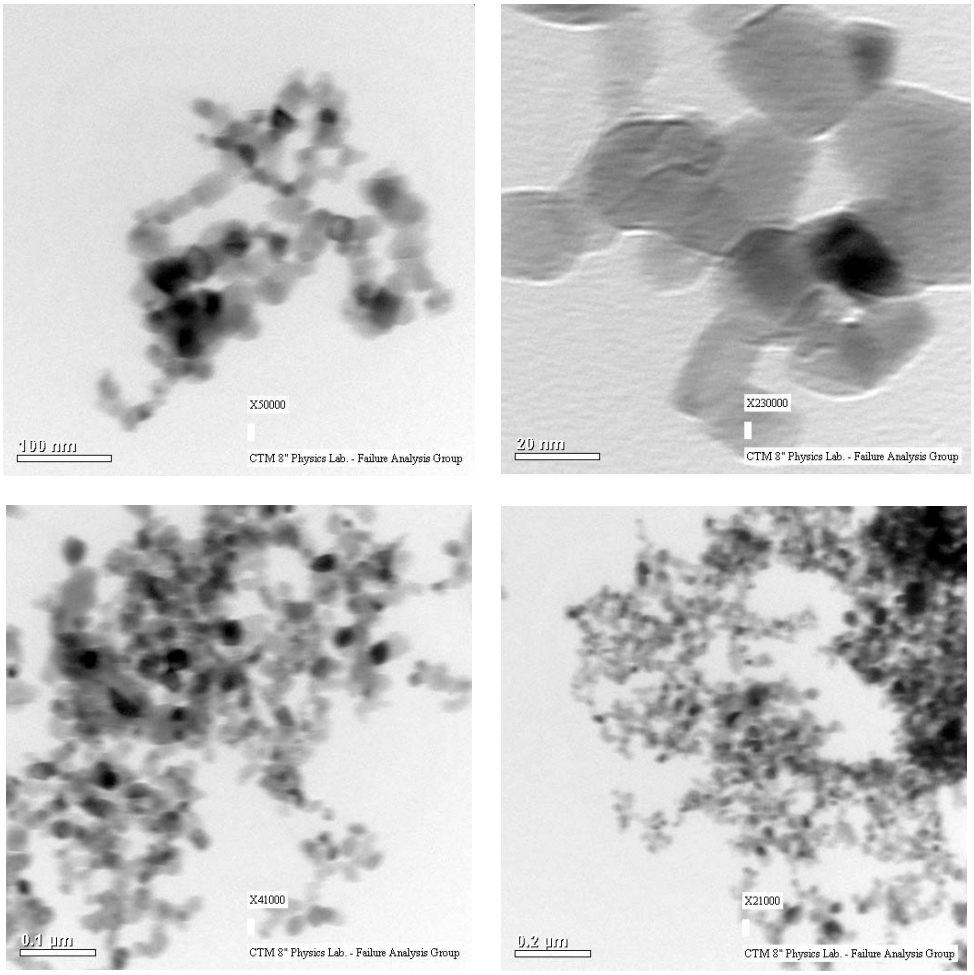

Figs. 38 a, b, c, d: TiLi(5)Ce(5) NPs

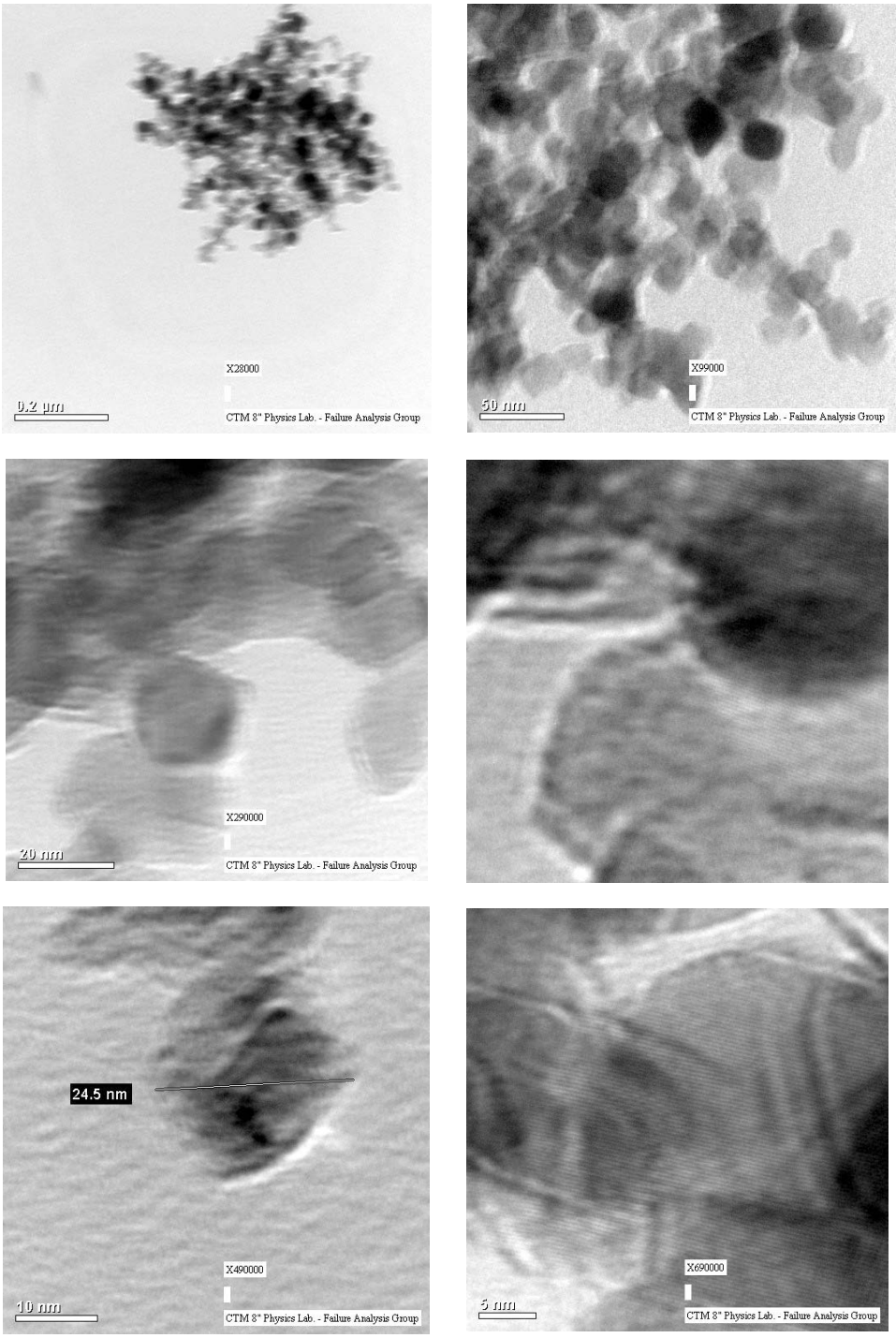

Figs. 39 a, b, c, d, e, f: TiLi(5)Co(5) NPs.

Nitrogen Sorption Isotherms and Brunauer-Emmett-Teller calculation

The specific surface areas and pore size distributions of all the materials were characterized using Nitrogen Gas Sorption. The results were elaborated using the Brunauer–Emmett–Teller (BET) method (58) [117], with further modifications [118] [119] [120]; they are shown in figures 40, 41, and 42.

$$A_s = n_m N_A a \quad (58)$$

where A_s is the surface area, n_m is the number of moles of the adsorbate in a monolayer, and a is the cross-sectional area of the adsorbate molecule. For a more extensive dissertation, we refer to the Condon method [124].

For the commercial TiO_2 (P25), the specific surface area was only 61.1 $m^2\ g^{-1}$, and there was no obvious porous characteristic shown in the corresponding pore size distribution curve that was established according to the Barrett–Joyner–Halenda (BJH) model [121]. This suggests the existence of a dense structure of amorphous hybrid particles. The new materials we synthetized show type IV isotherms [124] with a sharp capillary condensation step at high

relative pressures (P/P_o from 0.7 to 0.9). Moreover, H1 type hysteresis loops were observed for all the nanosheets, but were not as obvious for the nanoparticles; their relatively large pore sizes can be observed in fig. 34 [124] [125]. As summarized in table 2, the best sample was the TiLi(5)Co(5)-nanosheet, with a specific surface area of 446.0 $m^2 g^{-1}$ and a narrow pore size distribution centered at 8.0 nm. The enlargement in pore size, alongside with an increase in crystal size (table 2), resulted in a corollary decrease in specific surface area, from 446.0 to 109.4 $m^2 g^{-1}$.

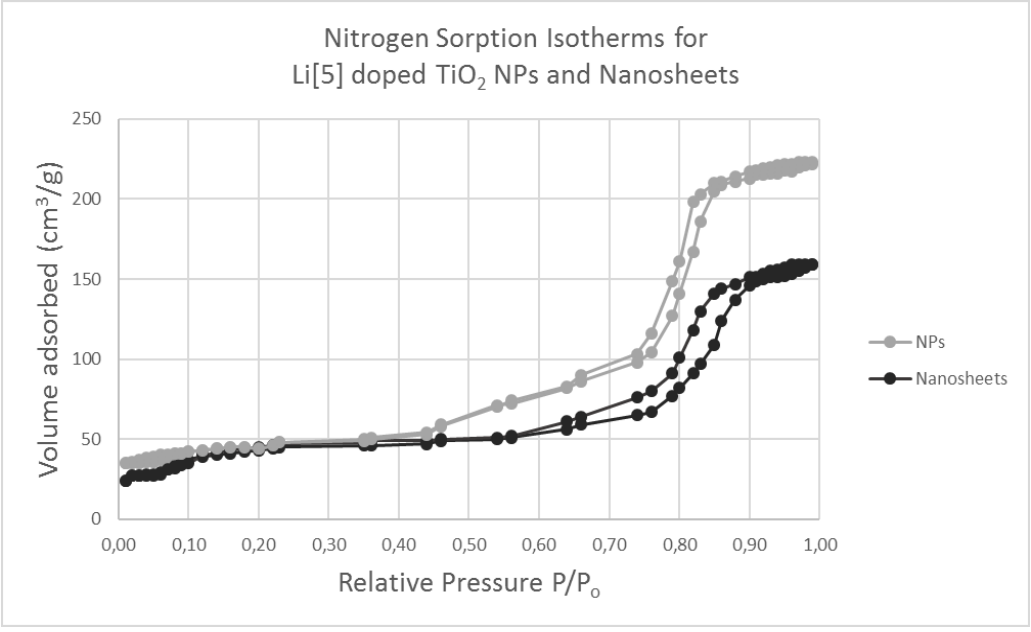

Fig. 40: Nitrogen sorption isotherms for TiLi(5) NPs and Nanosheets.

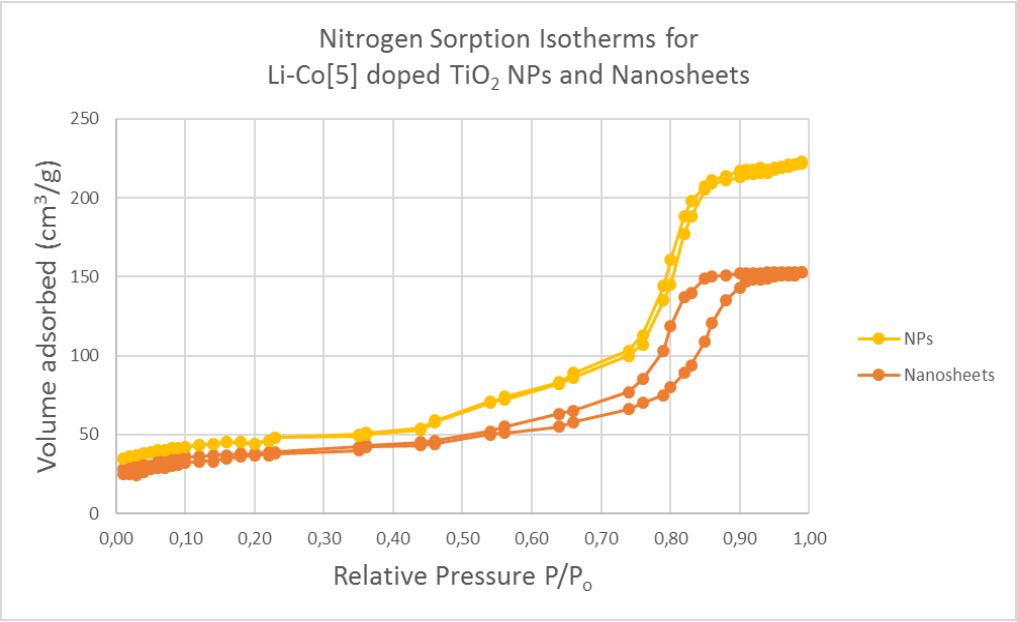

Fig. 41: Nitrogen sorption isotherms for TiLi(5)Co(5) NPs and Nanosheets.

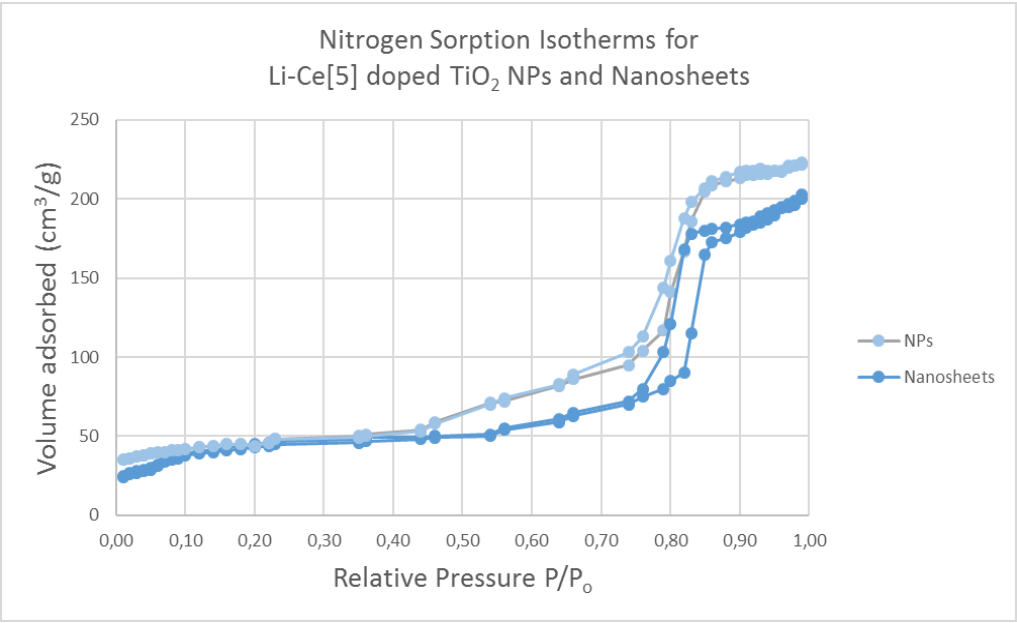

Fig. 42: Nitrogen sorption isotherms for TiLi(5)Ce(5) NPs and Nanosheets.

Table 2: Surface area and Pore size calculated by different techniques

Sample	Surface area (m^2g^{-1})	Pore size (nm) BET	Pore size (nm) XRD	Pore size (nm) SEM
ND-TiO_2 (control sample)	61.1 ± 0.2	28.3 ± 0.1	24.1 ± 0.3	29.2 ± 1.2
TiLiCl(5)	109.4 ± 0.6	19.4 ± 0.2	17.2 ± 0.2	21.4 ± 1.1
TiLi(5)	123.2 ± 0.6	21.5 ± 0.2	19.2 ± 0.2	20.8 ± 1.0
TiLi(5)Co(5)	162.4 ± 0.8	17.3 ± 0.3	13.7 ± 0.3	18.8 ± 1.0
TiLi(5)Ce(5)	141.8 ± 0.7	16.1 ± 0.2	12.2 ± 0.2	17.4 ± 0.9
TiLi(5)-nanosheets	288.9 ± 0.8	11.1 ± 0.3	10.7 ± 0.2	12.6 ± 0.8
TiLi(5)Co(5)-nanosheets	446.0 ± 0.9	8.0 ± 0.4	7.1 ± 0.1	9.8 ± 0.9
TiLi(5)Ce(5)-nanosheets	315.4 ± 0.8	9.8 ± 0.3	8.4 ± 0.2	10.8 ± 0.9

Zeta Potential

The Zeta potential is one of the main factors defining the behavior of suspended particles. In effect, it constitutes an important index of the intensity of the repulsive forces existing between the particles, and can be useful for understanding the stability of the colloidal suspension [126].

Electrical double-layer

A dispersed particle in a liquid generally has electrostatic surface charges, which create an electric field responsible for the redistribution of the ions present in the space surrounding the particle [126].

The electrical double-layer is defined as the layer of liquid containing the ions surrounding the particle, and is composed of two distinct regions. In the inner region, known as the stationary layer or *Stern layer*, the opposing ions are strongly bound to the charged particle, while in the outer region, called diffuse layer or *Gouy-Chapman layer*, these interactions are weaker. The latter is constituted by ions of both signs but with a predominance of the ions that also form the *Stern layer*. This prevalence is more marked near the stationary

layer, and decreases towards the end of the diffuse layer. In effect, the end of the latter is represented by the point where there is a perfect balance between the two opposite charge ions. Moving away from the surface of the particle, this balance will obviously be maintained. As can be seen in fig. 43, these two regions form a double layer around each particle. In particular, within the diffused layer, ions form metastable structures so that when the particle moves into the fluid, the ion that is located within the boundary called the *slipping plane* will move with it as a single object.

Conversely, the ions located outside the *Stern layer* are continuously replaced by the free ions present in the liquid. The diffused layer, as shown in fig. 43, can be divided into two parts. The innermost layer, rich in *Stern layer* charges, is always bound to the particle, whereas the outer layer is not bound to the colloid particle; it is therefore called a mobile layer. The interface separation point is known as the *slipping plane*, so called because only the inner layer will move with the colloid if a tangential force is applied [126].

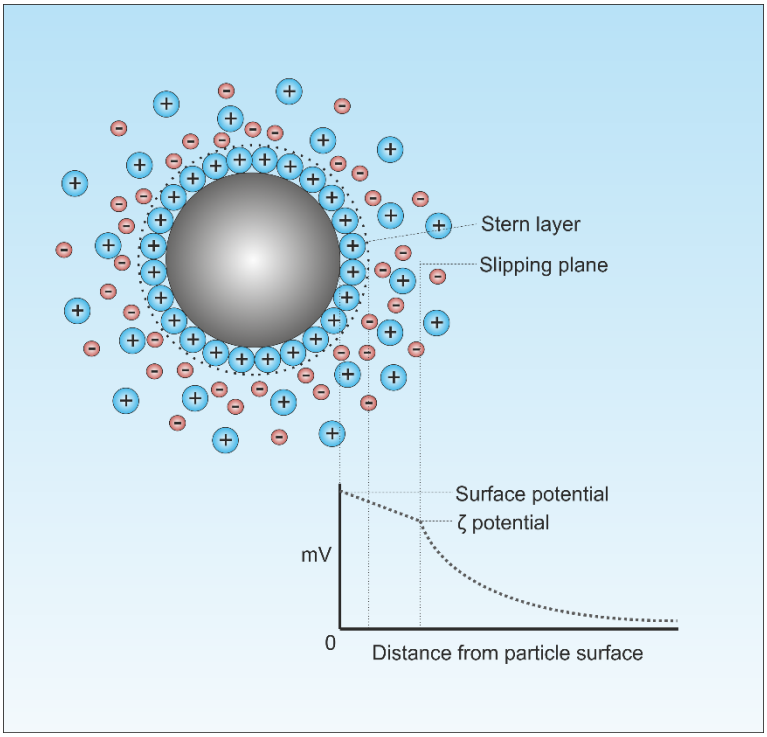

Fig. 43: Representation of the double-layer, the slippling plane, its correlation to zeta potential and the variation of electric potential related to the distance from particle surface.

In fig. 43, it is possible to observe the trend of the electrical potential generated by the formation of the double layer, starting from the surface of the particle down. The electrical potential assumes a certain value at the surface of the particle, depending on its charge, which decreases as it moves away from the surface, as a result of the higher concentration of the opposing charge ions. This phenomenon occurs because the opposite end of the diffused layer returns to

neutrality, which generates a potential difference between the various layers and the bulk solvent. We can distinguish:

- Surface potential: the difference in potential between the surface of the colloid and the bulk solvent;

- Stern Potential: difference in potential between the Stern layer and the bulk solvent;

- Zeta potential: difference in potential between the *slipping plane* of the diffused layer and the bulk solvent.

It can be seen, therefore, how the value of the electrical potential at first decreases rapidly within the stationary layer, and then decreases at a gradually slower rate within the diffused layer and beyond until it is annulled tending toward infinity by definition. Within the diffused layer, the potential measured at the slipping plane is known as the Zeta potential (ζ) [126]. It represents the potential attributed to the particle and to its charge. This potential gives us information on the stability of the colloid, and allows us to estimate the critical concentration threshold at which the nanoparticles tend to agglomerate.

Stability of a colloid solution

The presence and the magnitude of the charges located on particles dispersed in a liquid constitutes an important factor for the stability of colloidal systems. The zeta potential is a measure of the repulsive force between the particles, and also an indicator index of the stability of the colloids. When the value of the zeta potential falls below 30mV, the system becomes unstable. The particles tend to aggregate, since the forces of attraction begin to prevail when two particles get close to one another during their Brownian movements.

Derjaguin, Landau, Verwey, and Overbeek developed a theory of the stability of colloidal systems [127] [128], called DLVO. The authors claim that the stability of a particle in a solution is function of its total potential energy VT, which is determined by different contributions, as shown in the equation (59):

$$VT = \mathrm{VA} + \mathrm{VR} + \mathrm{VS} \quad (59)$$

where VS is the potential energy of the solvent, which usually leads to a marginal contribution to the total potential energy, and only

close to the separation surface. Most important is the relationship between VA (attractive contributions) and VR (repulsive contributions), in which the zeta potential is involved. The DLVO theory states that the stability of a colloidal system is determined by the comparison between the attractive forces of *London-Van der Waals* (VA) and the particle (VR) surrounding electric double layer repulsion forces that become important when two or more particles, due to their Brownian motion, get so close to one another that their electric double-layers overlap. According to this theory, there is a potential barrier, resulting from repulsive forces, which prevents two particles from aggregating. However, if the particle collision energy can overcome the potential barrier, the forces of attraction bring the particles into an indissoluble contact. This model is valid only in the case of spherical and smooth particles immersed in water [129].

The zeta potential value provides information on the stability of colloidal systems. If all the suspended particles possess a high negative or positive potential, then they tend to repel one another and to become more stable, with a low tendency to aggregate. Instead, if particles exhibit a low zeta potential, flocculation

becomes easier. Generally, preparations with an absolute zeta potential of approximately 30mV are considered stable.

As a result, when the dispersion of the nanoparticles is desired, the goal is to maximize the value of that zeta potential, which depends on several factors. Theoretical studies and experimental results have shown that the value of the zeta potential is influenced not only by the conditions of the suspension, such as pH, temperature, ionic strength, and type of ions, but also by the intrinsic properties of the particle, such as the size and the concentration [130]. Bourikas et al. demonstrated that the position of the slipping plane was linearly dependent, on a logarithmic scale, on the value of ionic force [131].

Among the factors that strongly affect the stability of colloid systems made up of nanoparticles, the pH is one of the most important. Dispersed TiO_2 particles in water are generally coated by hydroxyl groups (60):

$$Ti^{4+} + H_2O \rightarrow Ti^{4+}OH^- + H^+ \quad (60)$$

The surface charge of the particles is function of the pH of the solution, which influences the reactions occurring at the surface of the particles, as shown by reactions (61) and (62) [132].

$$TiO^- + H^+ \rightleftarrows TiOH \qquad (61)$$

$$TiOH + H^+ \rightleftarrows TiOH_2^+ \qquad (62)$$

The pH value for which the TiO_2 NPs surface is free of charge, and therefore neutral, and for which the zeta potential is null defines the isoelectric point (IEP) of the dispersed system. The isoelectric point is a property of the surface of the particle, and is the value around which there is little stability, since the Van der Waals forces are more influential. When the pH of the solution is lower than the pH value at the isoelectric point, there will be a positive charge at the surface of the nanoparticles, and, consequently, a positive zeta potential. Conversely, for a pH value greater than the isoelectric point, we will have particles with a negative surface charge and a negative zeta potential [133].

Zeta Potential Measurements

Zeta potential measurements were made using nanoparticle dispersions at different concentrations. We started with a concentration of 0.750 g/L, and progressively diluted it to avoid the saturation of the electrodes.

The first measurement, reported in fig. 44, shows the zeta potential of any impurities present in the Millipore water used to disperse the nanoparticles. As it can be seen from the graph, the potential is well centered at the value of 0 mV.

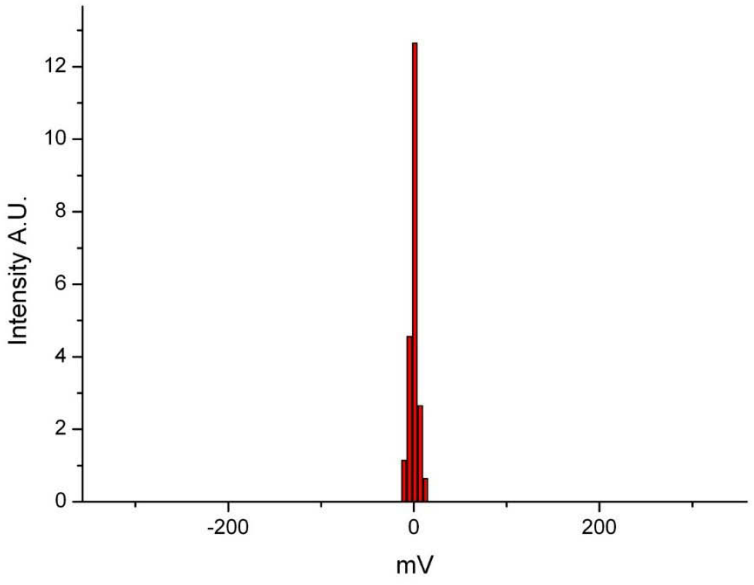

Fig. 44: zeta potential in Millipore water.

The histogram shown in fig. 45 refers to the dispersion in aqueous solution of the ND-TiO_2 nanoparticles, for an initial concentration of 0.750 g/L. The curve seems to have a Gaussian distribution centered around the value of +38 mV. This value is in agreement with literature data indicating the minimum value needed to obtain dispersed nanoparticles is +30 mV [126] [132]. These data confirmed the experimental evidence on the stability of the suspensions, which were still stable several months after the initial observation.

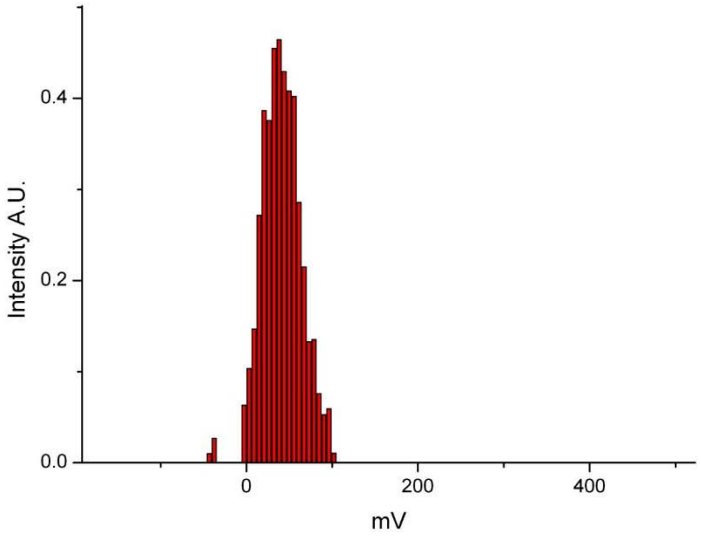

Fig. 45: Zeta potential of the ND-TiO_2 suspension at a concentration of 0.750 g/L.

Fig. 46 shows the histogram for the zeta potential measurement performed on another suspension of a ND-TiO_2 sample, which was diluted ten times with respect to the previous case. We can see how, in this case, the distribution of zeta potential values is less spread, and how the maximum value is located at +57 mV. This is caused by the lower concentration of suspended particles, associated with a lower chance of saturation of the electrodes.

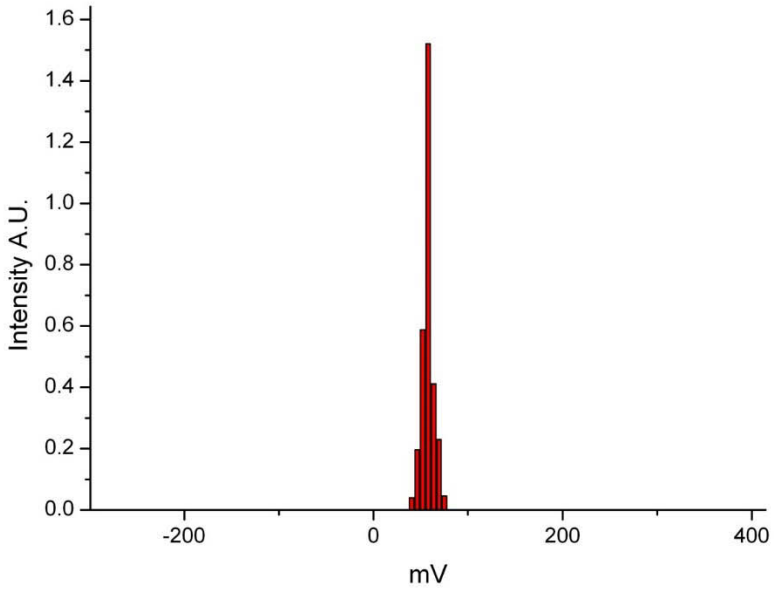

Fig. 46: Zeta potential of the ND- TiO_2 suspension at a concentration of 0.075 g/L.

After carrying out potential measurements on non-doped samples, we analyzed the lithium doped samples in order to verify their capacity to keep the nanoparticles in dispersion.

Fig. 47 shows the measurement made on the TiLi(3) sample at a concentration of 0.750 g/L. Even in this case, we can notice a Gaussian distribution with predominant values of +78 and +107 mV. These values are higher than those reported in the case of ND-TiO_2, demonstrating that the Li^+ ions adsorbed at the surface of the particles can give them a charge such as to guarantee electrostatic repulsion.

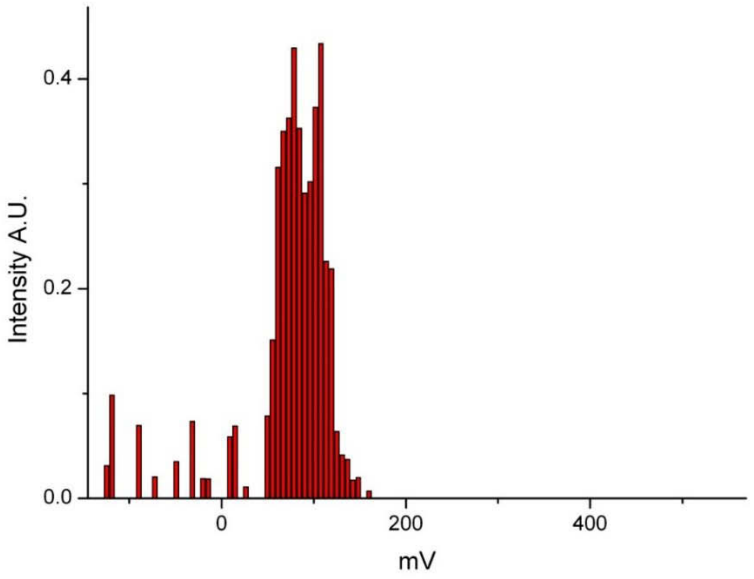

Fig. 47: Zeta potential of the TiLi(3) suspension at a concentration of 0.750 g/L.

Fig. 48 shows the measurement of zeta potential performed on a suspension of TiLi(3) NPs diluted ten times as compared to the previously analyzed sample (0.075 g/L). In this case, the distribution is centered on the maximum value of +92 mV. This value is much higher than the +30 mV value reported in the literature as the minimal threshold value required to obtain a stable nanoparticle suspension.

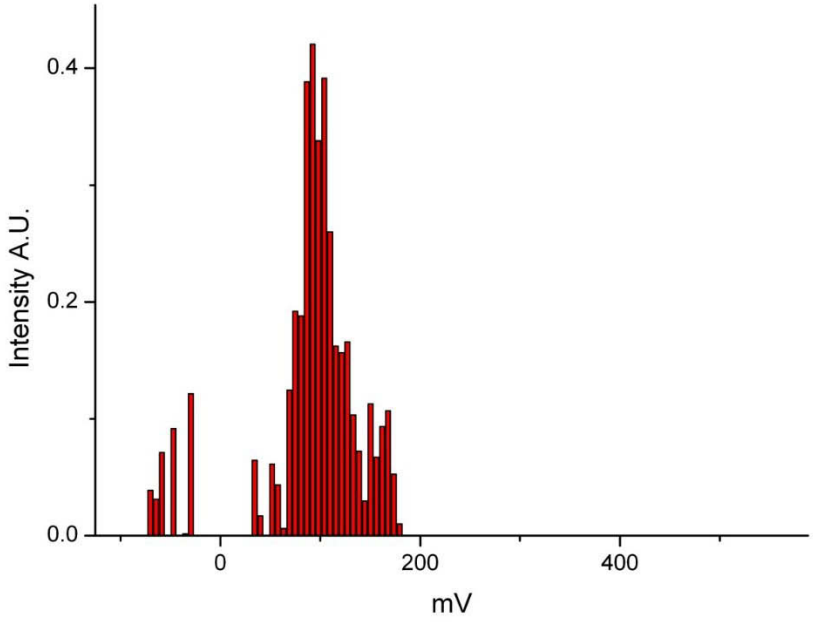

Fig. 48: Zeta potential of the TiLi(3) suspension at a concentration of 0.075 g/L.

We also carried out a test on the co-doped sample TiLi(5)Co(5), as reported in fig. 49. In this case, the distribution appears similar to the distribution exhibited by the samples doped only with lithium, with a maximum value of +110 mV. The similarity with TiLi(3) samples indicates that this ion allows the dispersion of nanoparticles, and does not conflict with any co-dopants that are located inside the system.

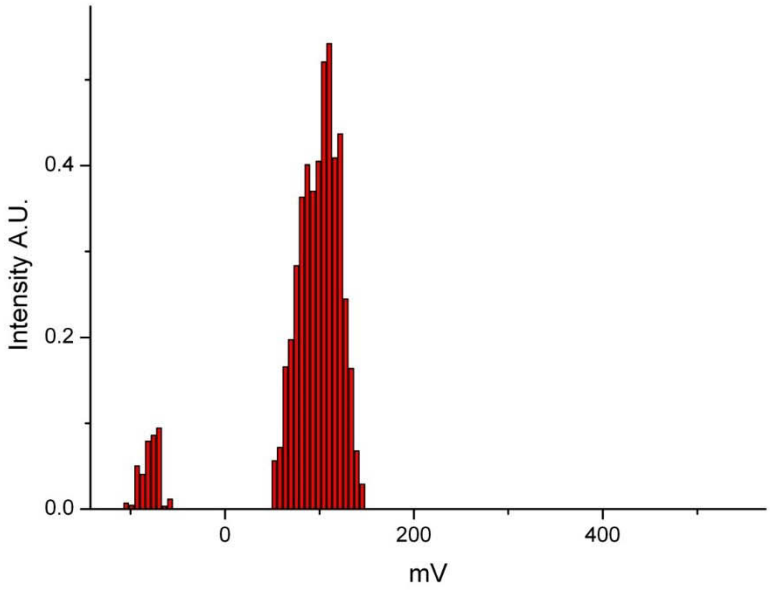

Fig. 49: Zeta potential of the TiLi(5)Co(5) suspension at a concentration of 0.750 g/L.

^{7}Li MAS NMR spectroscopy

Samples for ^{7}Li MAS NMR spectroscopy analysis were prepared in a dry box in N_2 atmosphere, inserted in 4 mm zirconia rotors with the available volume reduced to 20 µl, and sealed with kel-F caps.

^{7}Li magic angle spinning (MAS) NMR (I=3/2, 92.6% abundance) spectra were recorded at 155.50 MHz on a Bruker Advance 400 spectrometer. The π/2 pulse width was 5.5 µs. Spectra were acquired with a time domain of 4 k data points, zero filled, and Fourier transformed with a size of 16 k data points. The spin-rate was kept at 5500 Hz. The ppm scale was made using LiCl as an external reference. The longitudinal relaxation time T_1 was measured using the saturation recovery pulse sequence [134]. The measurement of the longitudinal relaxation times allowed the optimization of the recycle delay to be used for collecting ^{7}Li spectra. The transverse relaxation time T_2 was determined using the quadrupolar Carr-Purcell-Meiboom-Gill (QCPMG) pulse sequence [135].

Figs. 50 a, b, and c shows ^{7}Li MAS spectra of LiCl (a), TiO_2 nanoparticles synthesized with LiCl (TiLiCl(5) synthesis) (b), and TiO_2 nanoparticles synthesized with LiCl+HNO_3 (the TiLiCl-acid

intermediate) (c). The spectrum of LiCl shows a peak at 0 ppm with a linewidth of about 287 Hz. The spectrum of TiO_2 nanoparticles synthesized with LiCl shows a peak at -0.05 ppm, with a linewidth of 10 Hz indicating the high mobility of lithium ions (fig. 36b). The spectrum of the TiO_2 nanoparticles that were synthesized with LiCl + HNO_3 was deconvoluted to obtain a sharp and a broad peak centered at -0.08 and -0.06 ppm, respectively. The line width of the sharp peak was found to be 6 Hz, whereas that of the broad one was 37 Hz; see the insert in fig. 1c. In this case, the broad peak was ascribed to Li^+ interacting with H^+ at the nanoparticles surface, whereas the sharp peak was ascribed to the other Li^+ moving at the surface of the nanoparticles and inside the porous matrix of the nanoparticles.

To investigate Li^+ mobility, the longitudinal (T_1) and the transverse (T_2) relaxation times were measured.

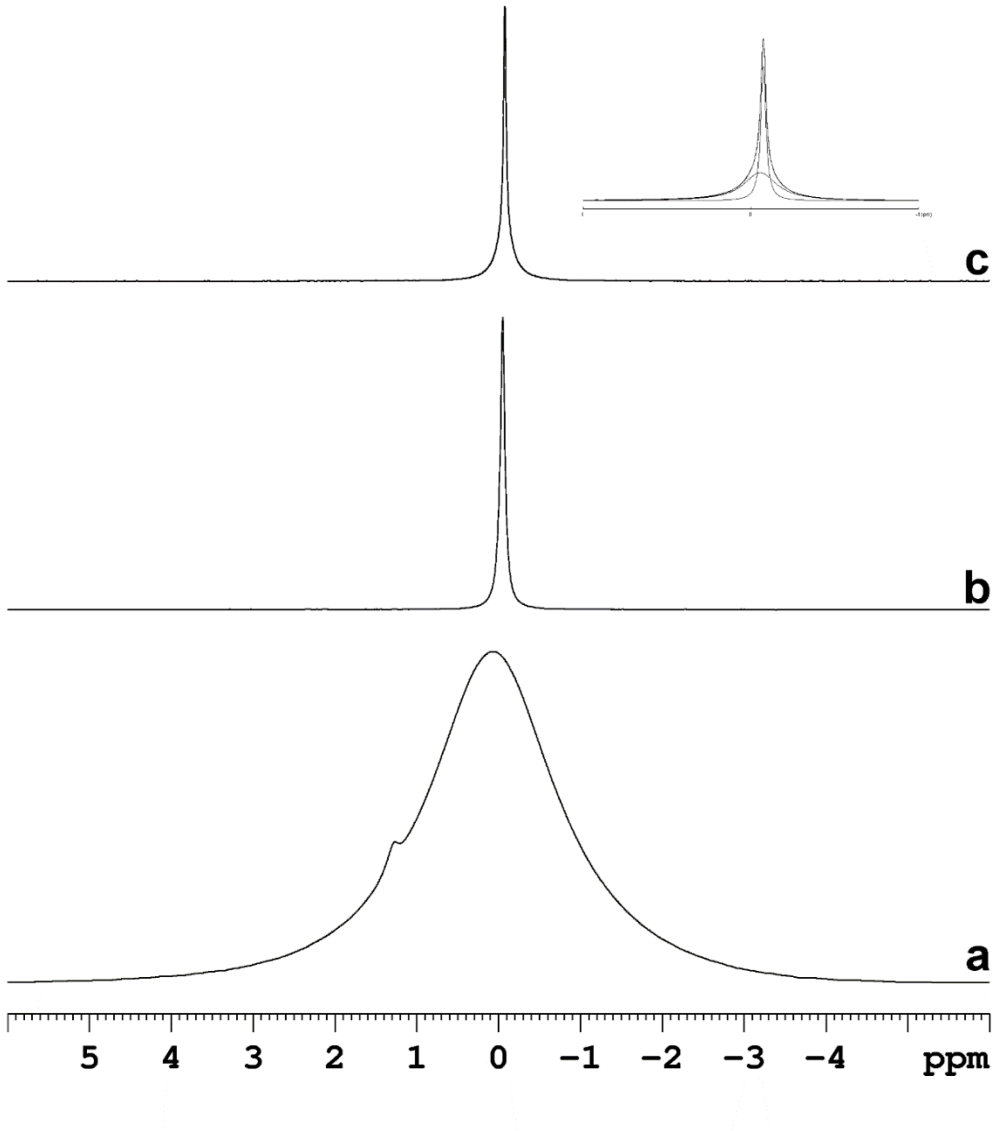

Figs. 50 a, b, c: ^{7}Li MAS spectra of a standard of LiCl (a), TiO_2 nanoparticles synthesized with LiCl, TiLiCl(5) synthesis) (b), and TiO_2 nanoparticles synthesized with LiCl + HNO_3 (TiLiCl-acid intermediate) (c). The deconvolution of the spectrum of TiLiCl-acid intermediate is reported in the insert.

Figs. 51 and 52 report the longitudinal relaxation decays of ^{7}Li magnetization measured in LiCl and Li-doped TiO_2 NPs, and in Li-doped TiO_2 xerogel. In all samples, a mono-exponential decay of the longitudinal magnetization $M_z(t)$ vs. time was obtained. T_1 values reported in table 3 were obtained fitting experimental data to the following equation (63):

$$M_z(t) = M_{z,\mathrm{eq}} - \left[M_{z,\mathrm{eq}} - M_z(0)\right] e^{-t/T_1} \qquad (63)$$

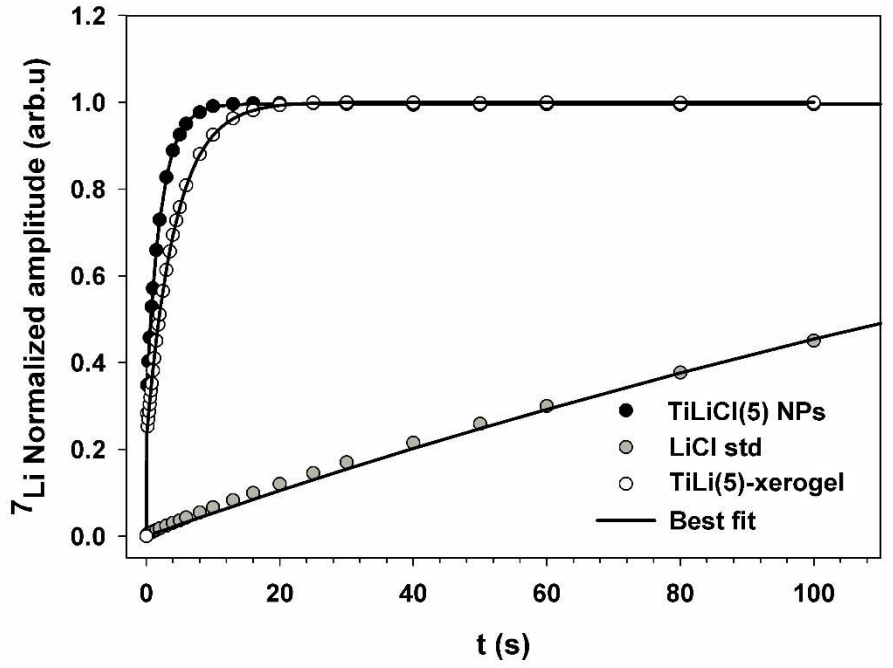

Fig. 51: Longitudinal relaxation decay measured in LiCl (grey circles), Li-doped TiO_2 NPs, TiLiCl(5) synthesis (black circles) and Li-doped TiO_2 xerogel, TiLi(5)-xerogel (white circles).

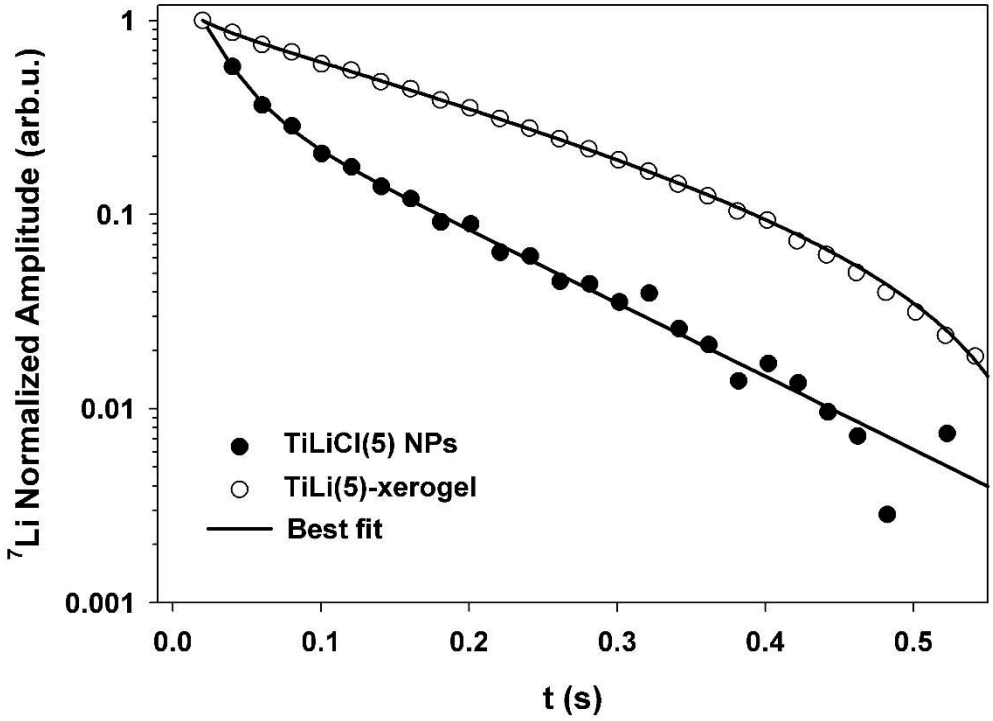

Fig. 52: Longitudinal relaxation decay measured in Li-doped TiO_2 NPs, TiLiCl(5) synthesis (black circles) and Li-doped TiO_2 xerogel, TiLi(5)-xerogel (white circles) in logarithmic scale.

Table 3. Longitudinal relaxation times measured in LiCl and in TiLiCl(5) nanoparticles.

Sample	T_1(s)	R^2
TiLiCl(5)	2.160±0.010	0.9999
TiLiCl-acid intermediate	2.168±0.018	0.9999
TiLi(5)-xerogel	4.330±0.061	0.9992
LiCl standard	>268	0.9999

It is worth noting that ^{7}Li exhibited a definitely higher mobility in TiLiCl(5) NPs (about 2.2 s) and in TiLi(5)-xerogel (about 4.3 s) than in LiCl, which was used as precursor during the synthesis (> 268 s).

In order to evaluate the presence of different lithium domains and their relative motions, transverse relaxation times were measured. With respect to T_1, T_2 yields a more detailed information on molecular motions occurring in domains with reduced dimensions. In effect, in the case of TiLiCl(5) NPs, the decay of the longitudinal magnetization was averaged out to a mono-exponential decay, whereas the transverse magnetization showed a bi-exponential decay corresponding to two distinct values of the transverse relaxation time. T_2 values reported in table 4 were obtained fitting experimental data to the equation 64:

$$\mathrm{M}_{xy}(t) = \mathrm{M}_{01}\ \mathrm{e}^{\left(-\mathrm{t}/\mathrm{T}_{21}\right)} + \mathrm{M}_{02}\ \mathrm{e}^{\left(-\mathrm{t}/\mathrm{T}_{22}\right)} \qquad (64)$$

where M_{01} and M_{02} are the spin densities of the two components corresponding to two lithium domains, and T_{21} and T_{22} are the transverse relaxation times of each component. Therefore,

transverse relaxation time measurements allowed the detection of two Li^+ domains and the evaluation of the relative amount of Li^+ in each domain.

Table 4. Transverse relaxation times measured in Li-doped TiO_2 nanoparticles.

Sample	M_{01}	T_{21}(s)	M_{02}	T_{22}(s)	R^2
TiLiCl(5)	0.76	0.022±0.001	0.24	0.111±0.006	0.9993
TiLiCl-acid intermediate	0.46	0.010±0.010	0.54	0.069±0.003	0.9970
TiLi(5)Co(5)	0.67	0.025±0.001	0.33	0.098±0.004	0.9979
TiLi(5)-nanosheets	0.28	0.124±0.003	0.72	0.176±0.003	0.9998
TiLi(5)-xerogel	0.17	0.017±0.005	0.83	0.203±0.004	0.9997

The fast relaxing component was assigned to Li^+ at the surface of nanoparticles, and the slow relaxing one to Li^+ ions confined into the porous nanoparticles. In the case of TiLiCl(5) nanoparticles, the amount of Li^+ ions at the surface of the nanoparticles was found to be higher at the surface (76%) than inside the nanoparticles (24%), whereas in the case of TiLiCl-acid intermediate nanoparticles the presence of H^+ ions at the surface of the nanoparticles possibly reduced the presence of Li^+ ions moving at the surface of the nanoparticles (46%). In the case of TiLi(5)-xerogel nanoparticles, the amount of Li^+ ions moving atthe surface of the nanoparticles was

found to be strongly reduced (17%) compared to the amount of Li^+ ions inside the nanoparticles (83%).

T_2 relaxation time and diffusion measurements as a function of temperature will allow a detailed investigation of Li^+ motions in Li-doped TiO_2 nanoparticles.

Fig. 53 reports the longitudinal relaxation decays of ^7Li magnetization measured in TiLi(5)-nanosheets, in TiLi(5)Co(5), and in $LiNO_3$ that it was used as precursor in these samples. In $LiNO_3$, a bi-exponential decay of the longitudinal magnetization Mz(t) vs time was obtained. In TiLi(5)-nanosheets and in TiLi(5)Co(5) a mono-exponential decay of the longitudinal magnetization was found (table 5).

Table 5. Longitudinal relaxation decay measured in TiLi(5) and TiLi(5)Co(5) nanoparticles.

Sample	T_1(s)	R^2
TiLi(5)-nanosheets	4.33±0.06	0.9992
TiLi(5)Co(5)	2.168±0.018	0.9999

Sample	T_{1A}(s)	M_{1A}	T_{1B}(s)	M_{1B}	R^2
$LiNO_3$ std	115±27.03	0.56	2.38±0.51	0.44	0.9999

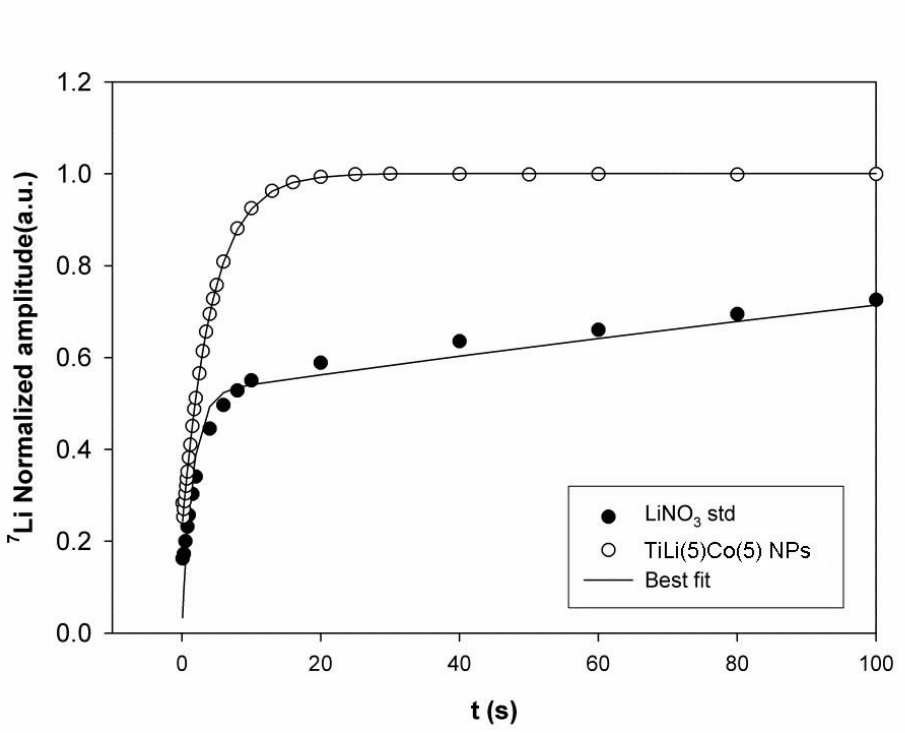

Fig. 53: Longitudinal relaxation decay measured in $LiNO_3$ (black circles) and Li-doped TiO_2 nanoparticles with $CoCl_2$ and $LiNO_3$ (white circles).

Also in this case, ^{7}Li exhibited a definitely higher mobility in TiLi(5) NPs than in $LiNO_3$, which was used as precursor.

To evaluate the presence of different lithium domains and their relative motions, transverse relaxation times were measured.

Table 6. Transverse relaxation times measured in Li-doped TiO_2 nanoparticles.

Sample	T_2(s)	R^2
TiLi(5)-nanosheets	0.164±0.005	0.9954
TiLi(5)Co(5)	0.025±0.001	0.9879

In all samples, the transverse magnetization showed a mono-exponential decay. T_2 values reported in table 6 were obtained fitting experimental data to the equation (65):

$$\mathrm{M}_{xy}(t) = \mathrm{M}_{\mathrm{xy}}(0)\ \mathrm{e}^{\left(-\mathrm{t}/\mathrm{T}_2\right)} \quad (65)$$

In order to better understand the lithium domains, their motion and the behavior of the materials we measured T_1 and T_2 as functions of temperature.

In figs. 54 a, b, and c T_1 as function of temperature is reported for samples TiLi(5) NPs, $TiLiNO_3$-acid intermediate NPs, and TiLi(5)Co(5) NPs.

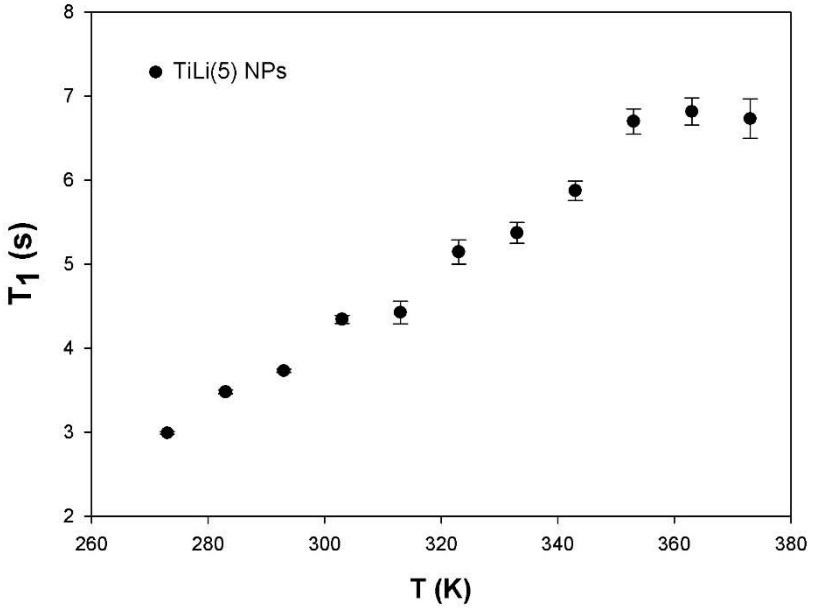
TiLi(5) NPs
T1 (s)
T (K)
8
7
6
5
4
3
2
260
280
300
320
340
360
380

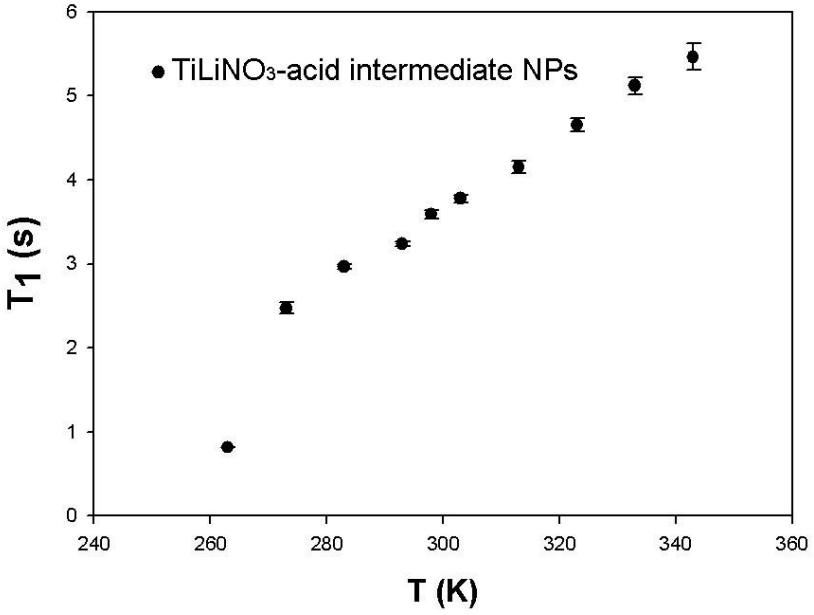
TiLiNO3-acid intermediate NPs
T1 (s)
T (K)
6
5
4
3
2
1
0
240
260
280
300
320
340
360

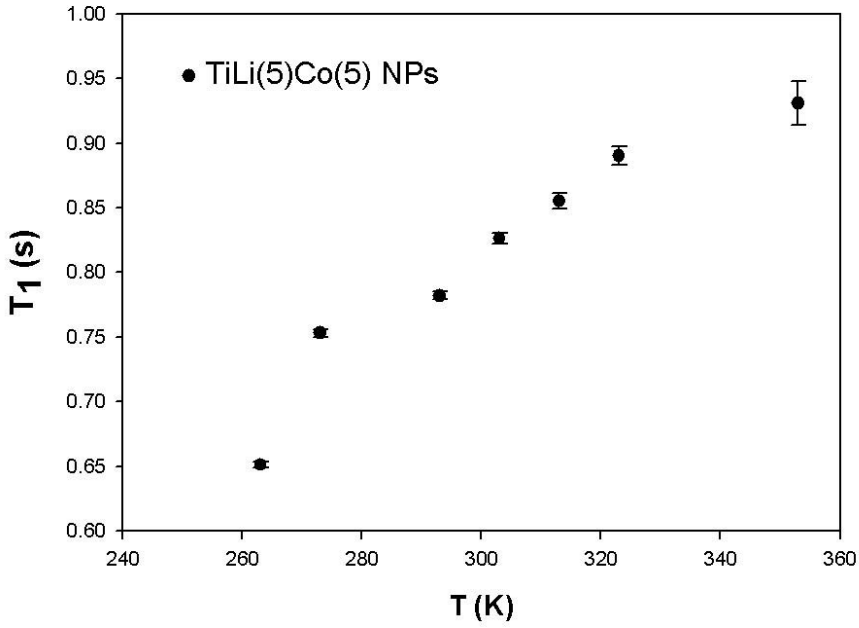

Figs. 54: Longitudinal relaxation decay as function of temperature measured in a) TiLi(5) NPs, b) TiLiNO_3-acid intermediate NPs and c) TiLi(5)Co(5)NPs.

In table 7, transverse relaxation times as function of temperature, measured in TiLiNO_3-acid intermediate are reported.

In figs. 55 a, b the transverse relaxation times measured for the TiLi(5) NPs and TiLi(5)Co(5) NPs samples are reported. In both cases, the behavior of the transverse relaxation time is not linear, and a dynamic simulation is currently being performed in order to better

understand this behavior. The ^{1}H MAS NMR spectra for the same samples are available in the appendix.

Table 7. Transverse relaxation times measured in Li-doped TiO_2 + HNO_3 (intermediate) nanoparticles.

Li-doped TiO2 + HNO3	**M_{01}**	**T_{21}(s)**	**M_{02}**	**T_{22}(s)**	**R^2**
T=273 K	0.27	0.017±0.001	0.73	0.062±0.001	0.9999
T=283 K	0.42	0.017±0.002	0.58	0.056±0.003	0.9998
T=293 K	0.32	0.020±0.006	0.68	0.089±0.008	0.9984
T=303 K	0.25	0.017±0.003	0.75	0.089±0.003	0.9996
T=313 K	0.25	0.019±0.003	0.75	0.086±0.004	0.9997
T=323 K	0.17	0.016±0.003	0.83	0.083±0.002	0.9997
T=333 K	0.15	0.022±0.006	0.85	0.073±0.002	0.9986
T=343 K	0.36	0.024±0.005	0.64	0.071±0.006	0.9997
T=353 K	0.27	0.030±0.009	0.73	0.072±0.006	0.9998

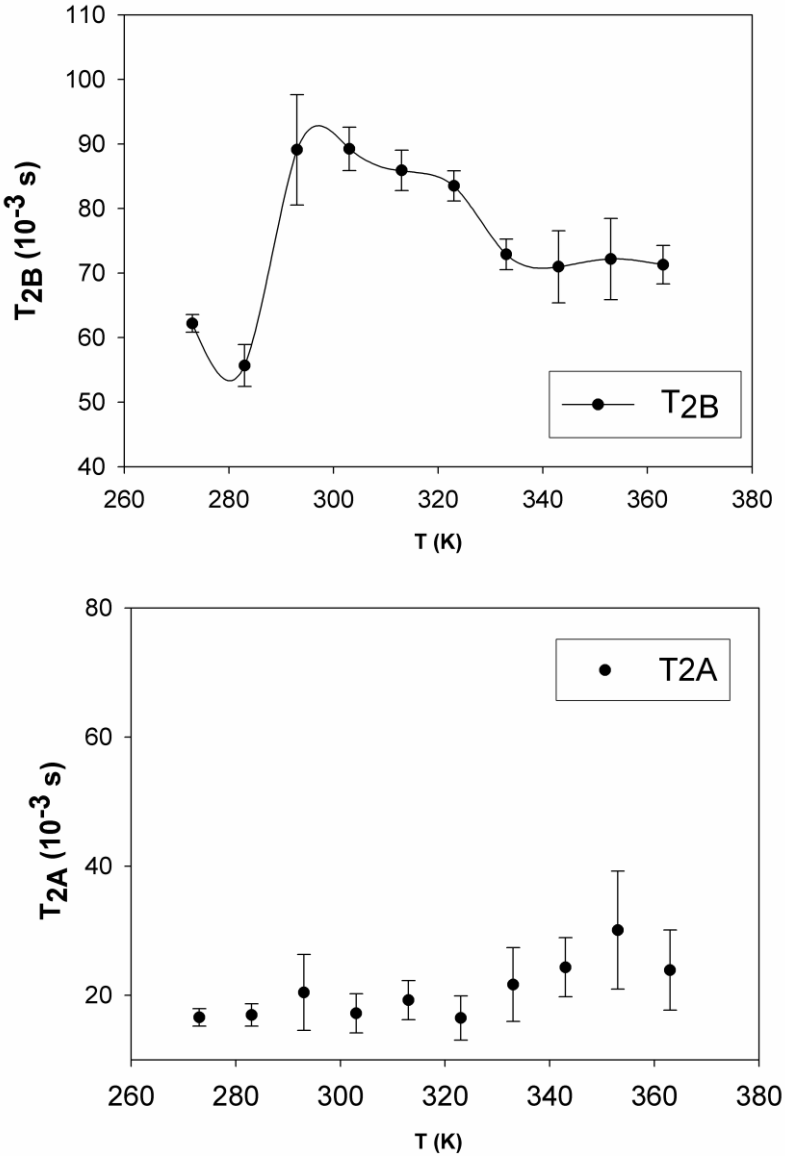

Figs. 55 a, b: Transverse relaxation times measured in TiLi(5)Co(5) NPs (top) and TiLi(5) NPs (bottom).

UV-VIS spectroscopy

UV-VIS spectroscopy was used to characterize the synthesized nanoparticles in order to check the absorption in the visible region. Fig. 56 shows the comparison between the absorption spectra of the commercial product Degussa P25 and the samples that we synthetized and doped with Li or Li and Co ions. As it can be seen in the graph, the spectrum of the Degussa P25 sample exhibits a maximum peak of absorption at around 309 nm, and then decreases rapidly until it reaches 400 nm. This means that its activity is conducted mainly in the region of the near UV spectrum.

The two doped TiO_2 samples that we synthesized show different levels of absorption. In the case of the sample doped with Li, a maximum absorption peak can be observed around 379 nm, shifted by about 70nm with respect to Degussa P25. This sample also has absorption in the visible up to above 500 nm, which means that its activity also takes place in the yellow-green region of the light spectrum.

The sample that was doped with Li and Co shows a maximum absorption around 353 nm, with a clear tail in the visible range up to about 730 nm. This range indicates that doping with Co makes it

possible to obtain extremely noticeable absorption in the range of yellow-green light spectrum, with a tail to red.

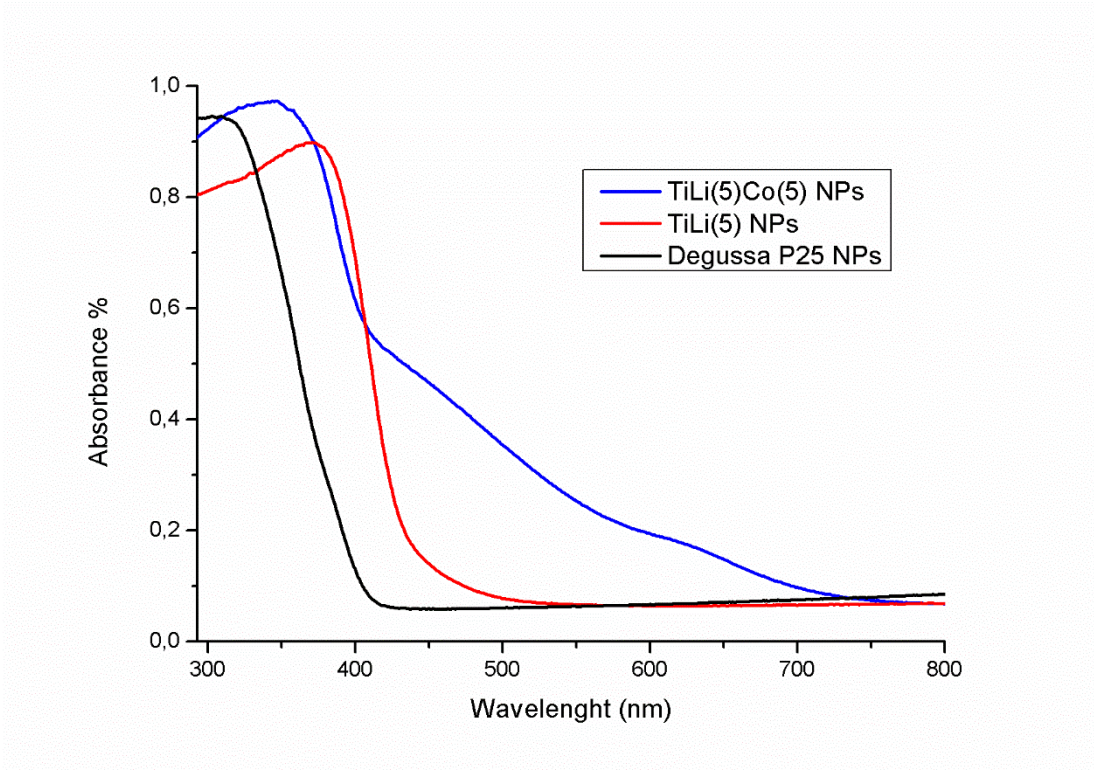

Fig. 56: Comparison of the absorption spectra of Degussa P25 NPs (black), of the TiLi(5) NPs (red) and the TiLi(5)Co(5) NPs (blue).

Fig. 57 shows the comparison between the absorption spectra of the commercial product Degussa P25 and the samples.

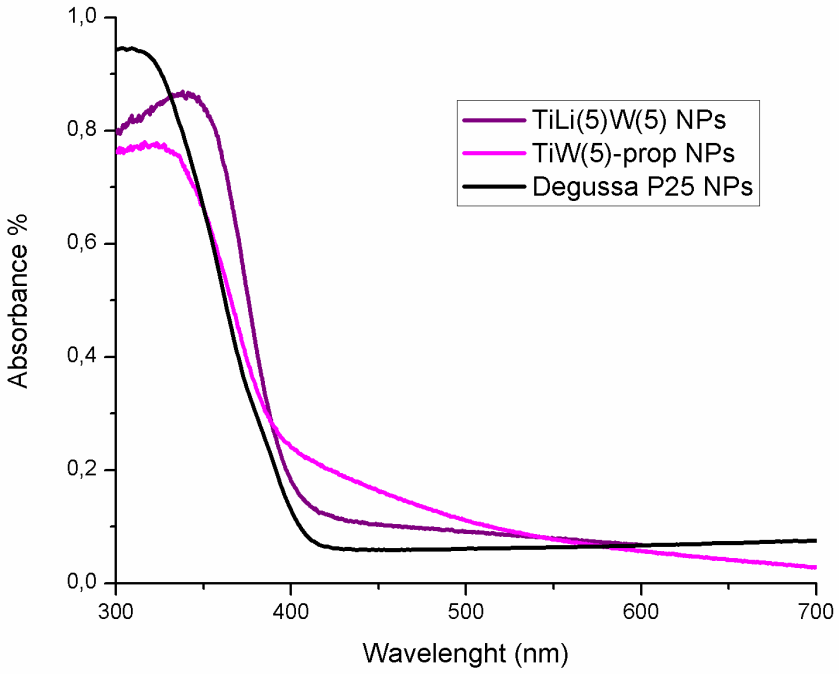

Fig. 57: Comparison of the absorption spectra of Degussa P25 NPs (black), of the TiLi(5)W(5) NPs (violet) and the TiW(5)-prop NPs (pink).

In the case of the sample doped with W in aqueous solution, a maximum absorption can be observed around 375 nm, shifted by about 65 nm respect to Degussa P25. The sample also has absorption in the visible up to above 400 and 500 nm, which means that its activity also takes place in the blue-green region of the spectrum.

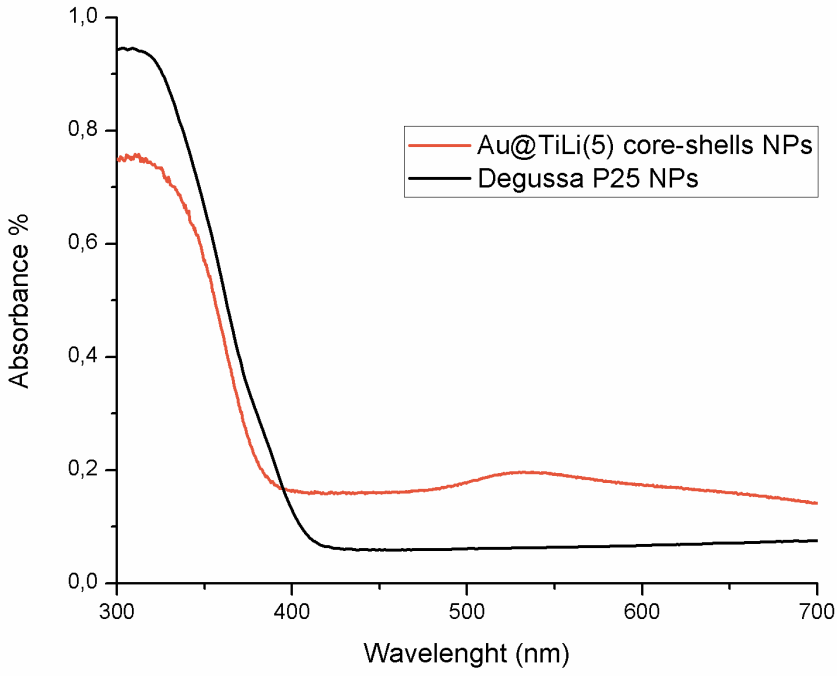

Fig. 58: Comparison of the absorption spectra of Degussa P25 NPs (black) and the Au@TiLi(5) core-shells NPs (orange).

Fig. 58. shows the comparison between the absorption spectra of Degussa P25 and the Au@TiLi(5) core shells. The maximum absorption of both samples is around 309 nm, but the Au@TiLi(5) sample shows an absorption peak around 530 nm. This means that its activity is very similar to the standard in the UV region, but it also absorb in the green-yellow region.

Fig. 59 shows the comparison between the Degussa P25 and the TiLi(5)-xerogel. The xerogel spectra shows a maximum absorption around 346 nm with a shift of 33 nm compared to P25 and a little peak around 400 nm, which represent the minimum for P25.

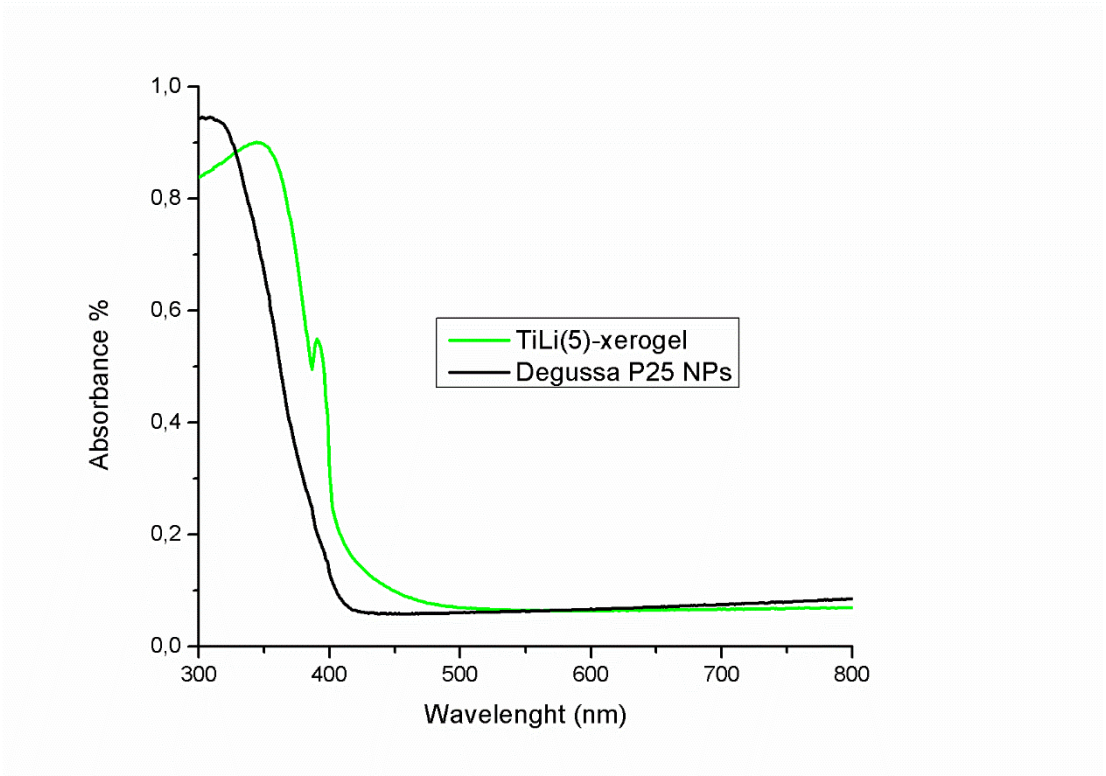

Fig. 59: Comparison of the absorption spectra of Degussa P25 (black) and the TiLi(5)-xerogel (green).

In order to obtain the energy gap value for each sample we applied the Kubelka-Munk function (66) [136]:

$$\alpha h\nu = A(h\nu - E_g)^{1/2} \quad (66)$$

Table 8. Energy Gap (Eg) calculation, best results in grey

Samples	**Eg (eV)**
TiO_2 (Degussa P25)	3.24
TiLiCl(5)	3.19
TiLi(1)	3.22
TiLi(3)	3.20
TiLi(5)	3.18
TiLi(5)Co(1)	3.22
TiLi(5)Co(3)	3.14
TiLi(5)Co(5)	3.05
TiLi(5)Ce(1)	3.21
TiLi(5)Ce(3)	3.18
TiLi(5)Ce(5)	3.13
TiLi(5)W(3)	3.19
TiLi(5)W(5)	3.17
TiLi(5)W(7)	3.14
TiCo(5)-prop	3.09
TiW(5)-prop	3.14
TiLi(5)-nanosheets	3.19
TiLi(5)Co(5)-nanosheets	3.08
TiLi(5)Ce(5)-nanosheets	3.14
TiLi(5)-xerogel	3.20
TiLi(5)Co(5)-xerogel	3.10
TiLi(5)Ce(5)-xerogel	3.15
TiLi(5)Co(5)-aerogel	3.11
Au@TiLi(5)	3.04

Contact angles and wettability

The mechanism for the development of superhydrophilicity of TiO_2 by UV irradiation is believed to involve the formation of either oxygen defects [137] [138] or dangling bonds [139]. Some researchers have been able to synthetize a TiO_2 surface with a modified shape plane, which has a large number of oxygen defects or dangling bonds [140]. Theoretically, this kind of TiO_2 should show superhydrophilic properties without the need for any UV irradiation.

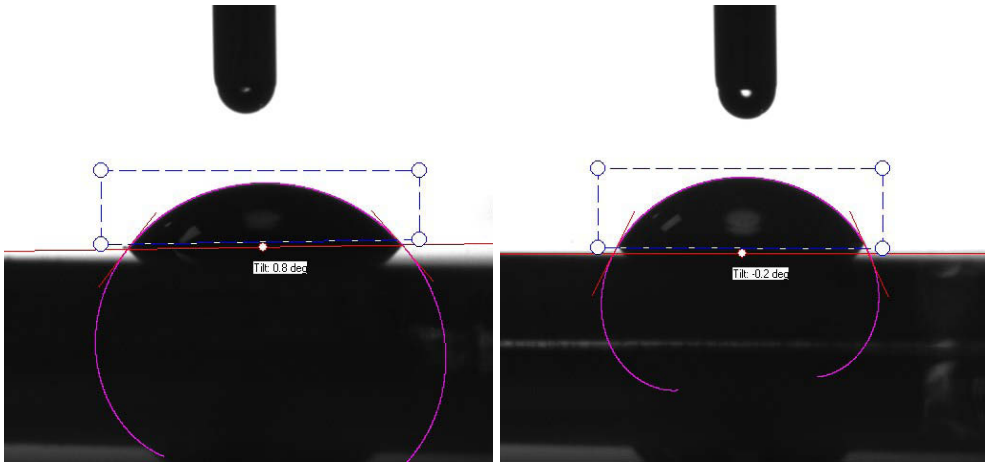

Fig. 60: Measurement of the contact angle of water (a) and hexadecane (b) on a glass surface coated with P25 NPs.

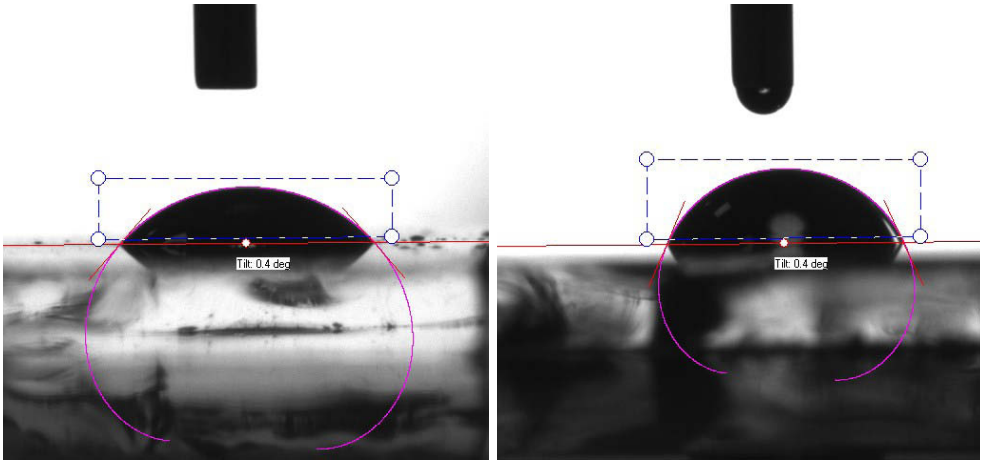

Fig. 61: Measurement of the contact angle of water (a) and hexadecane (b) on a glass surface with ND-TiO_2.

Figs. 60 and 61 show the contact angle of a drop of water (a) and hexadecane (b) on a P25 and ND-TiO_2 coated glass surface. The wettability seems to be normal and the contact angles are between 48° and 56°.

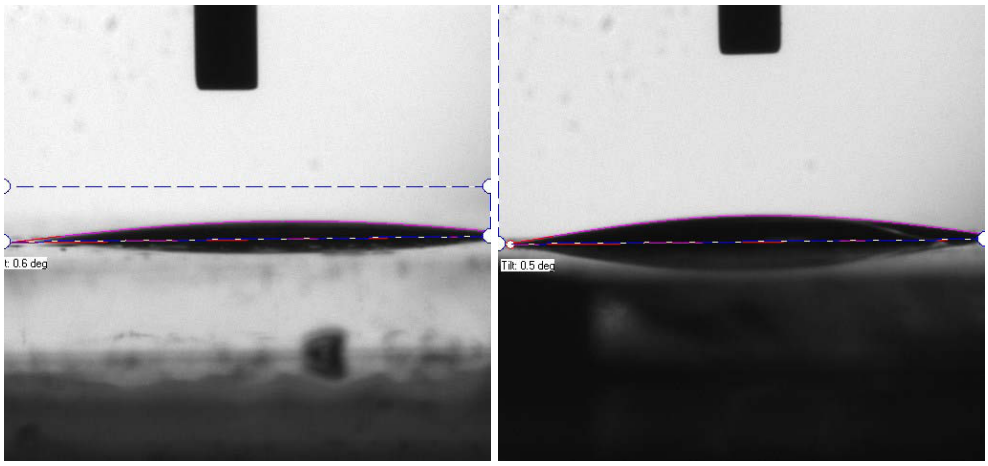

Fig. 62: Measurement of the contact angle of water (a) and hexadecane (b) on a glass surface with TiLi(5).

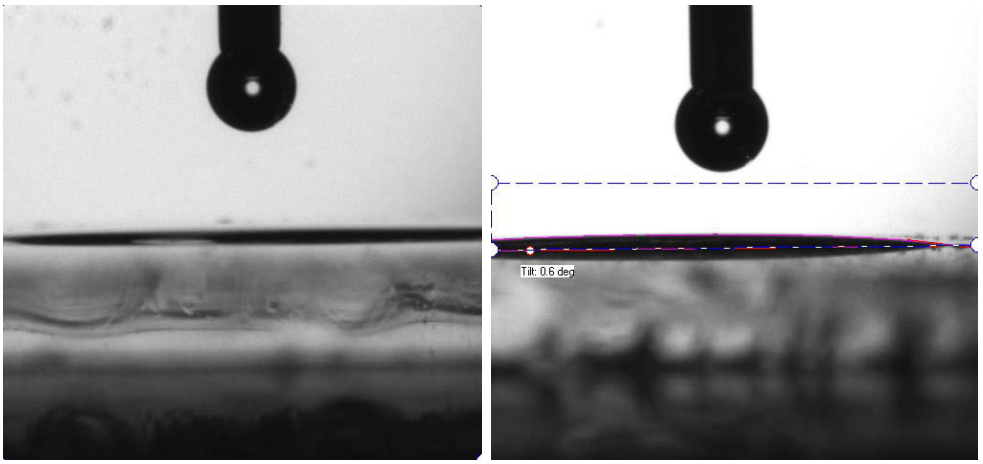

Fig. 63: Measurement of the contact angle of water (a) and hexadecane (b) a glass surface with TiLi(5)Co(5).

Figs. 62 and 63 show the superhydrophilicity and the superoleophilicity of the glass surface coated respectively with TiLi(5) and TiLi(5)Co(5) NPs, using water (a) and hexadecane (b).

These materials show an amphiphilic behavior and antifogging properties (fig. 69).

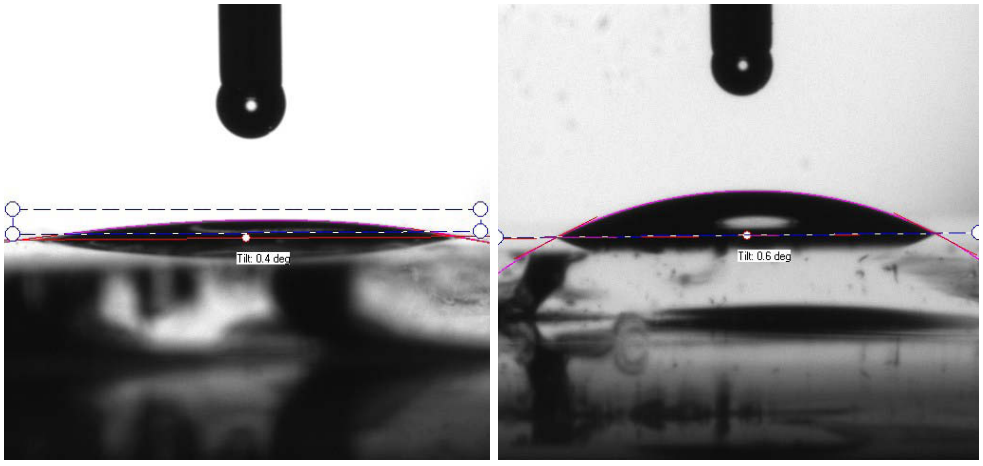

Fig. 64: Measurement of the contact angle of water (a) and hexadecane (b) a glass surface with TiLi(5)Ce(5).

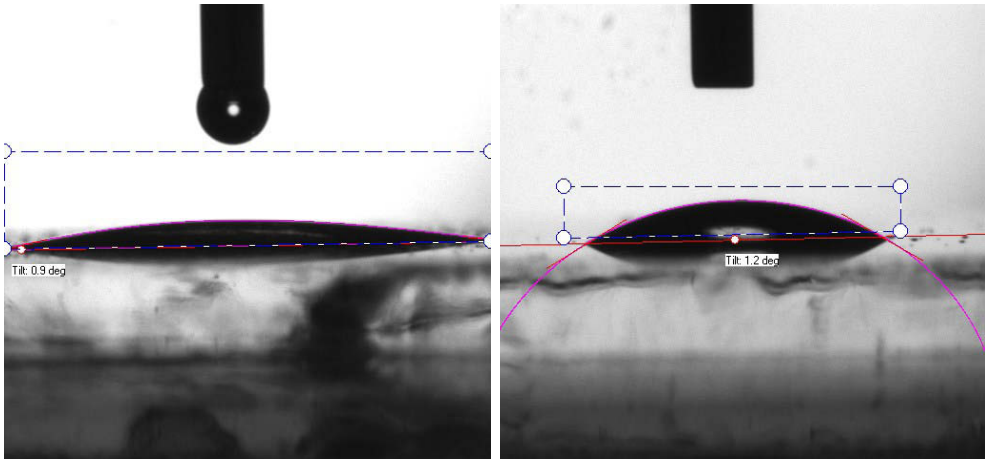

Fig. 65: Measurement of the contact angle of water (a) and hexadecane (b) a glass surface with TiLi(5)W(7).

Figs. 64 and 65 show the superhydrophilicity and the superoleophilicity of the glass surface coated respectively with

TiLi(5)Co(5) and TiLi(5)W(7) NPs, using water (a) and hexadecane (b). These materials show an amphiphilic behavior.

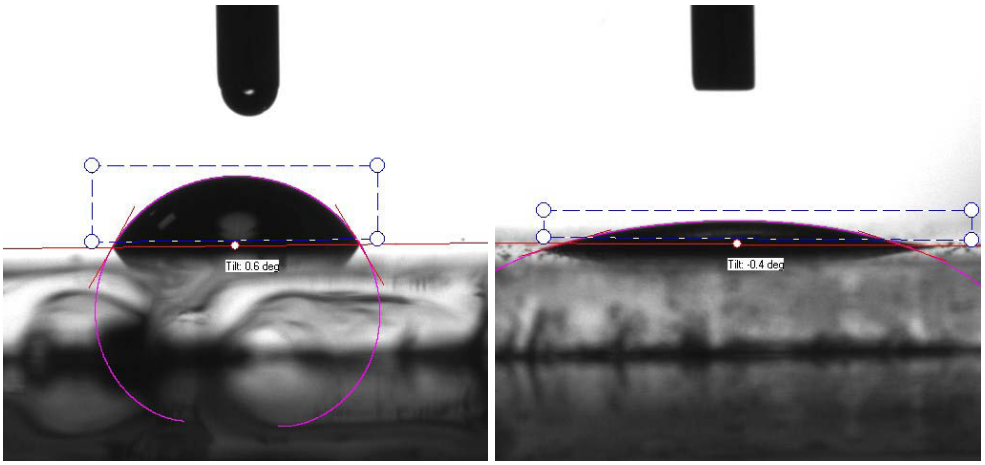

Fig. 66: Measurement of the contact angle of water (a) and hexadecane (b) on a glass surface with TiCo(5)prop.

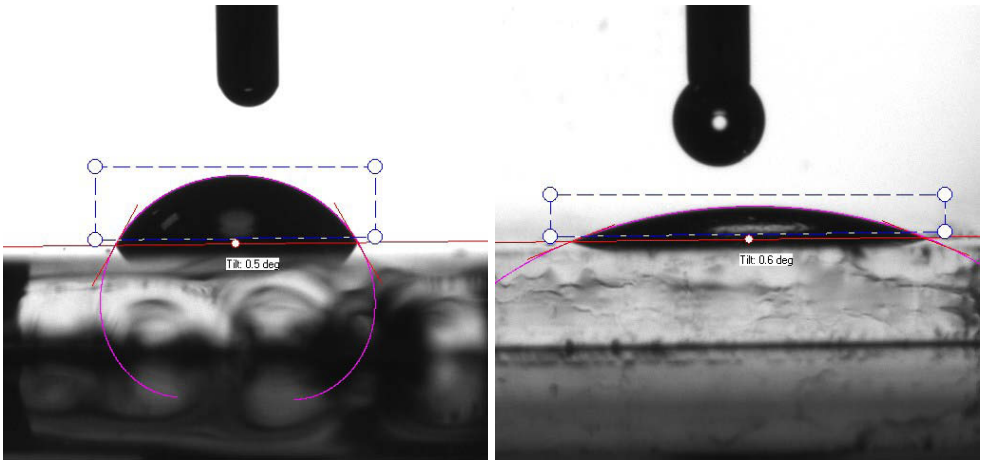

Fig. 67: Measurement of the contact angle of water (a) and hexadecane (b) a glass surface with TiW(5)prop.

Figs. 66 and 67 show the normal wettability with water (a) and superoleophilicity with hexadecane (b) of the glass surface coated with TiCo(5)-prop and TiW(5)-prop.

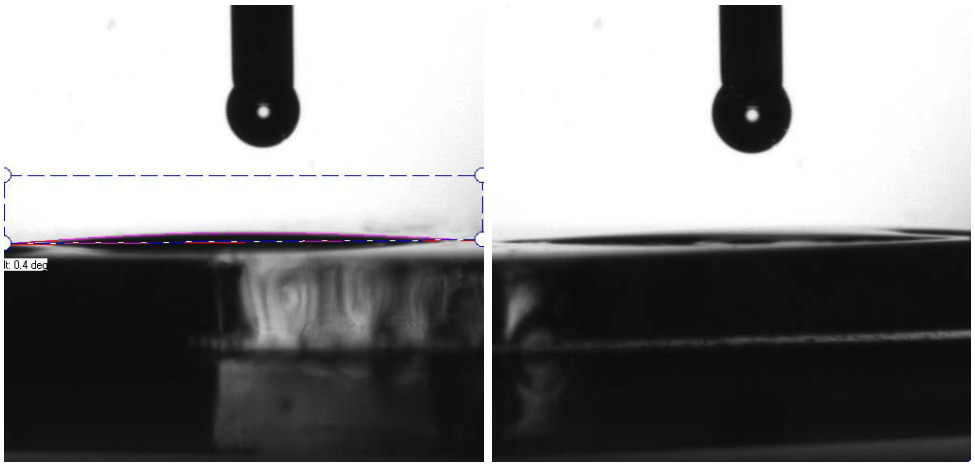

Fig. 68: Measurement of the contact angle of water (a) and hexadecane (b) a glass surface with Au@TiLi(5)

The glass surface coated with the Au@TiLi(5) nanoshells (fig. 68) shows superhydrophilicity and superoleophilicity using water (a) and hexadecane (b). The material also show amphiphilic behavior in this case.

Table 9. Contact angles between functionalized glass and water drop

Samples	**Contact Angles with water**	**Contact Angles with hexadecane**
Not treated glass	48.63°	56.11°
P25	49.69°	65.60°
ND-TiO_2	48.62°	66.90°
TiLi(5)	6.35°	8.54°
TiLi(5)Co(5)	< 1°	6.79°
TiLi(5)Ce(5)	9.11°	26.95°
TiLi(5)W(7)	9.70°	29.90°
TiCo(5)-prop	59.56°	17.30°
TiW(5)-prop	60.17°	21.91°
Au@TiLi(5)	3.05	< 1°

Fig. 69: Comparison of antifogging properties between uncoated (left) and TiLi(5)Co(5) NPs coated glass slide in steamed environment

Degradation of Rhodamine B in aqueous solution

The photocatalytic activities of doped TiO_2 NPs and nanosheets were evaluated by degrading a dye (Rhodamine B), in aqueous solution (10 mg/l), using UVb light (254 nm) and visible light (420 nm of maximum peak and a bandpass filter on 400 nm) irradiation. For photocatalytic process, 10 mg of each material were put into a 200 ml solution in a cylindrical glass reactor.

The solutions were irradiated in the horizontal direction, and the distance between the UV lamp and the solution was kept within 5 cm. Then, the solution had to be kept in a dark room and well stirred with the magnetic stirrer for more than 20 minutes to attain

equilibrium conditions throughout the solution. The concentration of the aqueous-dye suspensions in each sample was measured using UV–Vis spectrophotometer at a wave-length of 553 nm. The photocatalytic efficiency was calculated from the expression (66):

$$\eta = (1 - \frac{C}{C_0}) \quad (66)$$

where C_0 is the concentration of dyes before illumination, and C is the concentration of dyes after a given irradiation time. The aqueous suspensions were measured every 5 min during the process of photodegradation.

Degradation of Rhodamine B under UVb light

The results in fig. 75 show that the length of illumination and the quantity of the photocatalyst have an obvious influence on the degradation of the reactive dye. In general, the effect of the photocatalyst is evident in the results showed in these figures. Figs. 70, 71, 72, 73, and 74 present the degradation profiles of Rhodamine B in presence of the different groups of doped-TiO_2 NPs under UVb light at 254 nm. The TiLi group shows a similar behavior compared to the control group (Degussa P25 and ND-TiO_2). In the

cases of TiLiCe and TiLiW groups, the behavior is similar, but the kinetic is slower in comparison to the control group. The TiLiCo group shows a very slow kinetic compared to the controls, but the Au@TiLi(5) sample degradates most of the RhB in 30 minutes. At the reaction time of 60 min, the RhB degradation efficiencies of most of the samples are comparable with the standard sample. It is possible that the TiLiCo groups are shifted in the absorbance because of the color of the NPs themselves. The whole testing procedure was repeated three times. The standard deviation for the three experiments indicates a confidence level of 4,5% at the time of 60 min.

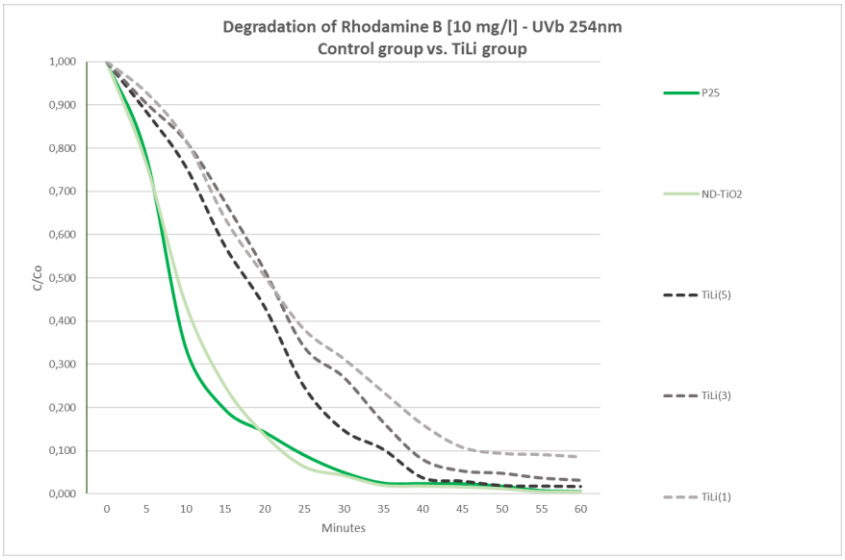

Fig. 70: Degradation of Rh. B under UVb light: comparison between the control group and the Li-doped NPs group.

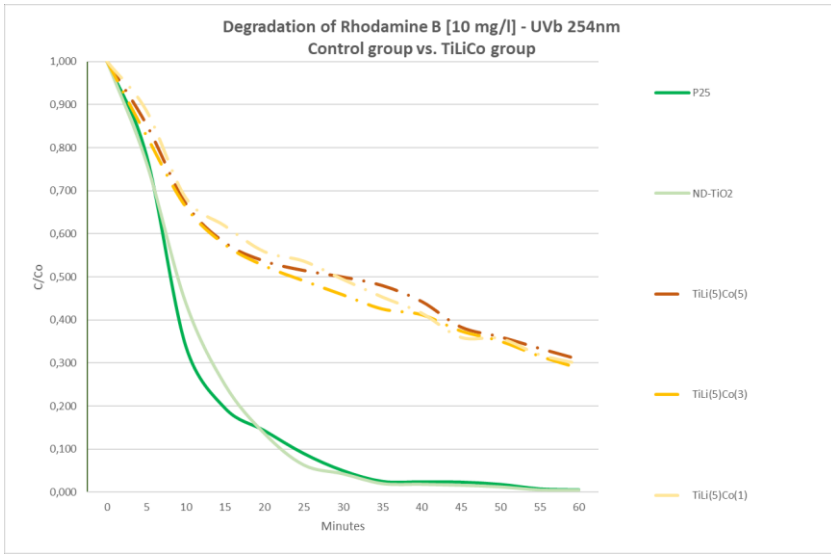

Fig. 71: Degradation of Rh. B under UVb light: comparison between the control group and the Li-Co doped NPs group.

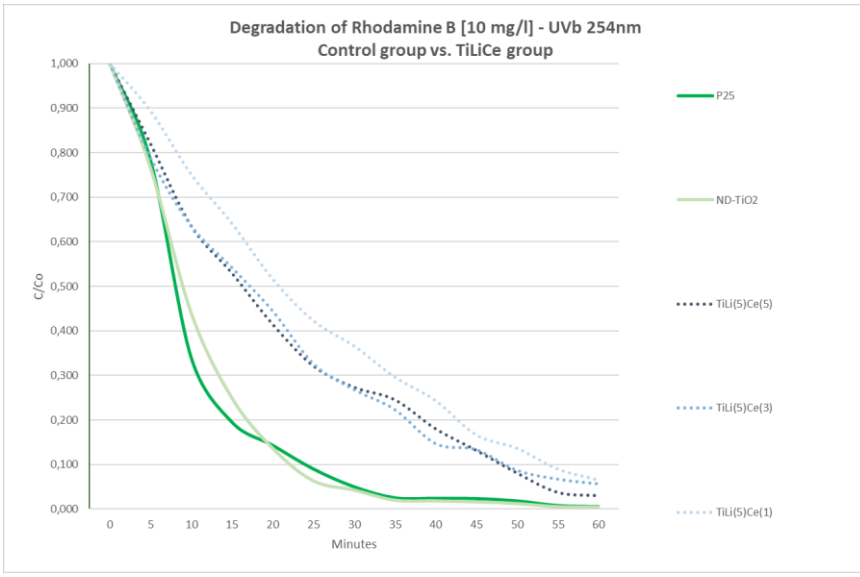

Fig. 72: Degradation of Rh. B under UVb light: comparison between the control group and the Li-Ce doped NPs group.

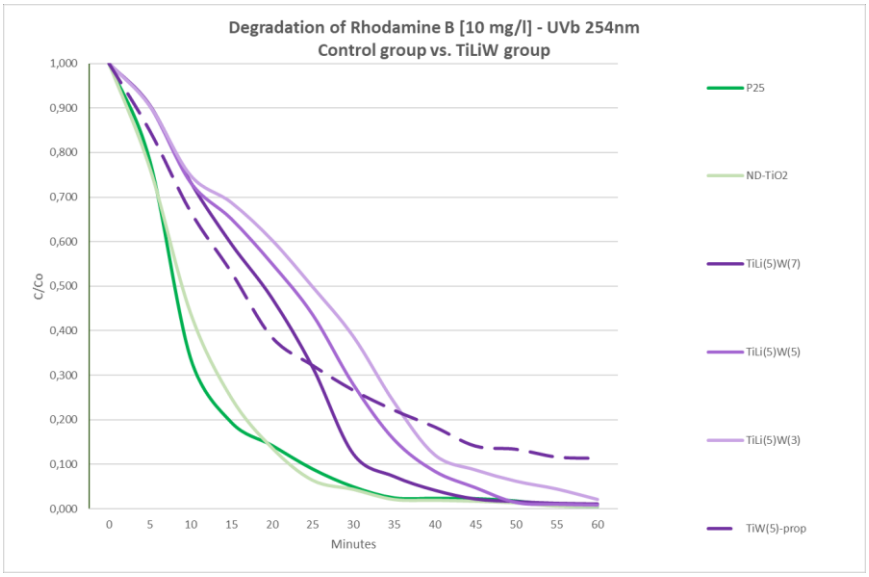

Fig. 73: Degradation of Rh. B under UVb light: comparison between the control group and the Li-W doped NPs group.

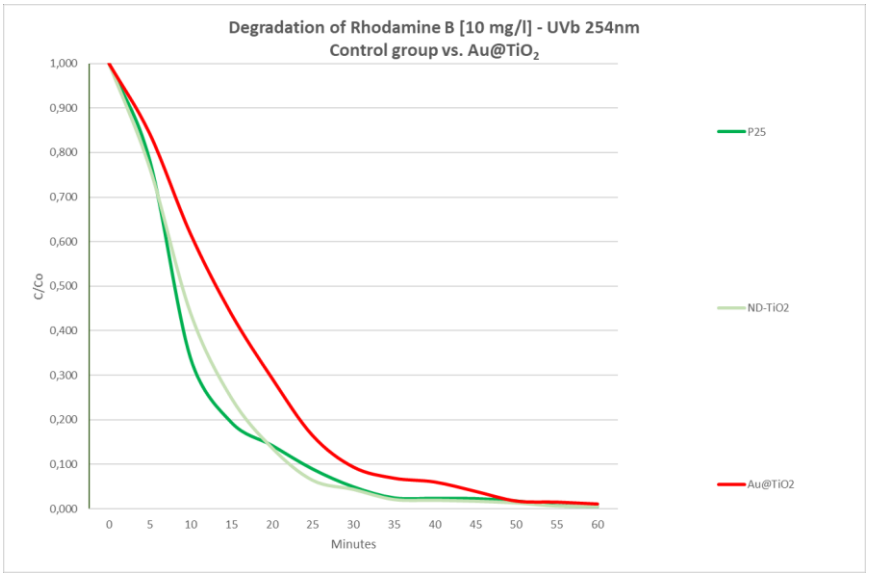

Fig. 74: Degradation of Rh. B under UVb light: comparison between the control group and the Au@TiLi(5) core shell group.

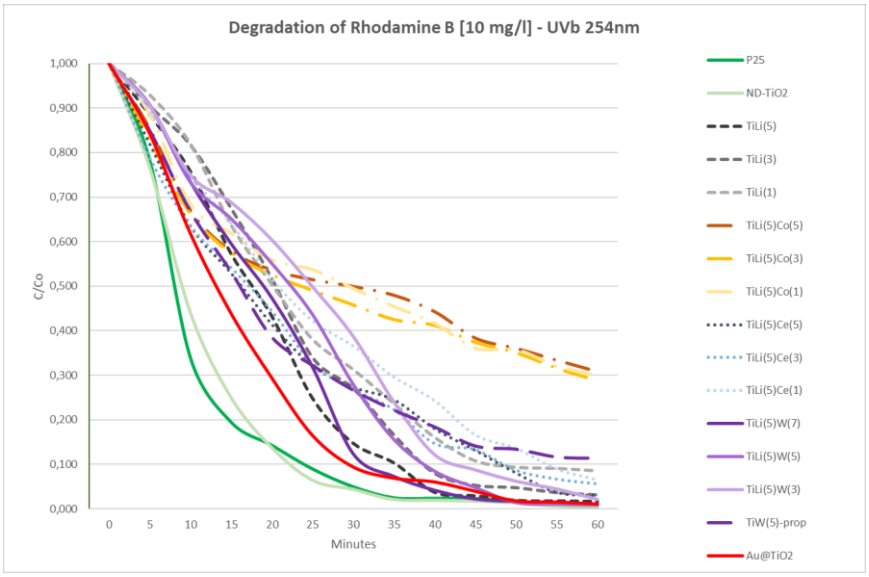

Fig. 75: Degradation of Rh. B under UVb light and comparison between all groups.

Degradation of Rhodamine B under visible light

Figs. 76, 77, 78, 79 and 80 show the degradation profiles of Rhodamine B in presence of the different doped-TiO_2 NPs groups under visible light at 420 nm of maximum peak and a bandpass filter at 400 nm. In this case, it is possible to see that the standard samples (P25 and ND-TiO_2) do not show any photocatalytic activity after 60 minutes of reaction. The photocatalytic activity of TiLiCo NPs group is much greater than the standard TiO_2 group, in particular for the sample TiLi(5)Co(5), which shows the best activity in comparison to

all other samples. It is important to notice that all the samples with 1% of dopants present a similar behavior of the standard group. All the samples with 5% of dopants show the best photocatalytic activity in each group. The best kinetic is reported for the samples Au@TiLi(5), TiW-prop, and TiLi(5)Co(5). The whole testing procedure was repeated three times. The standard deviation for all three tests indicates a confidence of 4,3% at the time of 60 min.

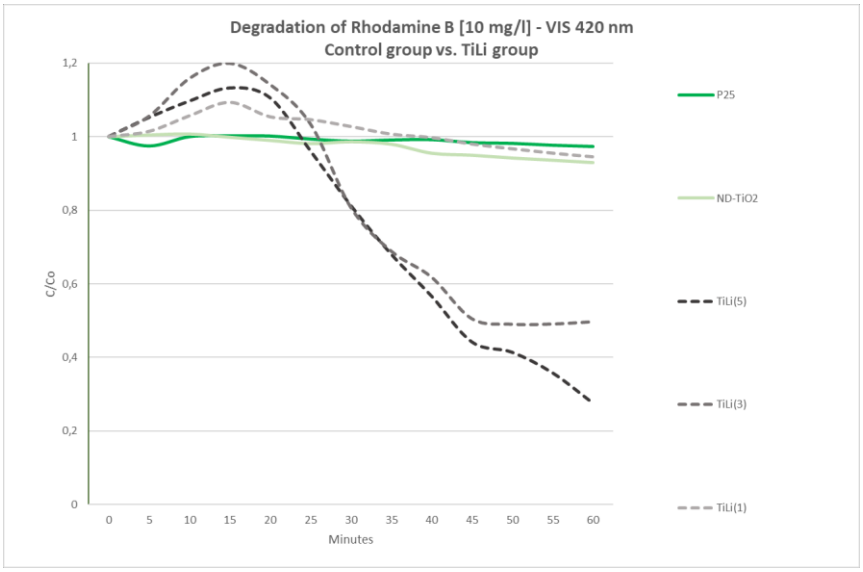

Fig. 76: Degradation of Rh. B under VIS light: comparison between the control group and the Li-doped NPs group.

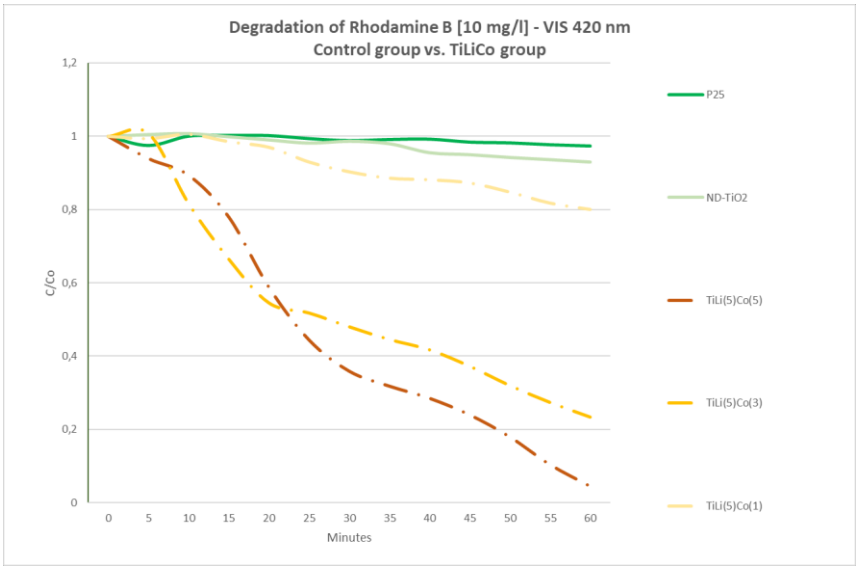

Fig. 77: Degradation of Rh. B under VIS light: comparison between the control group and the Li-Co doped NPs group.

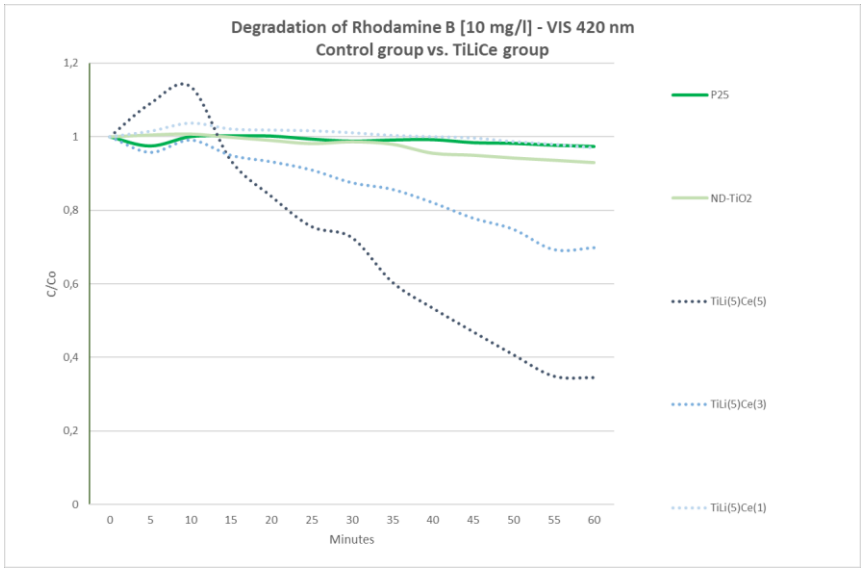

Fig. 78: Degradation of Rh. B under VIS light: comparison between the control group and the Li-Ce doped NPs group.

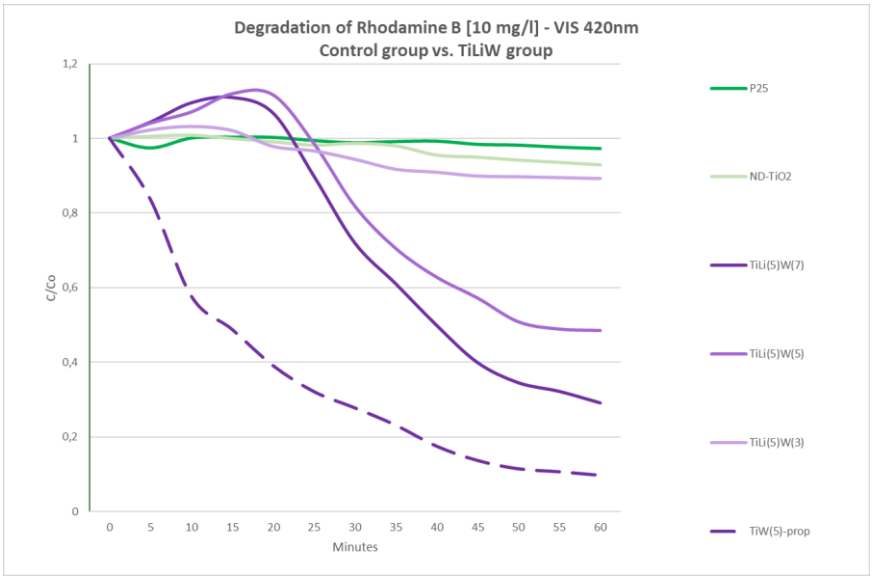

Fig. 79: Degradation of Rh. B under VIS light: comparison between the control group and the Li-W doped NPs group.

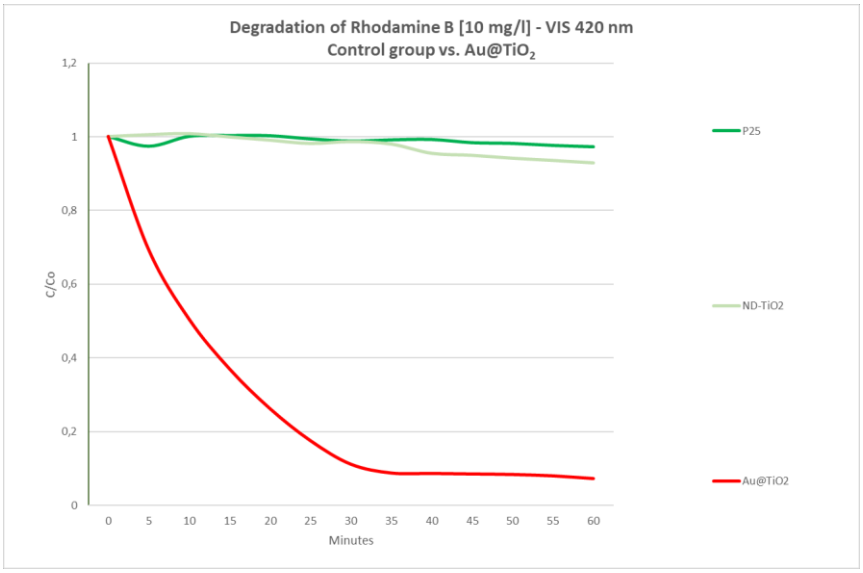

Fig. 80: Degradation of Rh. B under VIS light: comparison between the control group and the Au@TiLi(5) core shell group.

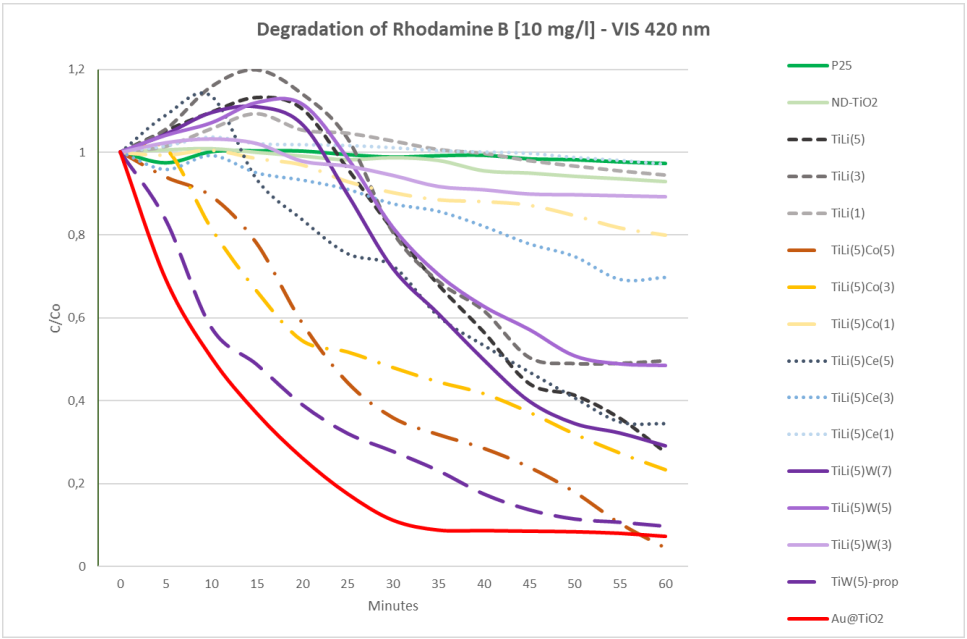

Fig. 81: Degradation of Rh. B under VIS light and comparison between all groups.

Degradation of formaldehyde under visible light

Volatile organic compounds (VOCs) are generally considered as key pollutants in the atmosphere, and play a crucial role in the formation and aging of fine particulate matter (PM). They can also react with oxidizing gases (e.g. ozone) and radicals (e.g. OH radicals and HO_2 radicals), contributing to the growth of fine PM. Heterogeneous reactions on PM can involves VOCs and other substances. These processes increase the dimensions of the particles, and change their chemical composition as well as their physical properties [141].

To simulate the impact of our catalyzer in the atmosphere, we chose to experiment it on formaldehyde (HCHO), since this compound is the most abundant carbonyl-containing VOC in the atmosphere [142] [143]. Atmospheric HCHO comes either from the oxidation of organic compounds or is directly emitted by industrial sources [15]. Its reactions with OH radicals, photolysis, and dry or wet deposition are well known, as well its removal pathways. However, Liu et al. found those sinks insufficient to improve the air quality during the large pollution controls enforced in Beijing for two months in order to reduce the emission of HCHO before the 2008 Olympic Games [143]. The heterogeneous processes between HCHO and other atmospheric aerosol compounds like sulfate aerosols [144] [145], mineral dust aerosols [146] [147] [148] [149], and organic aerosols [150] have been widely studied recently, and their contribution to the degradation of HCHO was evidenced [148]. Several of these studies focused on the oxides dust in aerosols, such as SiO_2, TiO_2, Al_2O_3, and Fe_2O_3.In particular, the adsorptions of HCHO by α- Al_2O_3, α- Fe_2O_3, and TiO_2 were found to be irreversible [146] [147], permanently affecting their hygroscopicity and their optical properties [148]. The principal meteorological factors such as

temperature (T), relative humidity (RH), and light radiation also have an impact on the heterogeneous reactions of VOCs [151] [152].

However, in this study, we realized a model to simulate a specific percentage of formaldehyde in a chamber. A realistic model of the atmosphere is multicomponent and more complex, and our laboratory experiments represent only a foundation to test the photocatalytic systems in a real environment.

The kinetic of the photocatalytic effect of the NPs we made (under visible light at 420 nm of maximum peak and a bandpass filter on 400 nm) with HCHO (4 ppm) inside an environmental chamber (4000 cm^3) was simulated for 120 minutes on each sample. We used the acetylacetone method [153] and the absorption of the reaction product 2,6-dimethyl-3,5-diacetyl-1,4-dihydropyridin in water at 413 nm (molar absorptivity $6.639 \cdot 10^3$ $L \cdot mol^{-1} \cdot cm^{-1}$) [154]. The decay rates of HCHO and the primary degradation products (CO_2) were measured using a GC-MS, and then compared with the Degussa P25 and the NP-TiO_2. All the tests made with the acetylacetone method were repeated three times, providing a standard deviation that indicates a confidence level of 4,8% at the time of 60 min. The GC-

MS test for the detection of CO_2 was carried out just once to verify that the conversion of HCHO into CO_2 actually took place.

The TiLi group showed a low conversion rate of HCHO in CO_2; in particular, the sample TiLi(1) shows the same behavior as the control group. The best result is achieved by the TiLi(5)Co(5) sample, which reaches the maximum conversion rate in around 100 minutes.

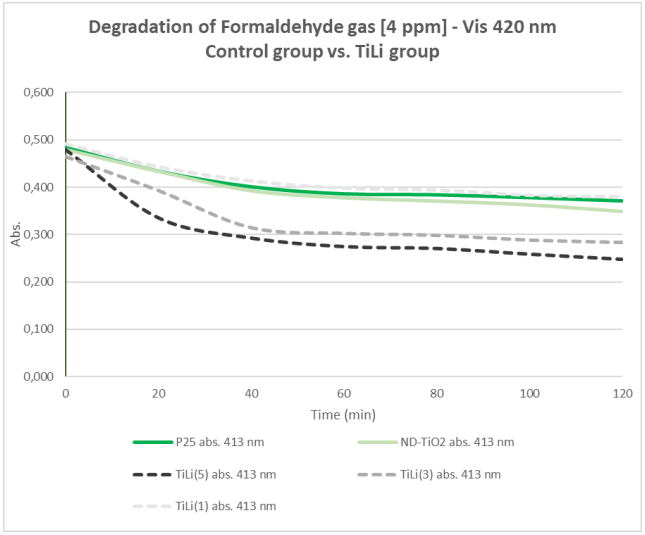

Fig. 82: Degradation of HCHO under visible light and comparison between the control group and the TiLi group.

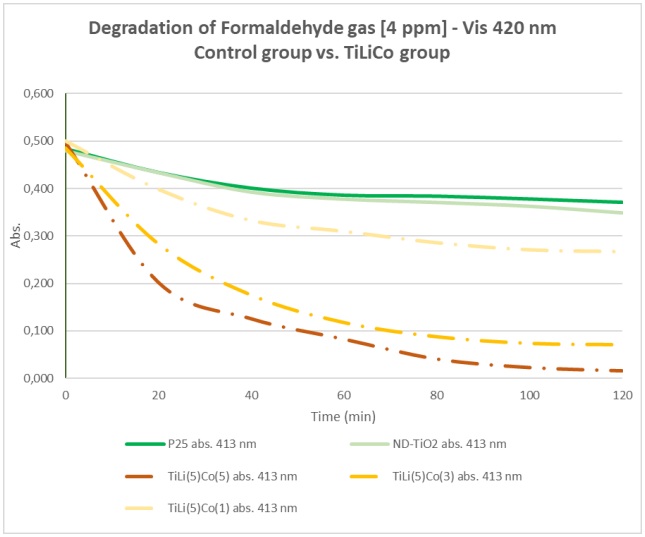

Fig. 83: Degradation of HCHO under visible light and comparison between the control group and the TiLiCo group.

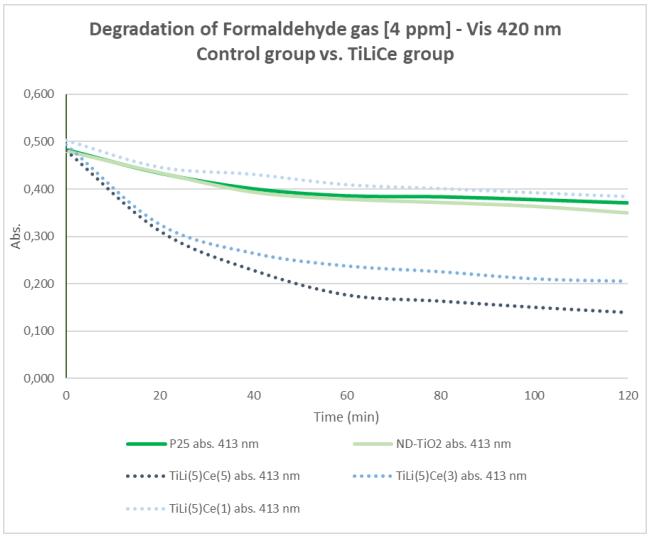

Fig. 84: Degradation of HCHO under visible light and comparison between the control group and the TiLiCe group.

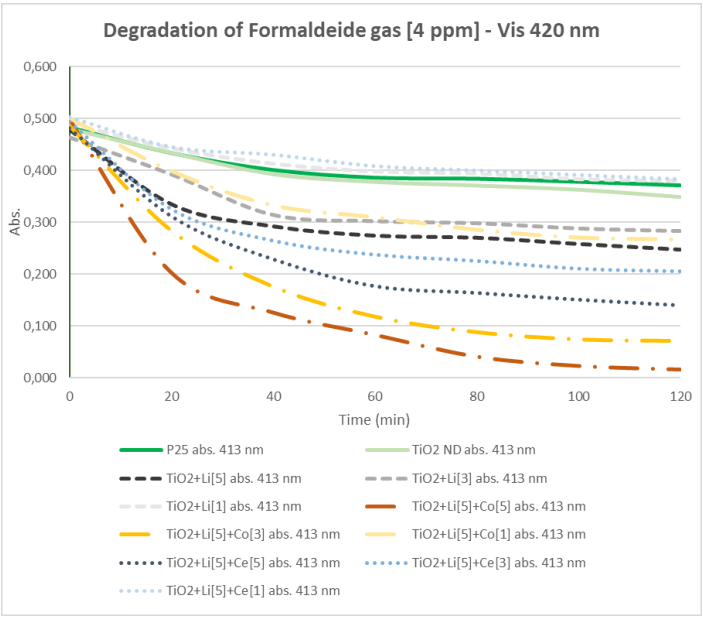

Fig. 85: Degradation of HCHO under visible light and comparison between all groups.

In addition, the primary product of HCHO degradation (CO_2) was investigated. In fig. 86, the Gas Chromatography standard curve for CO_2 between 0 and 43 ppm concentration is depicted. The fit is linear (R^2=0,9997), which allows us to use the GC data without any modification.

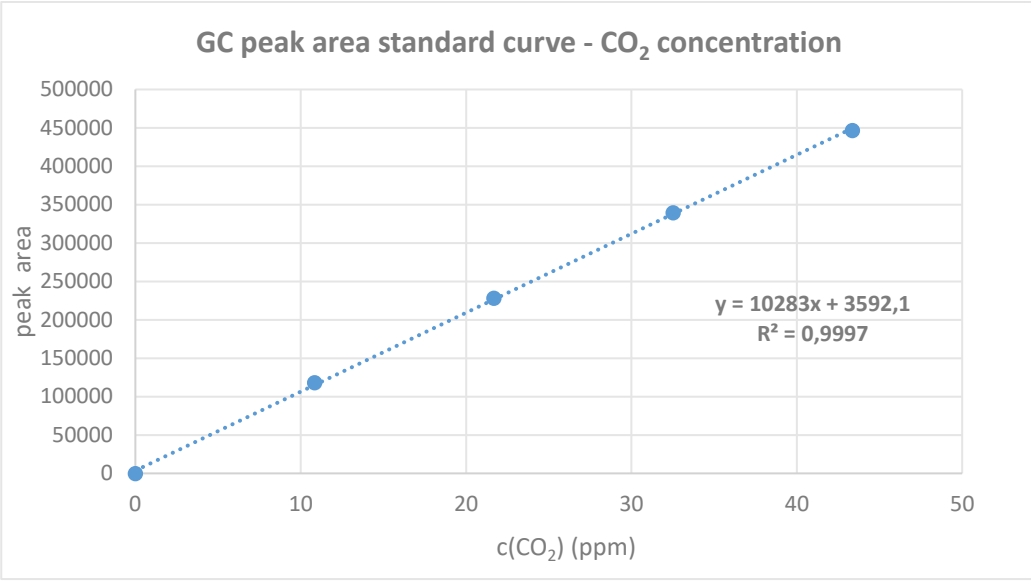

Fig. 86: Gas chromatography standard curve for CO_2.

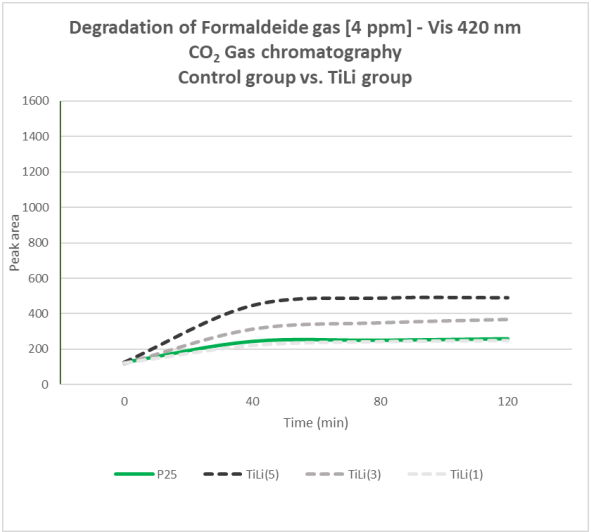

Fig. 87: CO_2 production during photocatalytic reaction for the Li doped NPs and P25.

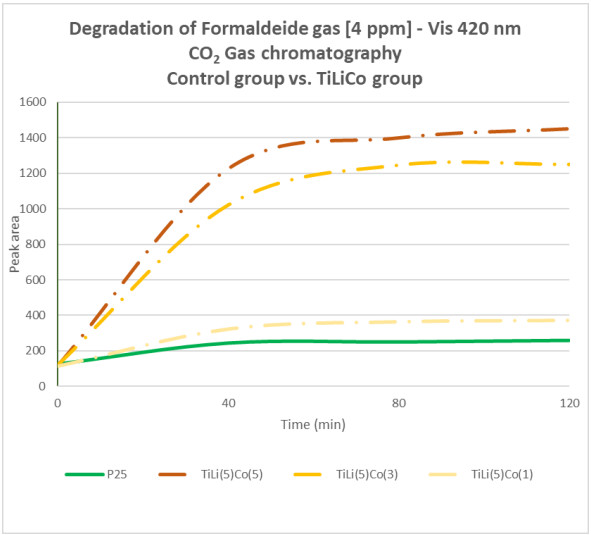

Fig. 88: CO_2 production during photocatalytic reaction for the Li-Co doped NPs and P25.

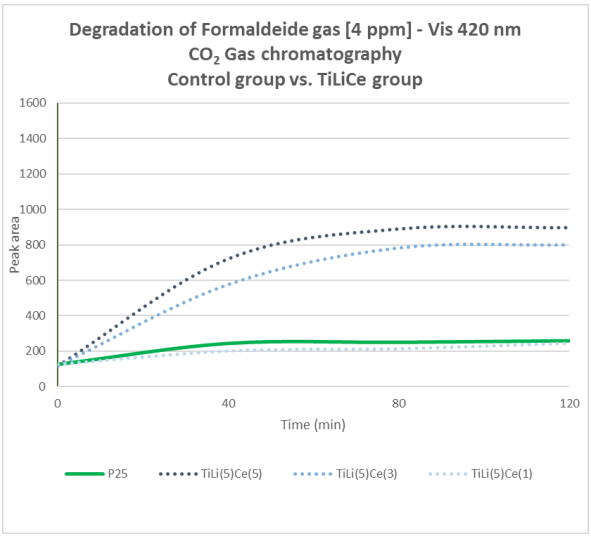

Fig. 89: CO_2 production during photocatalytic reaction for the Li-Ce doped NPs and P25.

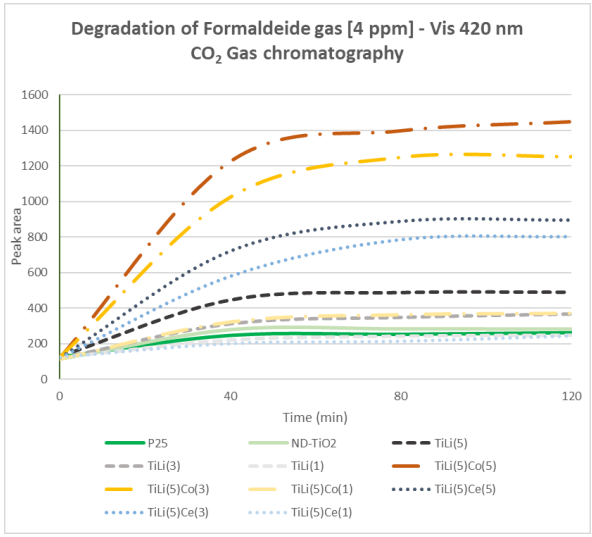

Fig. 90: CO_2 production during photocatalytic reaction for all the groups.

Cytotoxicity of doped NPs on *E. coli* and Human Lung Cells

In-vitro tests were carried out in order to determine the toxicity and the risk related to the use of TiO_2 NPs and doped TiO_2 NPs in public space (indoor and outdoor) with and without photocatalytic activation. Nanoparticles smaller than 100 nm have a high deposition efficiency through the respiratory tract [155] [156]; however, their toxicity is not only related to their size [157] [158] [159] [160].

In this study, cytotoxicity was evaluated through the cellular survival rate using a WST-1 assay, which is a colorimetric method based on the conversion of the tetrazolium salt WST-1 and of the sodium salt

of 4-[3-(4iodophenyl)-2-(4-nitrophenyl)-2H-5-tetrazolio]-1,3-benzene disulfonate [161] (Roche) into a soluble colored formazan by a cellular reduction system. For this test, we used human Caucasian fibroblast-like lung cells (WI-38 cell Line, Sigma-Aldrich) and *Escherichia coli* cells (*E. coli* K12 strain, Sigma-Aldrich) [162] [163].

Intracellular Lactate Dehydrogenase (LDH) was also used as a marker of membrane integrity. LDH leakage assay provides information on membrane integrity because this enzyme is normally present in the cytosol of mammalian cells and released into the extracellular medium through the damaged plasma membrane [164]. Some studies showed that some cytotoxicity assays were not suitable for assessing nanoparticles' toxicity, because of their possible role in the oxidation of NADH to NAD^+ [165] [166] or in the adsorption of LDH molecules on the surface of NPs [167] [168] [169]; however, Han et al. [170] validated the LDH assay for TiO_2 toxicity.

All methods are well reported in the literature [155] [160] [164] [170] [171].

WST-1 assay

For the WST-1 assay, eight groups of tests in triplicate were carried out:

- group zero (G0): WI38-G0 (3 plate) and ECK12-G0 (3 plate) in absence of NPs and irradiation as control;
- group one (G1): WI38-G1 (51 wells) and ECK12-G1 (51 wells) with NPs but in absence of irradiation;
- group two (G2): WI38-G2 (51 wells) and ECK12-G2 (51 wells) with NPs and with the presence of UVb irradiation (290 nm, 4.3 mW cm^{-2});
- group three (G3): WI38-G3 (17 wells) and ECK12-G3 (17 wells) with NPs and with the presence of visible light (420 nm of maximum peak and a bandpass filter of 400 nm, 4.1 $mWcm^{-2}$).

The cells were purchased from Sigma-Aldrich and grown in RPMI1640 medium (Welgene) and Dulbecco's modified eagle's medium (DMEM) under a humidified atmosphere (5% CO_2, 95% air). The media were supplemented with calf serum 100 ml/L, penicillin 100 units/ml and streptomycin 100 mg/L.

10^3 cells/100 µl were seeded in 104 well plates and incubated overnight at 37 °C under a 5% CO_2 atmosphere. After 24 hours, the

medium that had been put in the wells was replaced with a fresh medium containing nanoparticles (~600 µg/ml each), and kept in incubation for 72 h. The pH of the nanoparticles solution had to be adjusted to 5.5-6.5 in order to not damage the normal growth of the cells, and the solution was therefore maintained at 7.2-7.4 by equilibration with CO_2. The effect of the nanoparticles on cell proliferation was determined by a water-soluble tetrazolium assay protocol (WST-1) as described above. To sum it up, 10 µl of WST-1 solution were added to each well, and the plates were further incubated under irradiation (except for groups G0 and G1). After 4 h, the absorbance was measured with a plate reader at 440 nm.

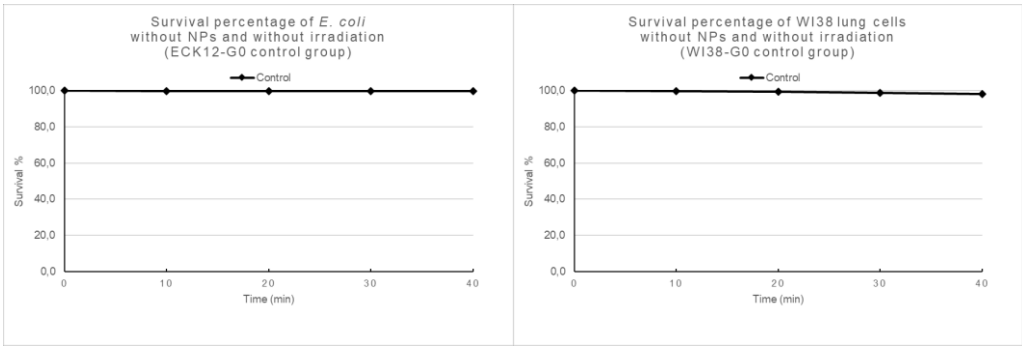

Figs. 91 a, b: comparison between the control groups of E. coli and human lung cells, without NPs and without irradiation (G0).

Figs. 91 a and b show the first control group (G0), which contains the two groups of cells without any NPs and irradiation. Forty minutes after the start of the experiment, no variation of the survival percentage can be observed.

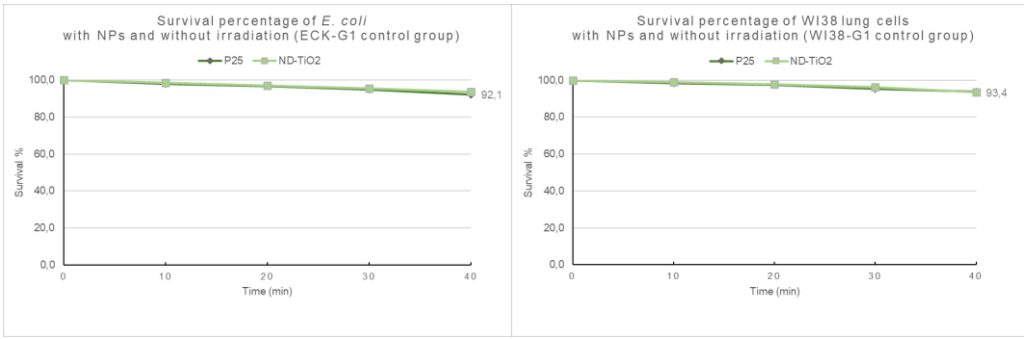

Figs. 92 a, b: comparison between the control groups of E. coli and human lung cells with NPs and without irradiation (G1).

Figs. 92 a and b show the control group G1, for which the cells were treated with our blanks (the Degussa P25 and the ND-TiO_2), but the samples were merely kept in the dark, without any irradiation. We can notice that the mortality level of both types of cell is around 8%.

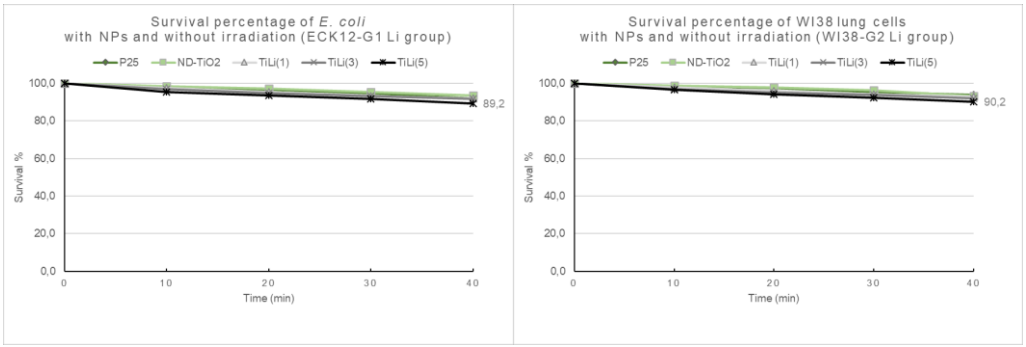

Figs. 93 a, b: comparison between the control groups and TiLi groups of E. coli and human lung cells with NPs and without irradiation (G1).

Figs. 93 a and b show the first comparison between the control groups and the TiLi NPs groups in absence of irradiation. In both cases, the mortality level is around 10% after 40 minutes.

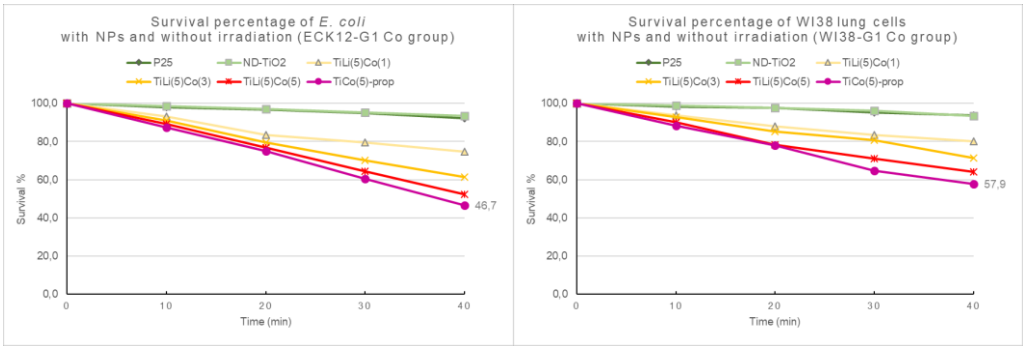

Figs. 94 a, b: comparison between the control groups and TiLiCo groups of E. coli and human lung cells with NPs and without irradiation (G1).

Figs. 94 a and b show the comparison between the control groups and the Co doped NPs groups in absence of irradiation. In both cases, we can observe a linear decrement of the live cells. The *E. coli* cells are more sensitive than human lung cells, and after 40 minutes, the survival percentage is around 46% for the bacteria and around 58% for the lung cells.

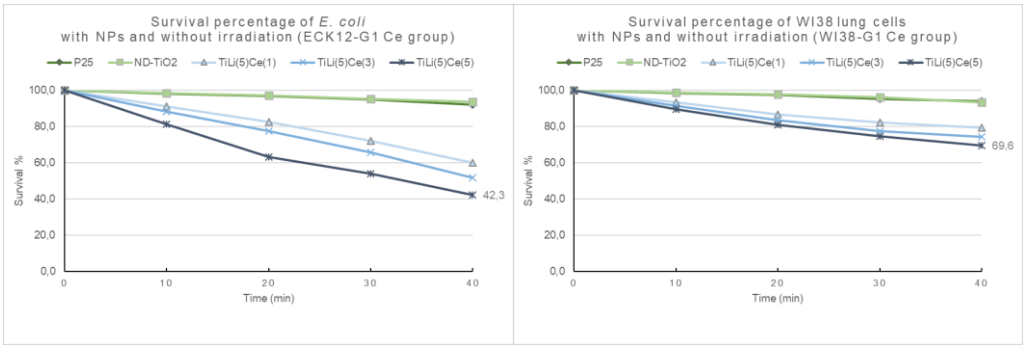

Figs. 95 a, b: comparison between the control groups and TiLiCe groups of E. coli and human lung cells with NPs and without irradiation (G1).

Figs. 95 a and b show the comparison between the control groups and the TiLiCe NPs groups in absence of irradiation. In this case, the *E. coli* cells shown a greater mortality (57,7%) than human lung cells (30,4%) after 40 minutes.

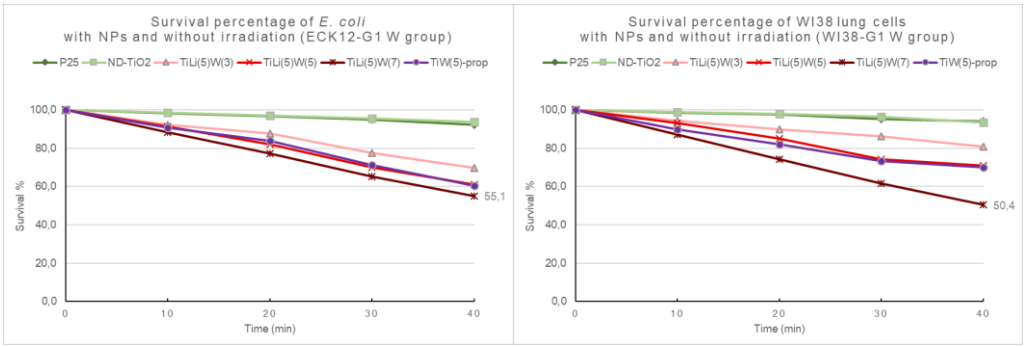

Figs. 96 a, b: comparison between the control groups and TiLiW groups of E. coli and human lung cells with NPs and without irradiation (G1).

Figs. 96 a and b show the comparison between the control groups and the W doped NPs groups in absence of irradiation. In both cases, we can observe a linear decrement of the live cells. After 40 minutes, in the worst cases (the samples with 7% of W) the mortality level is between 45 and 50%. It is important to notice that the mortality increases as the percentage of dopant increases.

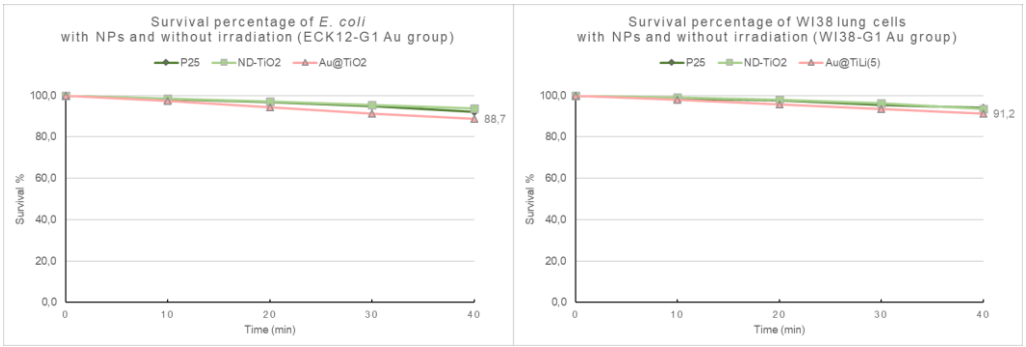

Figs. 97 a, b: comparison between the control groups and Au@TiLi(5) groups of E. coli and human lung cells with NPs and without irradiation (G1).

Figs. 97 a and b show the comparison between the control groups and the Au@TiLi(5) core shells NPs. In both cases, the samples with the core shells have a mortality level similar to the one of the control samples.

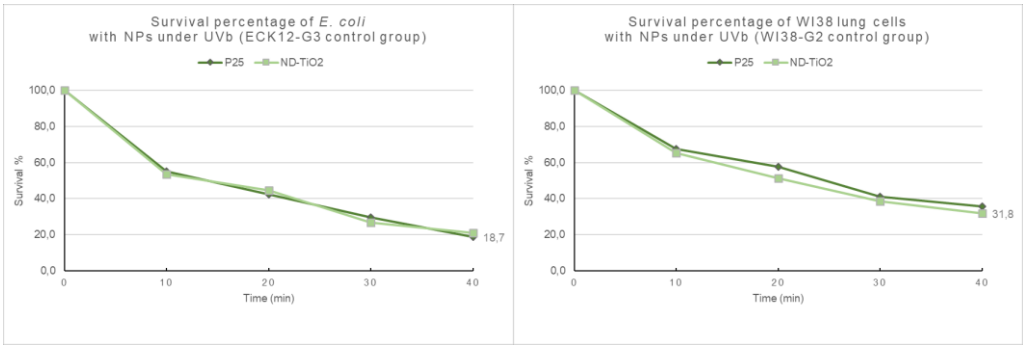

Figs. 98 a, b: comparison between the control groups of E. coli and human lung cells with NPs under UVb irradiation (G2).

Figs. 98 a and b show the control groups G2 of the bacteria and human cells with the P25 and ND-TiO_2 under ultraviolet light (290 nm). In this case, we can notice that the activation of photocatalysis, together with the ability of damage of the ultraviolet light, increases the mortality in both samples. In the case of *E. coli*, the mortality level is very high (around 82% in 40 minutes), while for human lung cells it is around 68%.

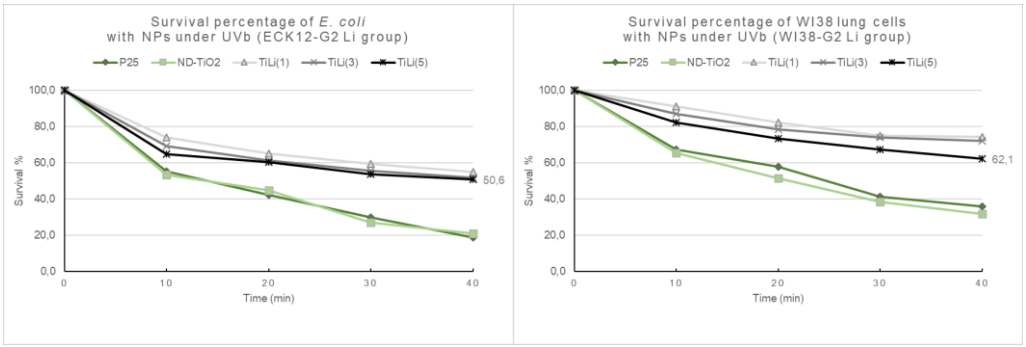

Figs. 99 a, b: comparison between the control groups and TiLi groups of E. coli and human lung cells with NPs under UVb irradiation (G2).

Figs. 99 a and b show the comparison between the control groups and the TiLi NPs groups in presence of UVb light. In this case, it is very important to notice that, in general, the mortality level is lower in the groups with the doped nanoparticles than in the control groups. Surely, some of the cells in both groups die due to ultraviolet

irradiation, but we are led to think that the replacement of H^+ ions with Li^+ ions causes a decrease in cellular mortality both in the case of *E. Coli* and in the case of human cells.

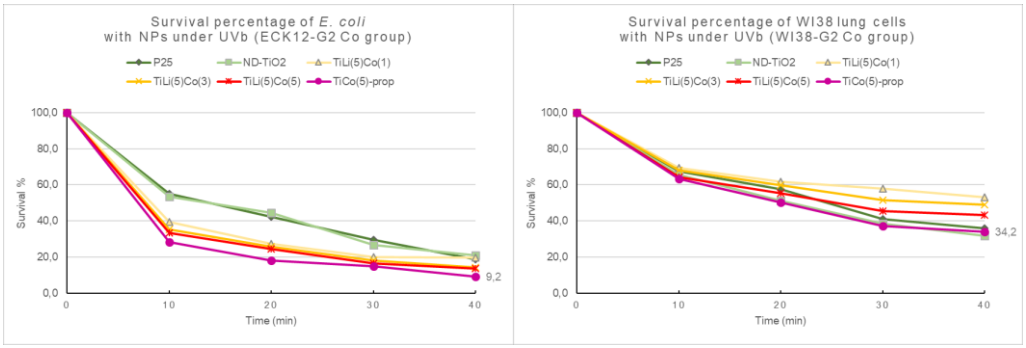

Figs. 100 a, b: comparison between the control groups and Co groups of E. coli and human lung cells with NPs under UVb irradiation (G2).

Figs. 100 a and b show the comparison between the control groups and the Co doped NPs groups under the UVb irradiation. The *E. coli* group showed a very important increase of the mortality level, which is over 90% after 40 minutes. The mortality level for human lung cells was also high, and amounted to about 65% after 40 minutes.

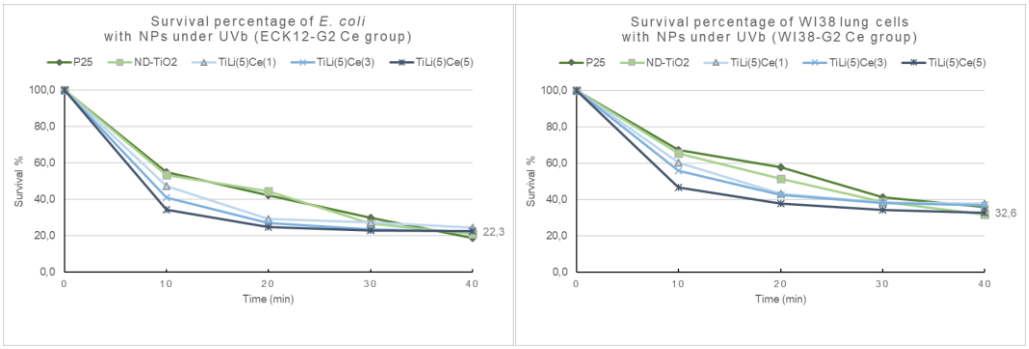

Figs. 101 a, b: comparison between the control groups and Ce groups of E. coli and human lung cells with NPs under UVb irradiation (G2).

Figs. 101 a and b show the comparison between the control groups and the TiLiCe doped NPs groups under UVb irradiation. Mortality in *E. coli* group is about 10% greater than in the human lung cells group. After 40 minutes, the percentage of surviving cells is around 22% for the *E. coli*, and around 32% for the human lung cells.

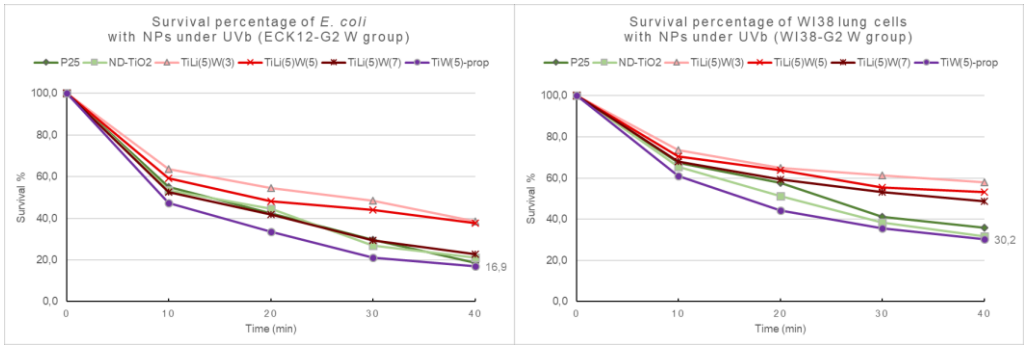

Figs. 102 a, b: comparison between the control groups and W groups of E. coli and human lung cells with NPs under UVb irradiation (G2).

Figs. 102 a and b show the comparison between the control groups and the W doped NPs groups under UVb irradiation. The *E. coli* group shows a very important increase of mortality, which is around 83% after 40 minutes. For human lung cells, the mortality is high as well, amounting to about 70% after 40 minutes.

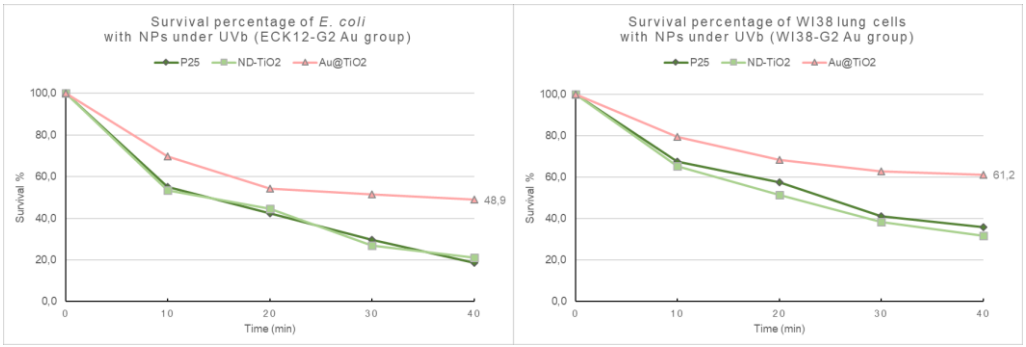

Figs. 103 a, b: comparison between the control groups and Au groups of E. coli and human lung cells with NPs under UVb irradiation (G2).

In the case of Au@TiLi(5) NPs shown in figs. 103 a and b, we can notice that in both cases, the mortality is lower than for the control samples under UVb irradiation.

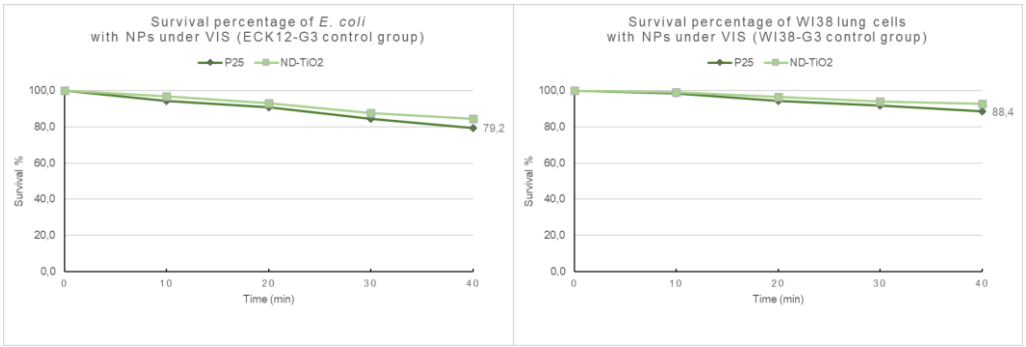

Figs. 104 a, b: comparison between the control groups of E. coli and human lung cells with NPs under VIS irradiation (G3).

Figs. 104 a and b show the control groups G3 of the bacteria and human cells together with the P25 and ND-TiO_2, under visible light (420 nm). In this case, we can notice that there is no activation of photocatalysis, and that the mortality rate is very low in both cases: for *E. coli*, the mortality is around 21%, while for human lung cells it is around 11%.

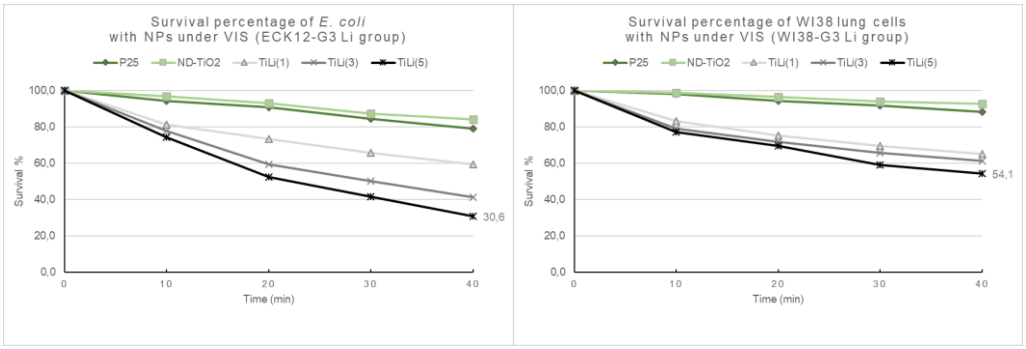

Figs. 105 a, b: comparison between the control groups and Li groups of E. coli and human lung cells with NPs under VIS irradiation (G3).

Figs. 105 a and b showthe comparison between the control groups G3 and the TiLi NPs group under visible light. In this case, we can notice that the activation of photocatalysis increases the mortality rate mostly in the *E. coli* samples, and seems to be linear and depending on the amount of dopant. A comparison with figs. 93 and 99 leads us to think that it is not the dopant itself that increases the toxicity, but rather the increase of photocatalytic activity in the visible region of our nanoparticles.

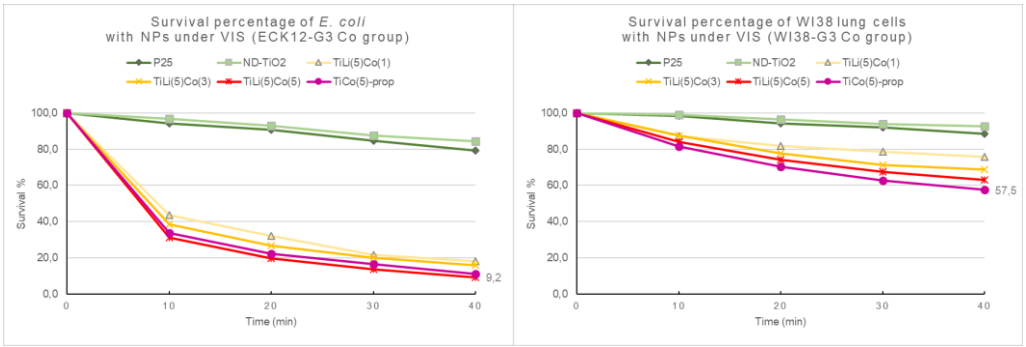

Figs. 106 a, b: comparison between the control groups and Co groups of E. coli and human lung cells with NPs under VIS irradiation (G3).

Figs. 106 a and b show the comparison between the control groups and the Co doped NPs groups under visible light. In this case, we can see how the mortality of *E. Coli* is very pronounced, reaching a maximum of about 91% after 40 minutes. In the case of human lung cells, we can notice that mortality is high (43% circa), but that it seems to depend principally on the amount of dopant. The figure is comparable to the mortality level observed in the control samples without irradiation in fig. 94. This leads us to think that for human cells, the presence of a dopant, rather than photocatalysis, represents the main factor determining the level of toxicity.

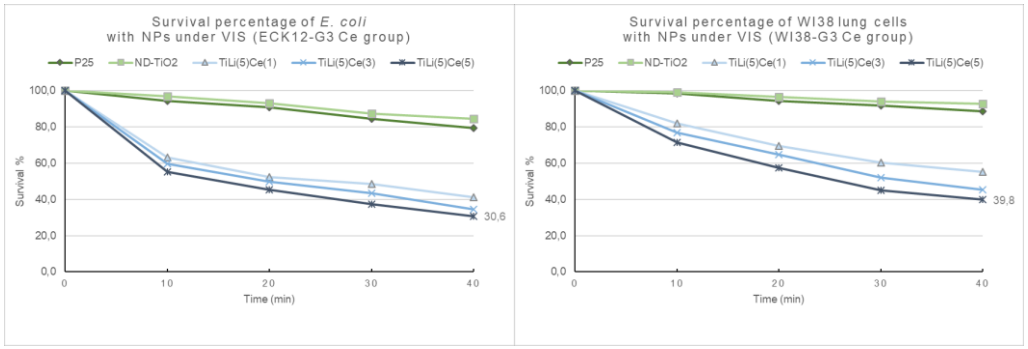

Figs. 107 a, b: comparison between the control groups and Ce groups of E. coli and human lung cells with NPs under VIS irradiation (G3).

Figs. 107 a and b show the comparison between the control groups and the TiLiCe doped NPs groups under visible light irradiation. Also in this case, the mortality in *E. coli* group is about 10% greater than in the human lung cells group. After 40 minutes, the survival cells percentage is around 30% for the *E. coli* and 40% for the human lung cells.

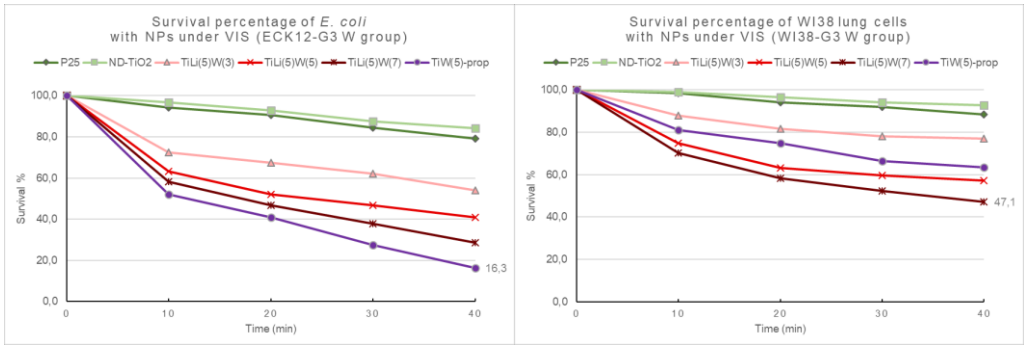

Figs. 108 a, b: comparison between the control groups and W groups of E. coli and human lung cells with NPs under VIS irradiation (G3).

Figs. 108 a and b show the comparison between the control groups and the W doped NPs groups under visible light. As in the case of cobalt, we can see that the mortality of *E. Coli* is very pronounced, and reaches a maximum of about 83% after 40 minutes. In the case of human lung cells, we can notice that mortality is high (around 53%) but it is comparable with the control samples without irradiation in fig. 96. This leads us to think again that toxicity, in the case of human cells, is mostly determined not by photocatalysis, but rather by the presence of a dopant. For all cases, mortality seems to depend on the amount of dopant.

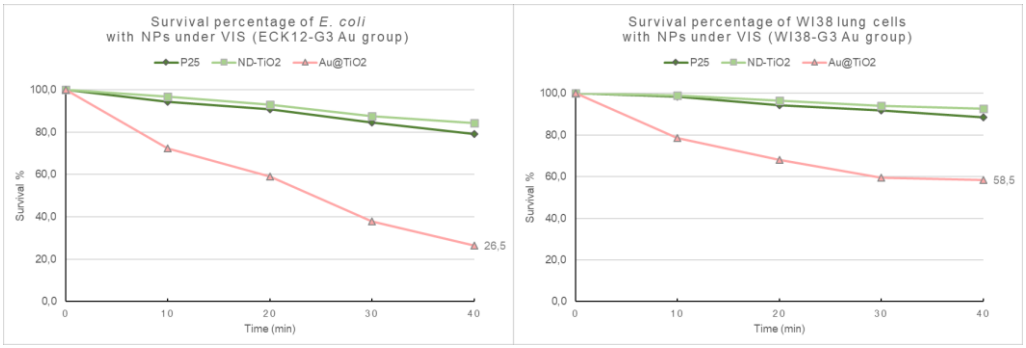

Figs. 109 a, b: comparison between the control groups and Au groups of E. coli and human lung cells with NPs under VIS irradiation (G3).

Figs. 109 a and b show the comparison between the control groups and the Au@TiLi(5) NPs. In the case of *E. coli*, it is possible to notice that photoactivation is responsible for the high mortality of the cells, which reaches around 74% after 40 minutes. In the case of human lung cells, the mortality is around 42%.

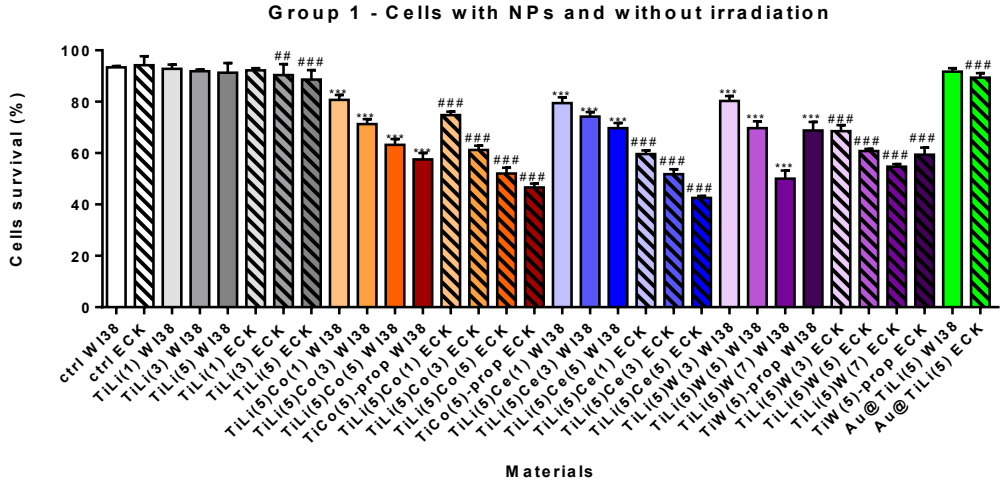

*Fig. 110: Percentage of cells survival in WI38 and ECK treated with not doped NPs and with doped-NPs without irradiation. The treated cells, when compared vs. WI38 and p<0.0001 are indicated with "***"; in the case of ECK cells and p<0.0001 they are indicated with "###" and p<0.001 with "##".*

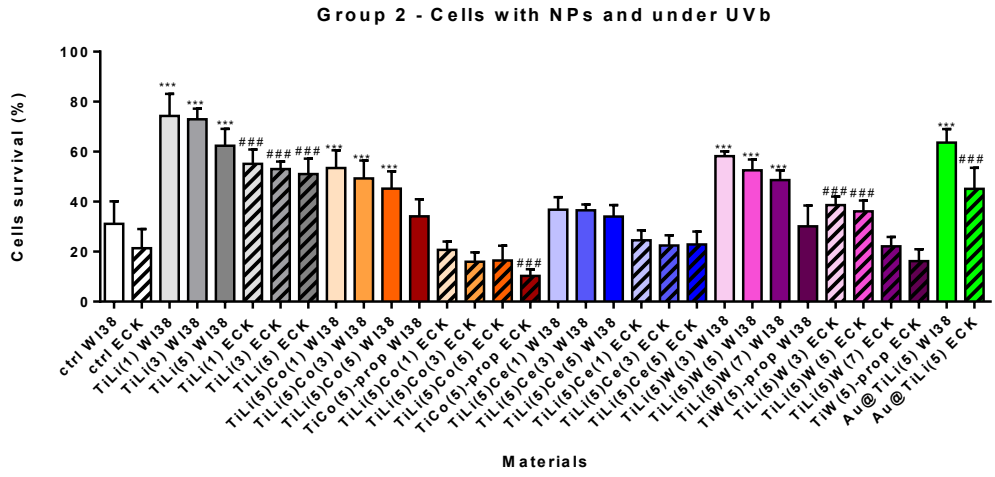

*Fig. 111: Percentage of cells survival exposed to UVb light in WI38 and ECK treated with ND-NPs doped NPs. The treated cells, when compared vs. WI38 and p<0.0001 are indicated with "***"; in the case of ECK cells and p<0.0001 they are indicated with "###".*

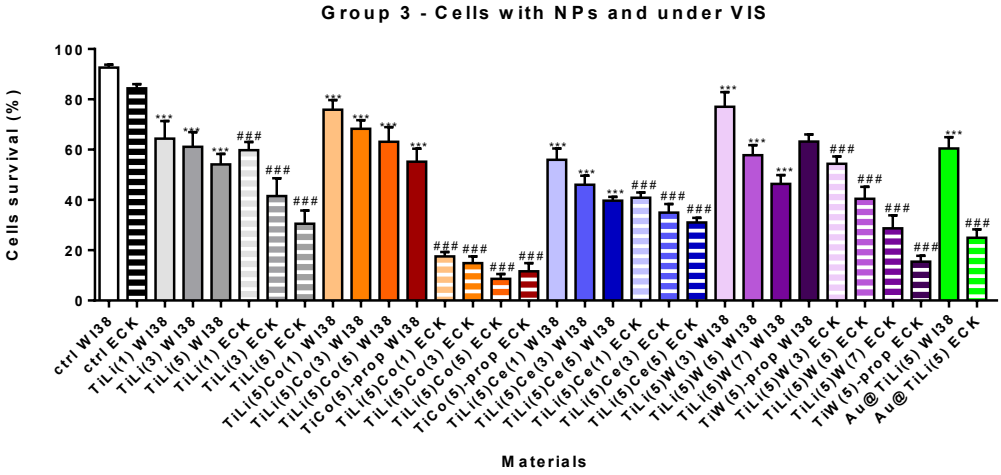

*Fig. 112: Percentage of cells survival exposed to visible light in WI38 and ECK treated with ND-NPs and with doped NPs. The treated cells, when compared vs. WI38 and p<0.0001 are indicated with "***"; in the case of ECK cells and p<0.0001 they are indicated with "###".*

All analyses were performed in GraphPad Prism Software v.6.1 using one-way ANOVA and Tukey's Multiple Comparison Test.

In Group 1 (fig. 110), cells had been treated with NPs only, without irradiations. Compounds TiLi(1), TiLi(3), and TiLi(5) in WI38 showed not significant differences with the control group, but ECK TiLi(1) showed no difference vs. ECK control group, while TiLi(3) and TiLi(5) showed a drop in cells' survival ($p<0.001$ and $p<0.0001$, respectively). All other compounds showed a significant decrease in cells' survival, except for Au@TiLi(5) in WI38 vs control.

Group 2 in fig. 111 shows the percentage of cells survival when exposed to UVb light in WI38 and ECK treated with NPs only, and with NPs with all compounds. In this case, WI38 and ECK treated with NPs exhibit a similar level of mortality. TiLi compounds were more stable under UVb, no matter whether in WI38 or ECK cells ($p<0.0001$). TiLi-TiCo groups compounds showed more variability in results: in WI38 cells TiLi(5)Co(1),(3),and (5) showed lower mortality in respect to the ECK, but TiCo(5)-prop showed no difference with NPs only; in ECK the toxicity seems to become worse according to the significance value in cells treated with TiCo(5)-prop. Compounds with Ce showed no significant values, while compounds with Au

showed in both WI38 and ECK protection. TiLi(5)W(3) and W(5) showed an increase in cells survival in both WI38 and ECK protection, TiLi(5)W(7) just in WI38, but no significant value in ECK; lastly, TiW(5)-prop showed no significant values in both WI38 and ECK.

Group 3 in fig. 112 shows what happens when the cells were exposed to visible light. All compounds versus their controls groups showed a significant toxicity both in WI38 and ECK ($p<0.0001$).

Oxidative stress markers

Lactate dehydrogenase (LDH) release

Lactate dehydrogenase (LDH) is a cytosolic enzyme present in many different cell types. When its plasma membrane is damaged, a cell releases LDH into the cell culture medium. The amount of extracellular LDH in the medium can be quantified by a coupled enzymatic reaction in which LDH catalyzes the conversion of lactate to pyruvate via the reduction of NAD+ to NADH. Diaphorase then uses NADH to reduce a tetrazolium salt to a red formazan product that can be measured at 490nm. The level of formazan formation is

directly proportional to the amount of LDH released into the medium, which is indicative of the cytotoxicity of an agent [172].

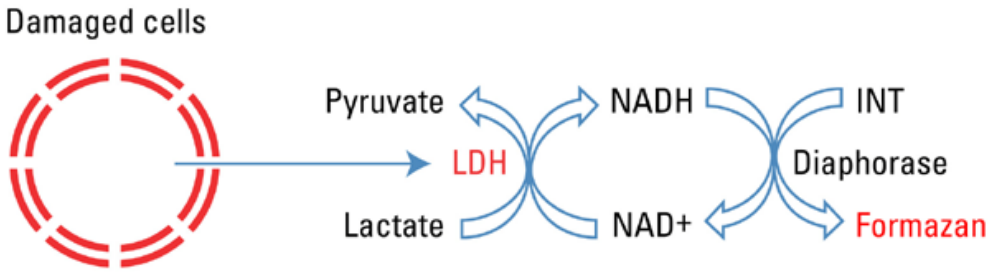

Fig. 113: Schematic of LDH cytotoxicity assay mechanism [172]

The samples for the LDH assay were prepared following a validated method for TiO_2 NPs [170], using a *Pierce LDH Cytotoxicity Assay Kit* (ThermoFisher). One milliliter of cells at a density of 5×10^5 cells/ml in Gibco RPMI 1640 containing 10% of Fetal Bovine Serum (ThermoFisher) was used for each experiment; the cells were seeded in each well plate, and grown for 48 h before their exposure to NPs. The cells were then washed with Hank's Balanced Salt Solution (Gibco) three times, and exposed to NPs in RPMI medium containing 1% FBS.

After a 40 minutes exposure, the well plates were shaken briefly to homogenize the LDH that had been released in the cell culture media; afterward, the media was transferred into 1.5 ml microcentrifuge Eppendorf tubes, and were centrifuged at 10,000 × g and 4 °C for 15 min to remove any cell debris and NPs. One hundred microliters (100 µL) of each sample was transferred to a new plate and mixed with the reaction mixture of the kit (ThermoFisher). After 30 minutes at room temperature (25 °C), the reactions were stopped by adding the stop solution. Absorbance at 490 nm was measured using a plate-reading spectrophotometer (BioTek Synergy 2 SLFA Multi-Mode Plate Reader) to determine the LDH activity.

For the LDH assay, six groups of tests in triplicate were carried out with the same cells and at the same conditions as for the WST-1 tests, but with five different NPs concentrations (0.06, 0.6, 6, 60, 600 µg/ml) in addition to the control samples without NPs:

- group one (J1): WI38-J1 (86 wells) and ECK12-J1 (86 wells) with NPs but in absence of irradiation;
- group two (J2): WI38-J2 (86 wells) and ECK12-J2 (86 wells) with NPs and with the exposure to UVa irradiation (290 nm, 4.3 mW cm^{-2});

- group three (J3): WI38-J3 (86 wells) and ECK12-J3 (86 wells) with NPs and with the exposure to visible light (420 nm of maximum peak and a bandpass filter of 400 nm, 4.1 $mWcm^{-2}$).

The data were reported as the percentage of the released amount of LDH compared to the LDH amount of the control samples (100%). All analyses were performed with GraphPad Prism Software v.6.1 using a two-way ANOVA and Bonferroni's Multiple Comparison Test. Figs. 114 to 118 show that all the NPs produced an increase of the amount of LDH after 40 minutes of treatment without any light irradiation. In particular, the TiLiCo group (fig. 115), the TiLiCe group (fig. 116), and the TiLiW group (fig. 117) showed statistically significant values ($p<0.0001$).

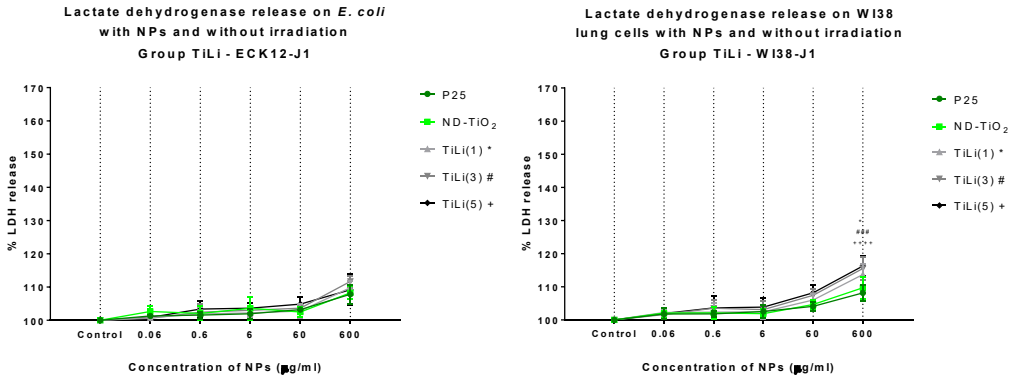

*Fig. 114: Lactate dehydrogenase release level on E. coli (left) and human lung cells (right) with TiLi NPs without any irradiation. (*p<0.05; **p<0.005; ***p<0.0005; ****p<0.0001; P25 vs. related NPs)*

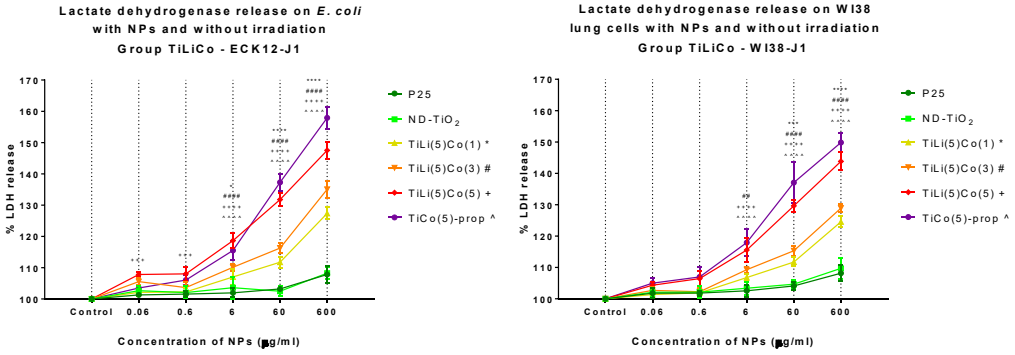

*Fig. 115: Lactate dehydrogenase release level on E. coli (left) and human lung cells (right) with TiLiCo NPs without any irradiation. (*p<0.05; **p<0.005; ***p<0.0005; ****p<0.0001; P25 vs. related NPs).*

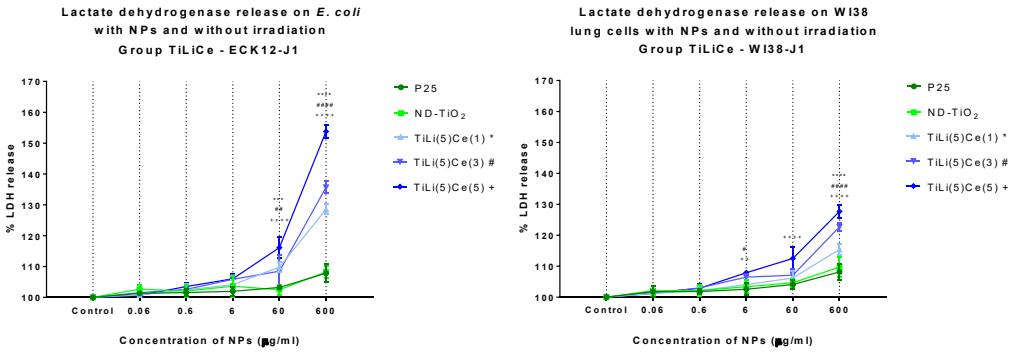

*Fig. 116: Lactate dehydrogenase release level on E. coli (left) and human lung cells (right) with TiLiCe NPs without any irradiation. (*p<0.05; **p<0.005; ***p<0.0005; ****p<0.0001; P25 vs. related NPs).*

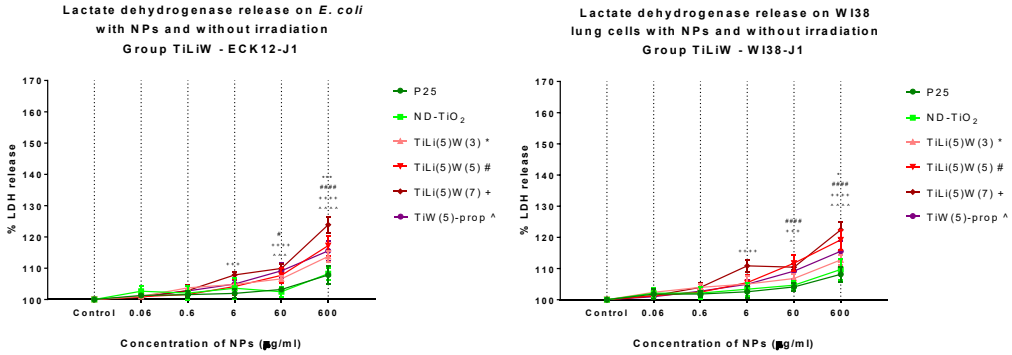

*Fig. 117: Lactate dehydrogenase release level on E. coli (left) and human lung cells (right) with TiLiW NPs without any irradiation. (*p<0.05; **p<0.005; ***p<0.0005; ****p<0.0001; P25 vs. related NPs).*

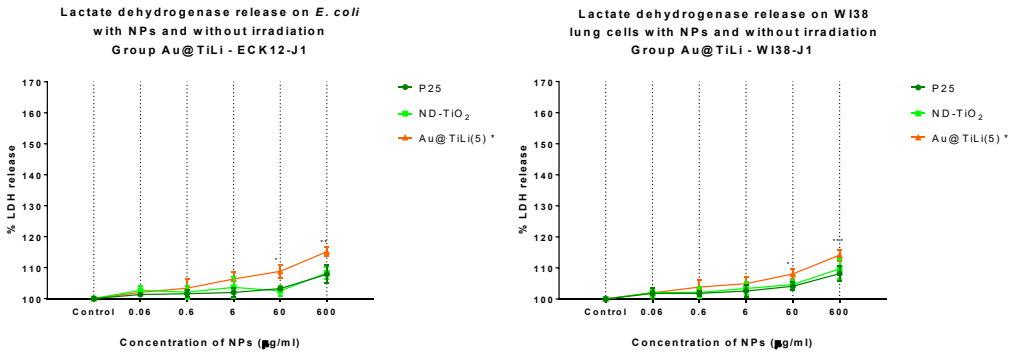

*Fig. 118 Lactate dehydrogenase release level on E. coli (left) and human lung cells (right) with Au@TiLi(5) NPs without any irradiation. (*p<0.05; **p<0.005; ***p<0.0005; ****p<0.0001; P25 vs. related NPs).*

Fig. 119 to 123 show that the increase of the amount of LDH with the NPs after 40 minutes of treatment under UVb light is not statistically significant (in most of the cases). In effect, it is due to the high absolute value of the control samples as can be seen from figure 130.

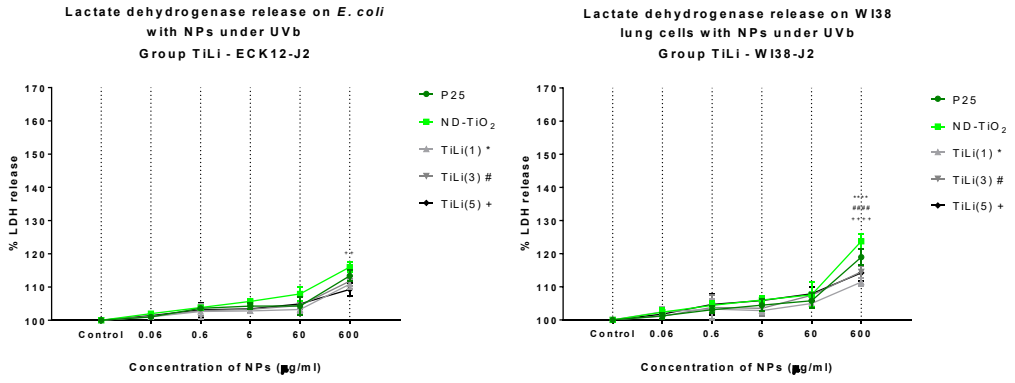

*Fig. 119: Lactate dehydrogenase release level on E. coli (left) and human lung cells (right) with TiLi NPs under UVb irradiation. (*p<0.05; **p<0.005; ***p<0.0005; ****p<0.0001; P25 vs. related NPs).*

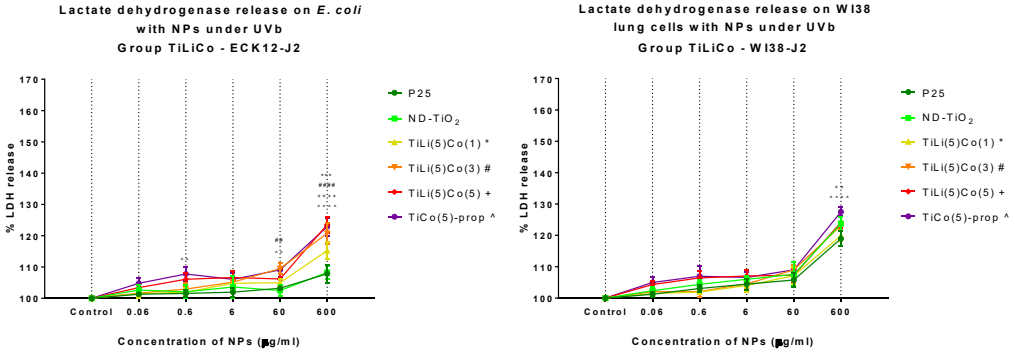

*Fig. 120: Lactate dehydrogenase release level on E. coli (left) and human lung cells (right) with TiLiCo NPs under UVb irradiation. (*p<0.05; **p<0.005; ***p<0.0005; ****p<0.0001; P25 vs. related NPs).*

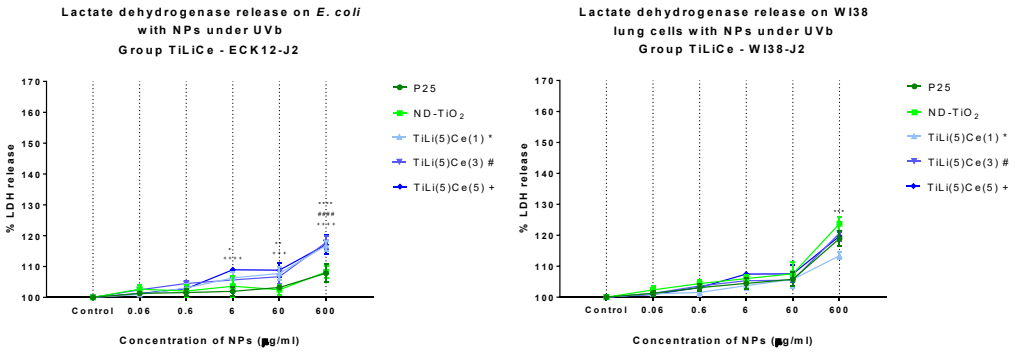

*Fig. 121: Lactate dehydrogenase release level on E. coli (left) and human lung cells (right) with TiLiCe NPs under UVb irradiation. (*p<0.05; **p<0.005; ***p<0.0005; ****p<0.0001; P25 vs. related NPs).*

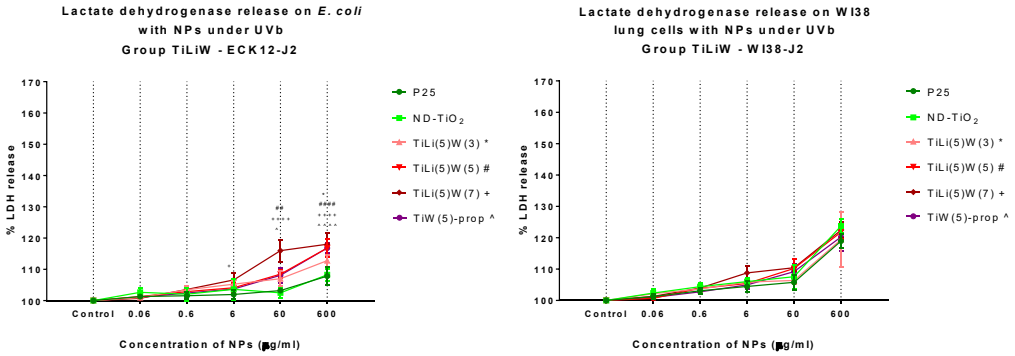

*Fig. 122: Lactate dehydrogenase release level on E. coli (left) and human lung cells (right) with TiLiW NPs under UVb irradiation. (*p<0.05; **p<0.005; ***p<0.0005; ****p<0.0001; P25 vs. related NPs).*

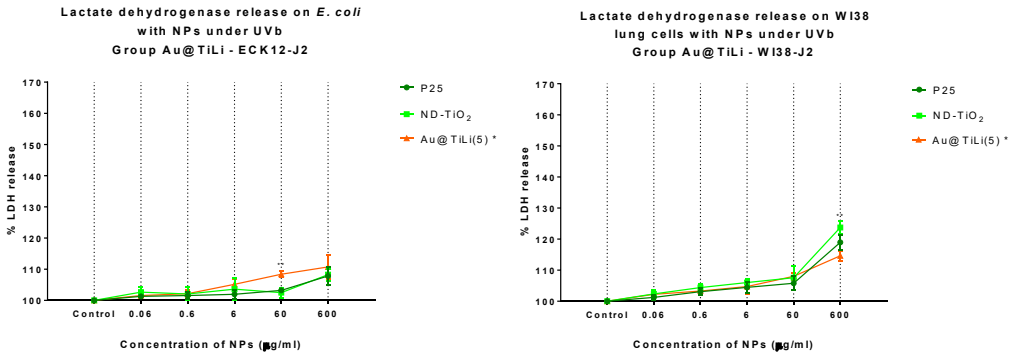

*Fig. 123: Lactate dehydrogenase release level on E. coli (left) and human lung cells (right) with Au@TiLi(5) NPs under UVb irradiation. (*p<0.05; **p<0.005; ***p<0.0005; ****p<0.0001; P25 vs. related NPs).*

Fig. 124 to 128 show that all the NPs produced an increase of the amount of LDH after 40 minutes of treatment under visible light irradiation. All the groups showed statistically significant values ($p<0.0001$).

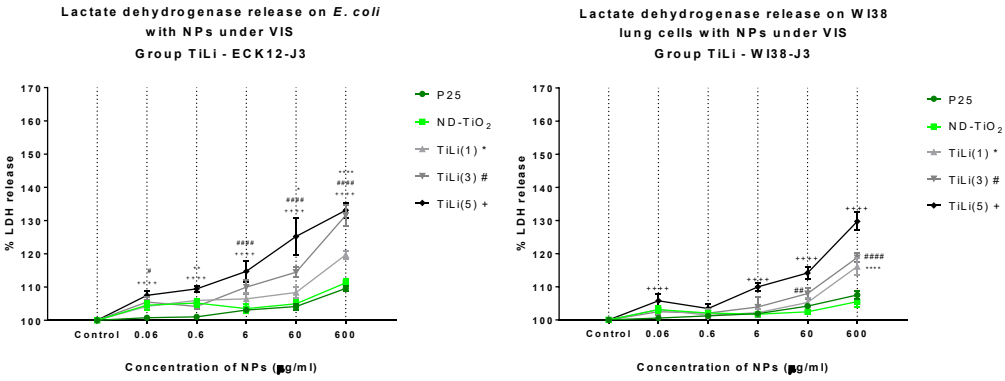

*Fig. 124: Lactate dehydrogenase release level on E. coli (left) and human lung cells (right) with TiLi NPs under visible light irradiation. (*p<0.05; **p<0.005; ***p<0.0005; ****p<0.0001; P25 vs. related NPs)*

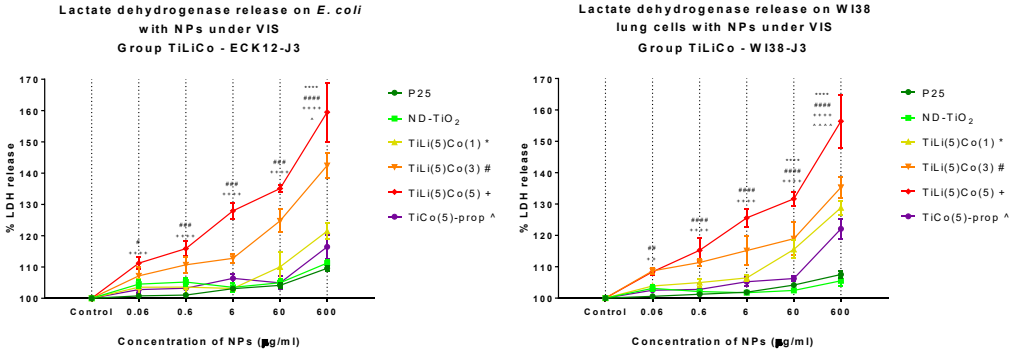

*Fig. 125: Lactate dehydrogenase release level on E. coli (left) and human lung cells (right) with TiLiCo NPs under visible light irradiation. (*p<0.05; **p<0.005; ***p<0.0005; ****p<0.0001; P25 vs. related NPs)*

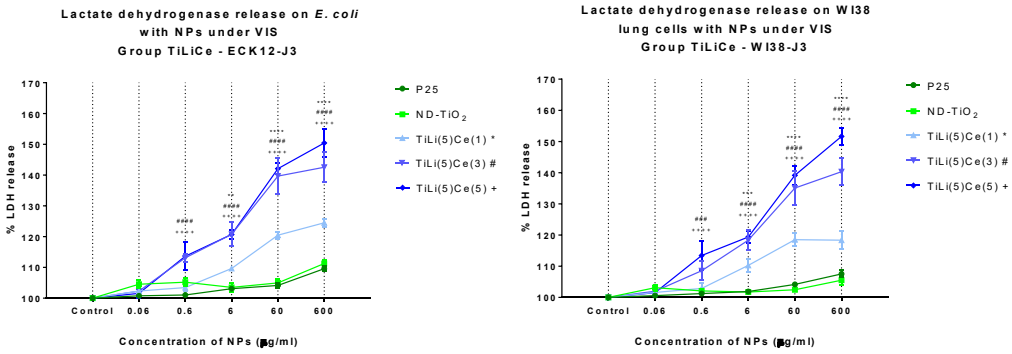

*Fig. 126: Lactate dehydrogenase release level on E. coli (left) and human lung cells (right) with TiLiCe NPs under visible light irradiation. (*p<0.05; **p<0.005; ***p<0.0005; ****p<0.0001; P25 vs. related NPs)*

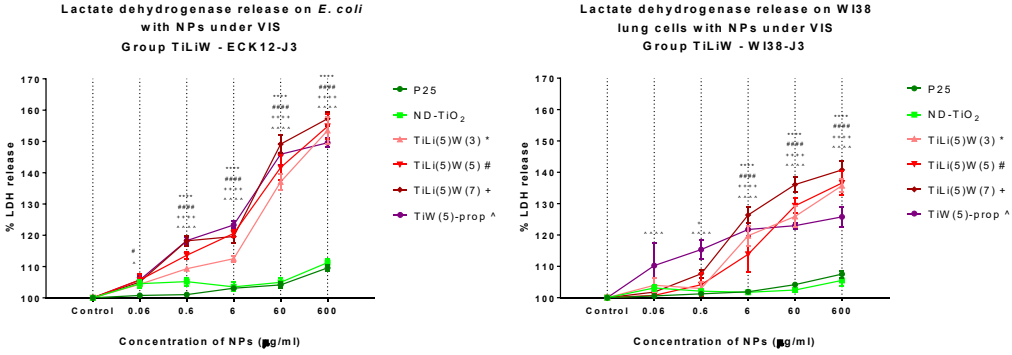

*Fig. 127: Lactate dehydrogenase release level on E. coli (left) and human lung cells (right) with TiLiW NPs under visible light irradiation. (*p<0.05; **p<0.005; ***p<0.0005; ****p<0.0001; P25 vs. related NPs)*

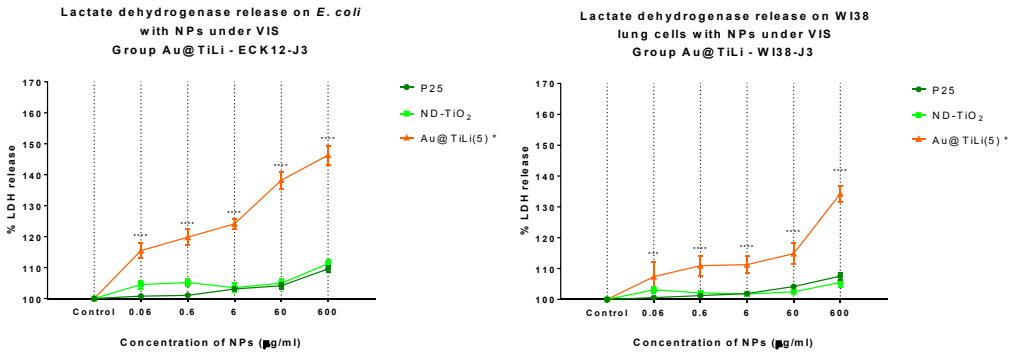

*Fig. 128: Lactate dehydrogenase release level on E. coli (left) and human lung cells (right) with Au@TiLi(5) NPs under visible light irradiation. (*p<0.05; **p<0.005; ***p<0.0005; ****p<0.0001; P25 vs. related NPs).*

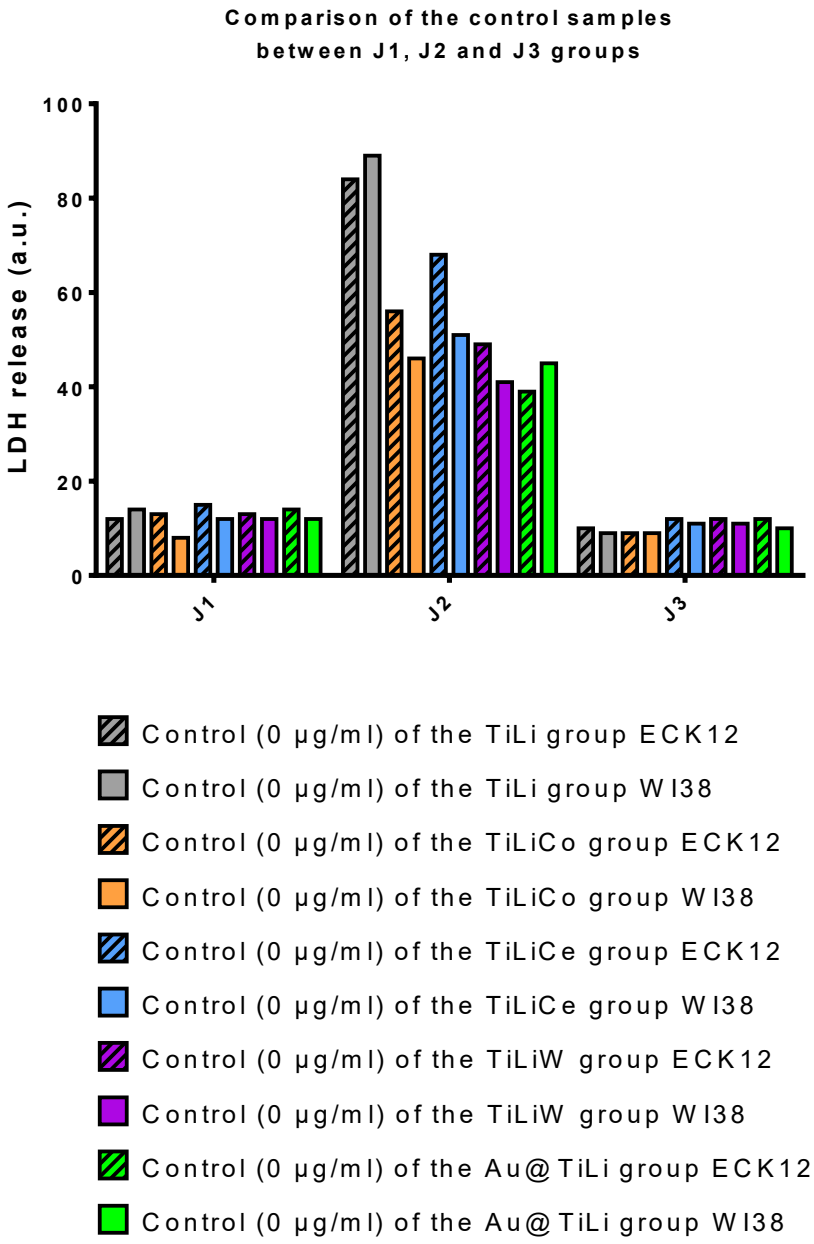

Fig. 129: Comparison of the not normalized values of the control samples (NPs-free) between J1, J2 and J3 groups.

Determination of reactive oxygen species (ROS)

Intracellular ROS in the human and bacterial cells were measured using the protocol described by Lyon et al [173] and by Kumar et al. [174]. The 2′,7′-dichlorodihydrofluorescein diacetate (H_2DCFDA, Sigma Aldrich) and hydroethidine (HEt, Sigma Aldrich), were used to measure ROS in and around the bacterial cells via increases in fluorescence as measured using a fluorimeter (Thermo Qubit 3). HEt has blue fluorescence in the cytoplasm and it is added at a final concentration of 100 µM to cells with or without NPs, and the dye is oxidized by superoxide to form an ethidium compound that fluoresces red when bound to DNA [175]. H_2DCFDA is nonfluorescent until it enters the cell, whereupon it is cleaved by an esterase, which improves cell retention and allows the compound to be oxidized (and fluoresce) by most ROS species. The protocol involved incubating the cells with 200 µM of H_2DCFDA for 30 min,

then harvesting the exposed cells by centrifugation, resuspending them in the medium such that the intracellular esterases could cleave the dye for 10 min, and finally exposing the cells to NPs for another 15 min. Data were interpreted relative to NPs-free controls (100%) with *E. coli* and human lung cells.

For the ROS assays, six groups of tests in triplicate were carried out with the same cells and at the same conditions as for the LDH tests, with five different NPs concentrations (0.06, 0.6, 6, 60, 600 μg/ml) in addition to the control samples without NPs:

- group one (R1): WI38-R1 (86 wells) and ECK12-R1 (86 wells) with NPs but in absence of irradiation;
- group two (R2): WI38-R2 (86 wells) and ECK12-R2 (86 wells) with NPs and with the exposure to UVa irradiation (290 nm, 4.3 mW cm^{-2});
- group three (R3): WI38-R3 (86 wells) and ECK12-R3 (86 wells) with NPs and with the exposure to visible light (420 nm of maximum peak and a bandpass filter of 400 nm, 4.1 $mWcm^{-2}$).

The data were reported as the percentage of the released amount of ROS compared to the ROS amount of the control (100%).

All the assays for the determination of ROS confirm the data obtained with LDH. Oxidative stress is present in all groups, in particular in those with the photocatalytic activation by UVb and visible light.

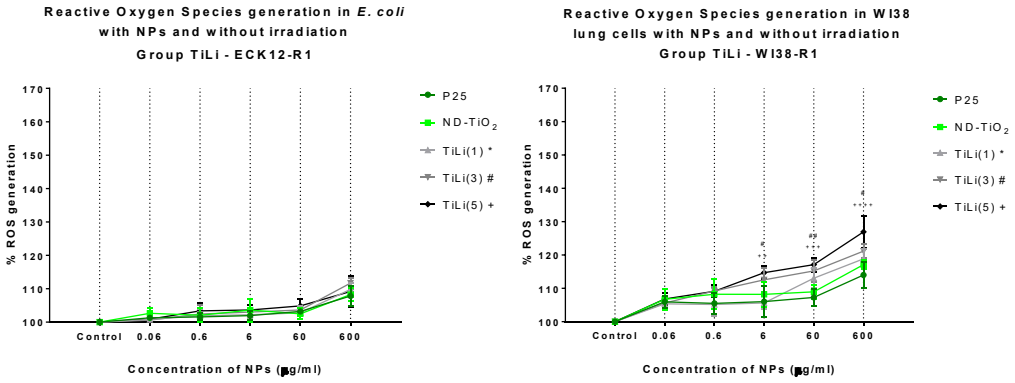

*Fig. 130: Intracellular Reactive Oxygen Species generation in E. coli (left) and human lung cells (right) with TiLi group NPs without irradiation. (*p<0.05; **p<0.005; ***p<0.0005; ****p<0.0001; P25 vs. related NPs)*

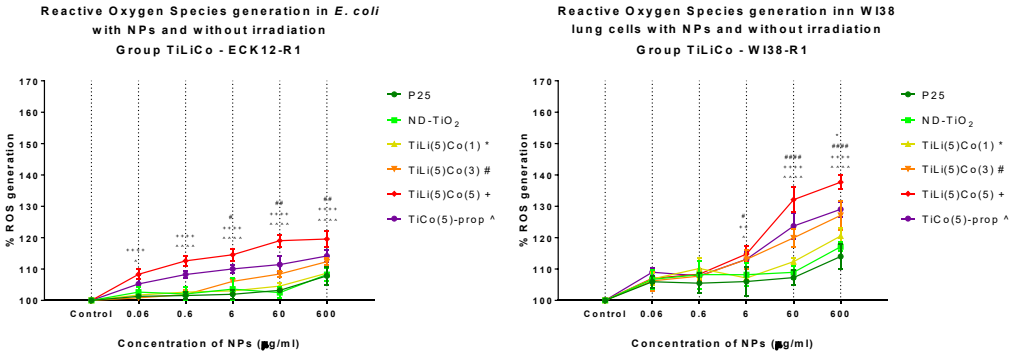

*Fig. 131: Intracellular Reactive Oxygen Species generation in E. coli (left) and human lung cells (right) with TiLiCo group NPs without irradiation. (*p<0.05; **p<0.005; ***p<0.0005; ****p<0.0001; P25 vs. related NPs)*

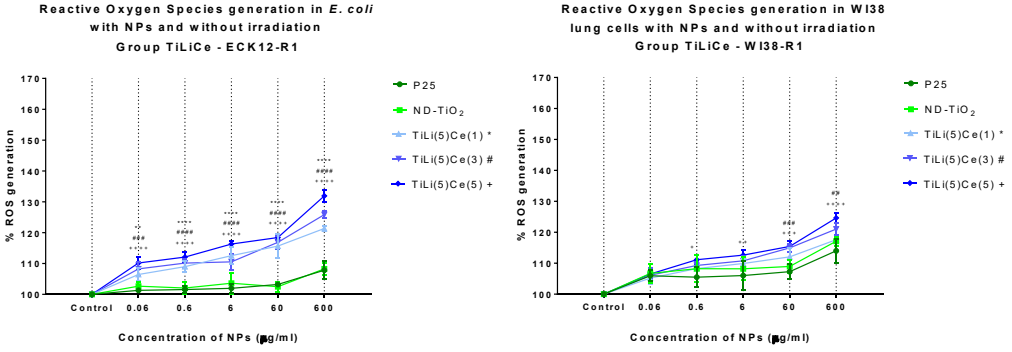

*Fig. 132: Intracellular Reactive Oxygen Species generation in E. coli (left) and human lung cells (right) with TiLiCe group NPs without irradiation. (*p<0.05; **p<0.005; ***p<0.0005; ****p<0.0001; P25 vs. related NPs)*

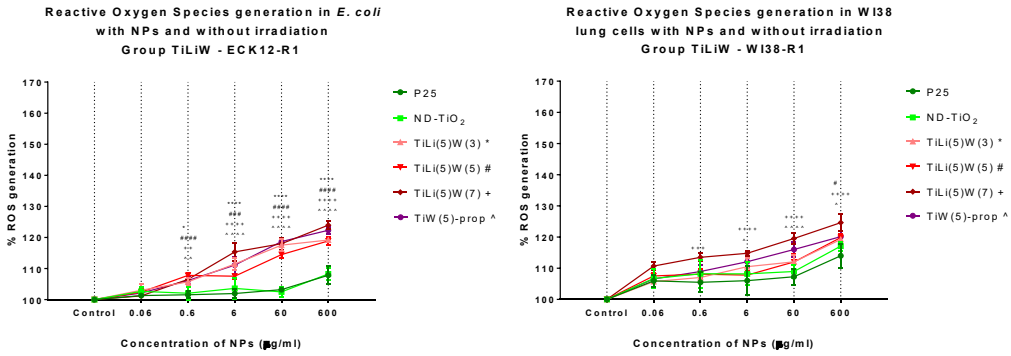

*Fig. 133: Intracellular Reactive Oxygen Species generation in E. coli (left) and human lung cells (right) with TiLiW group NPs without irradiation. (*p<0.05; **p<0.005; ***p<0.0005; ****p<0.0001; P25 vs. related NPs)*

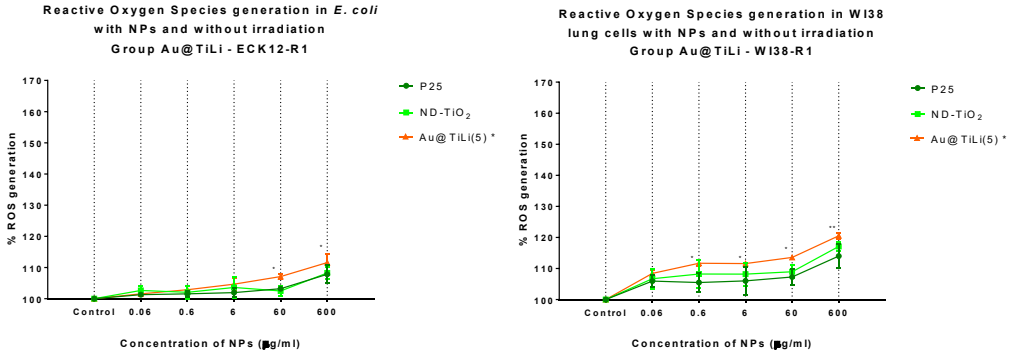

*Fig. 134: Intracellular Reactive Oxygen Species generation in E. coli (left) and human lung cells (right) with Au@TiLi group NPs without irradiation. (*p<0.05; **p<0.005; ***p<0.0005; ****p<0.0001; P25 vs. related NPs)*

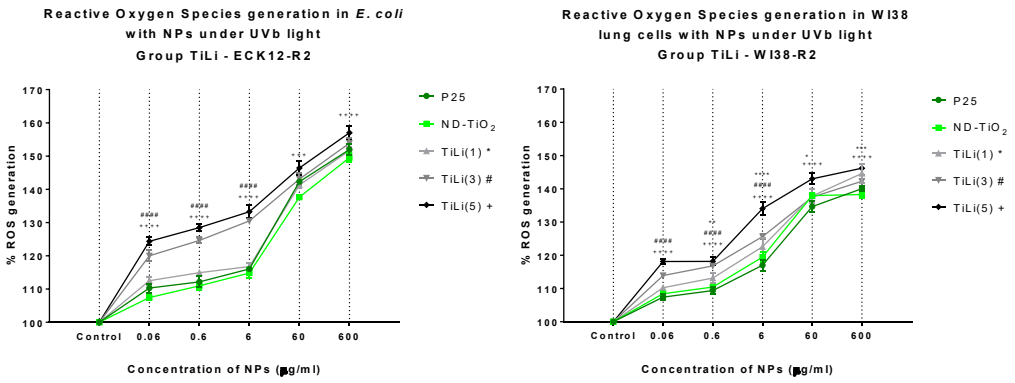

*Fig. 135: Intracellular Reactive Oxygen Species generation in E. coli (left) and human lung cells (right) with TiLi group NPs under UVb light. (*p<0.05; **p<0.005; ***p<0.0005; ****p<0.0001; P25 vs. related NPs)*

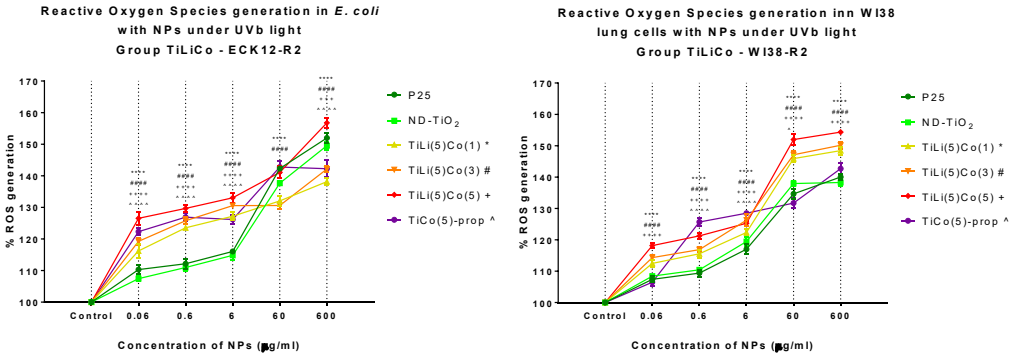

*Fig. 136: Intracellular Reactive Oxygen Species generation in E. coli (left) and human lung cells (right) with TiLiCo group NPs under UVb light. (*p<0.05; **p<0.005; ***p<0.0005; ****p<0.0001; P25 vs. related NPs)*

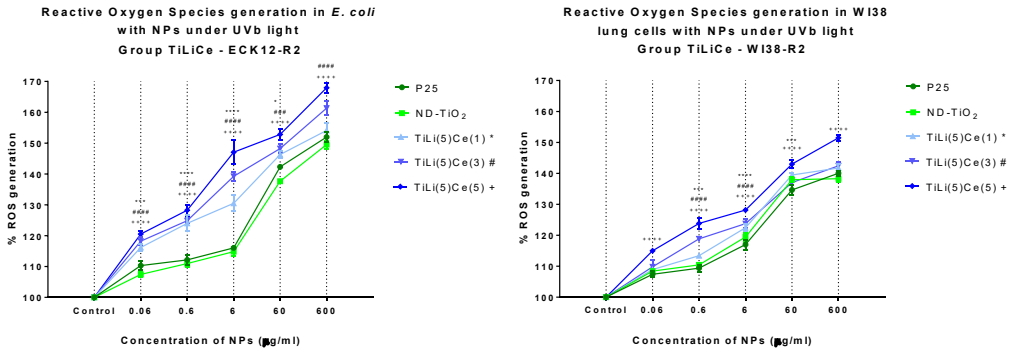

*Fig. 137: Intracellular Reactive Oxygen Species generation in E. coli (left) and human lung cells (right) with TiLiCe group NPs under UVb light. (*p<0.05; **p<0.005; ***p<0.0005; ****p<0.0001; P25 vs. related NPs)*

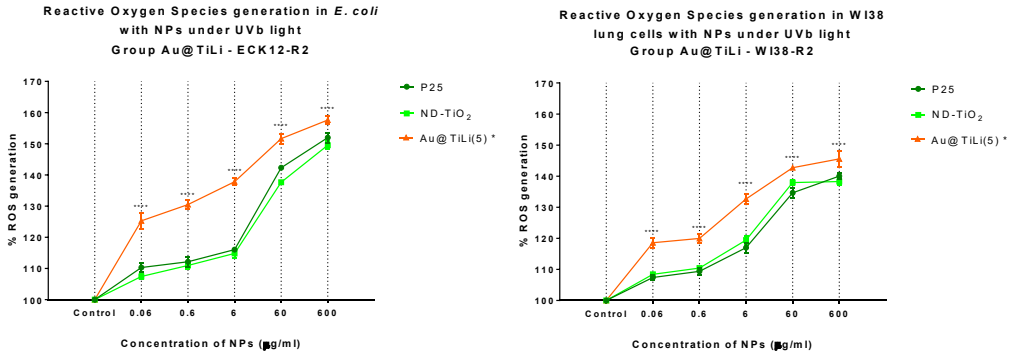

*Fig. 138: Intracellular Reactive Oxygen Species generation in E. coli (left) and human lung cells (right) with Au@TiLi group NPs under UVb light. (*p<0.05; **p<0.005; ***p<0.0005; ****p<0.0001; P25 vs. related NPs)*

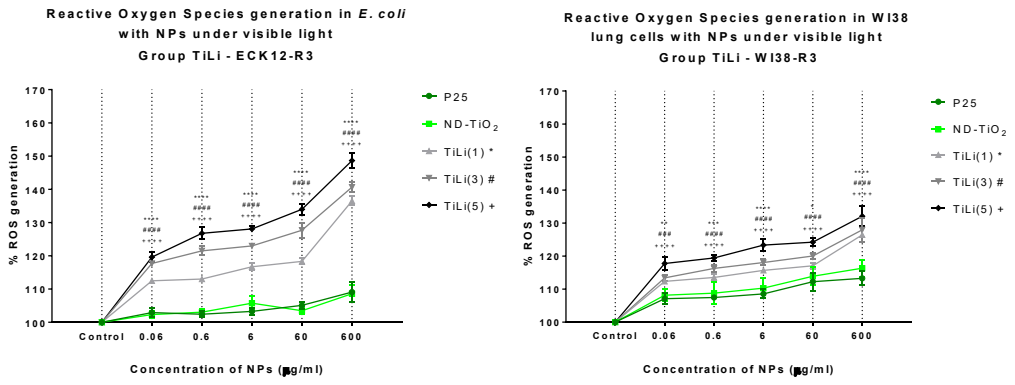

*Fig. 139 Intracellular Reactive Oxygen Species generation in E. coli (left) and human lung cells (right) with TiLi group NPs under visible light. (*p<0.05; **p<0.005; ***p<0.0005; ****p<0.0001; P25 vs. related NPs)*

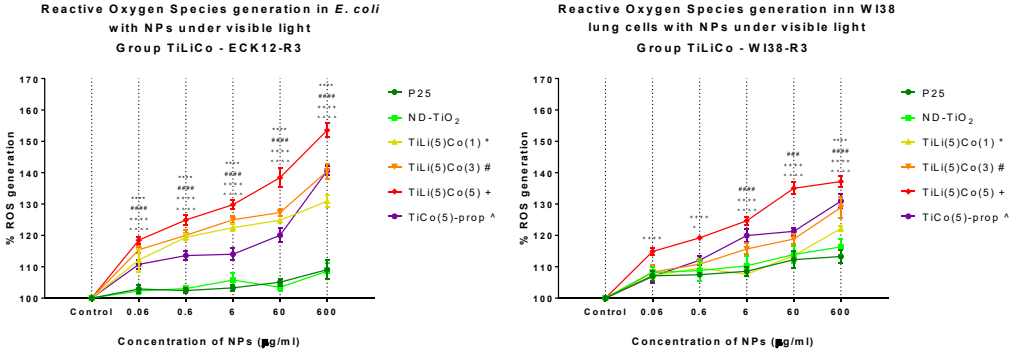

*Fig. 140 Intracellular Reactive Oxygen Species generation in E. coli (left) and human lung cells (right) with TiLiCo group NPs under visible light. (*p<0.05; **p<0.005; ***p<0.0005; ****p<0.0001; P25 vs. related NPs)*

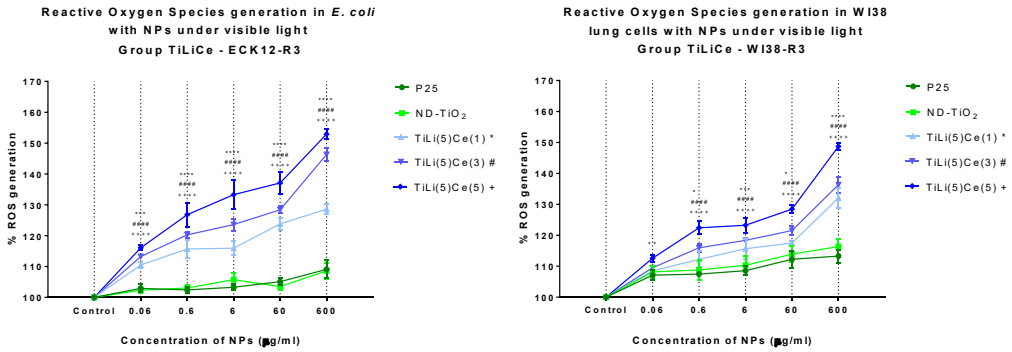

*Fig. 141 Intracellular Reactive Oxygen Species generation in E. coli (left) and human lung cells (right) with TiLiCe group NPs under visible light. (*p<0.05; **p<0.005; ***p<0.0005; ****p<0.0001; P25 vs. related NPs)*

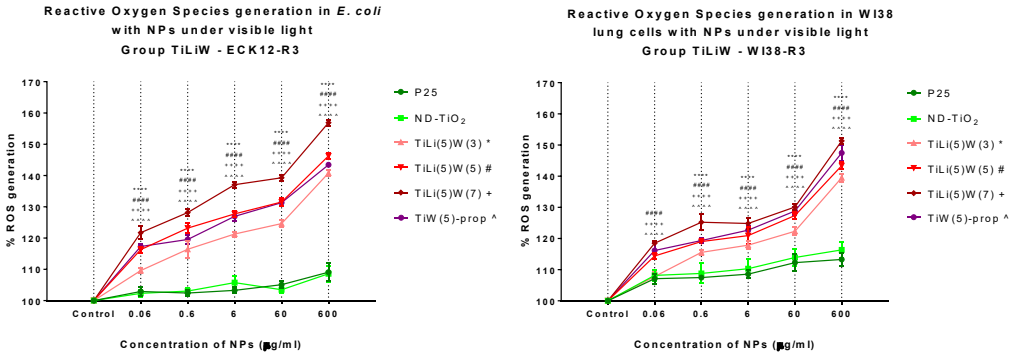

*Fig. 142 Intracellular Reactive Oxygen Species generation in E. coli (left) and human lung cells (right) with TiLiW group NPs under visible light. (*p<0.05; **p<0.005; ***p<0.0005; ****p<0.0001; P25 vs. related NPs)*

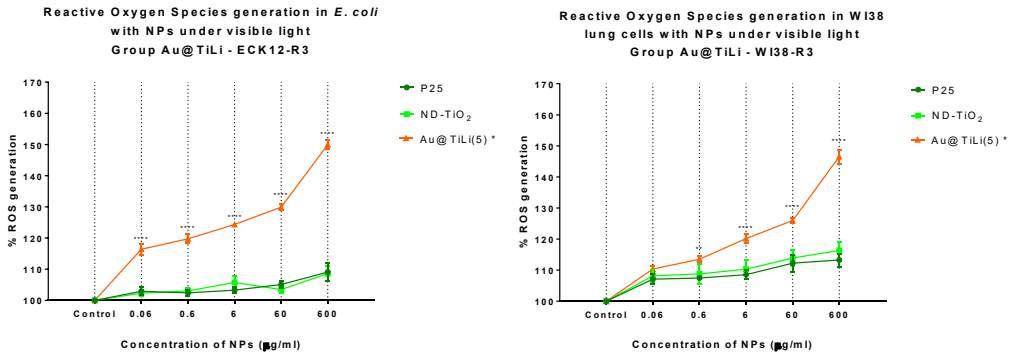

*Fig. 143 Intracellular Reactive Oxygen Species generation in E. coli (left) and human lung cells (right) with Au@TiLi group NPs under visible light. (*p<0.05; **p<0.005; ***p<0.0005; ****p<0.0001; P25 vs. related NPs)*

Conclusions

During this study, we were able to produce several new syntheses of Li-M co-doped TiO_2 anatase nanoparticles, nanosheets, and xerogels. Using a modified sol-gel with a two-steps desolvation method allowed us to obtain nanoparticles well dispersed in water, without having to resort to the use of organic surfactants and high temperature treatments. The syntheses described in this thesis can be considered as green methods for preparing such systems.

The particles we obtained from the syntheses were then doped with Li^+ ions to study the suitability of this ion as a replacement of the H^+ ion at the surface of the particles, and for maintaining a good dispersion of the particles in the solution. In effect, it has been shown that lithium ions are able to keep the nanoparticles dispersed

by electrostatic repulsion. Furthermore, lithium ions have a higher mobility than H^+ ions at the surface of the nanoparticles.

All materials were studied with the Brunauer–Emmett–Teller (BET) method in order to measure their relative surface areas. The NPs samples showed an increase of the relative surface areas in comparison with the standard samples, which constitutes the best increment observed for the nanosheets samples (446 $m^2 g^{-1}$).

The use of lithium, cobalt, cerium, and tungsten ions as dopants was studied through UV-Vis absorption measurements, which indicated an increased absorption in the visible range of the light spectrum, together with a decrease of the band gap for the doped samples in comparison with the pure TiO_2 sample

All nanoparticles and nanosheets were also investigated with several methods in order to evaluate their photocatalytic efficiency. Li-Co and Li-Ce doped nanoparticles showed very good results both in water solution and in gas phase. Under UVb light, the photocatalytic activity of our nanosystems is similar to the activity exhibited by the standard samples. However, under visible light, the doped NPs, in particular the Au@TiLi(5) and the TiLi(5)Co(5) samples, showed better results than the control samples. In conclusion, the NPs and

nanosheets materials we produced may be very good candidates for practical use in conditions of visible light irradiation.

All analyzed nanoparticles exhibited different photocatalytic activities for human cells and bacteria, particularly under irradiation.

Some transition metal doped nanoparticles also exhibited cytotoxicity in absence of illumination, probably resulting from their dopant content.

Therefore, the use of such systems could pose a risk for human health. However, if these compounds are merely inhaled, the lack of illumination inside the human body reduces the risk. For the TiLi and Au@TiLi(5) groups, the danger is virtually absent.

The toxicity on Escherichia coli cells is significantly higher in almost all cases. In the case of the TiLiCo group, in particular, there is a high difference between the level of toxicity for human cells, which is relatively low, and the level of toxicity for Escherichia coli, which is extremely high. This observation suggests that this type of material could be used as a bactericide in biological contaminated contexts.

Thus, the nanosystems we created are very effective as photocatalysts or as bactericidal systems with some surface

properties like superhydrophilicity and superoleophilicity. However, their use in indoor environments must include an adequate nanofiltration system at the exit of the reaction chambers to prevent the dispersion of the nanoparticles in the environment.

The production of a new Li-M co-doped TiO_2 based photocatalyst family, active in visible light, represents a remarkable advancement in research in the reference industry.

Appendix

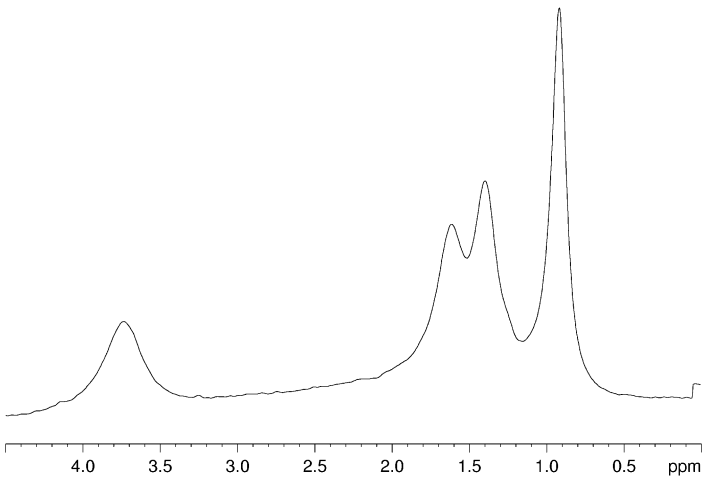

Fig. A: ^{1}H MAS NMR of the sample TiLiCl(5), peaks: 0.92, 1.40, 1.63, 3.74 ppm.

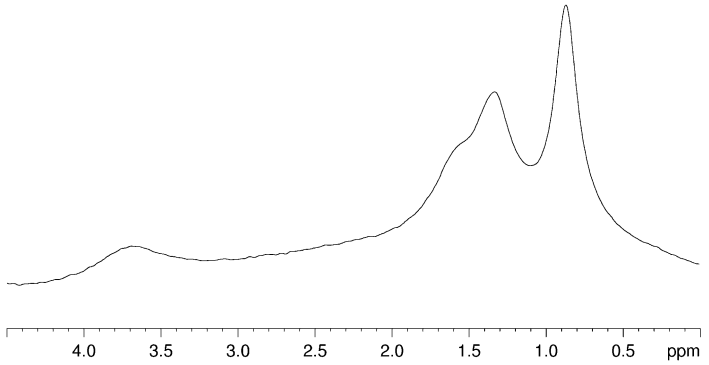

Fig. B: ^{1}H MAS NMR of the sample TiLiCl-acid intermediate, peaks: 0.88, 1.36, 1.61, 3.70 ppm.

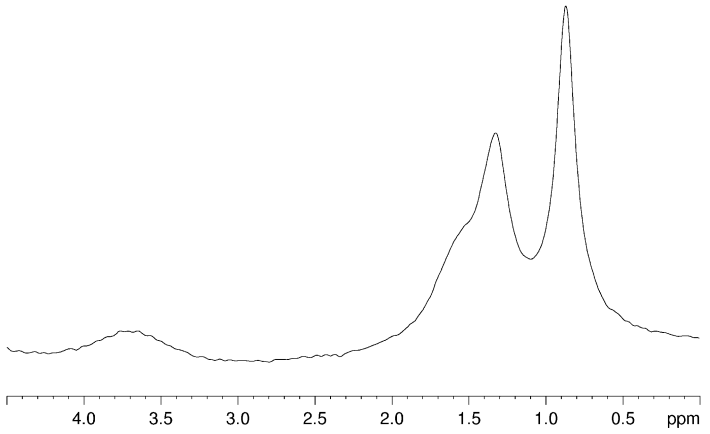

Fig. C: ^{1}H MAS NMR of the sample TiLi(5)Co(5), peaks: 0.88, 1.36, 1.61, 3.70 ppm.

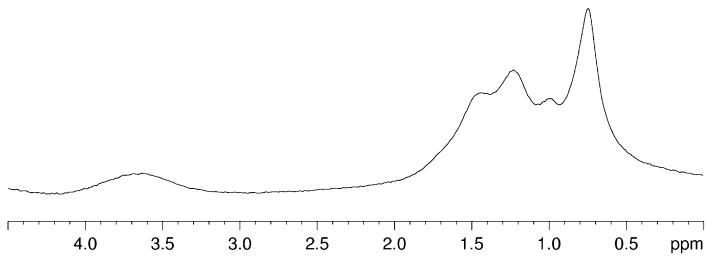

Figr. D: ^{1}H MAS NMR of the sample TiLi(5)-nanosheets, peaks: 0.77, 1.00, 1.23, 1.47, 3.74 ppm.

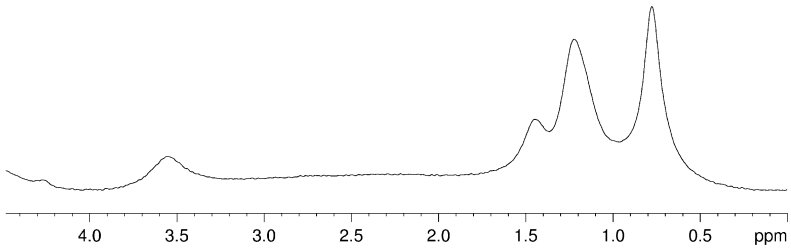

Fig. E: ^{1}H MAS NMR of the sample TiLi(5)-xerogel, peaks: 0.79, 1.23, 1.45, 3.56 ppm.

References

[1] United Nations, “World Population Prospects: The 2017 Revision, Key Findings and Advance Tables,” 2017.

[2] J. Nässén, J. Holmberg, A. Wadeskog, and M. Nyman, “Direct and indirect energy use and carbon emissions in the production phase of buildings: An input-output analysis,” *Energy*, vol. 32, no. 9, pp. 1593–1602, 2007.

[3] L. Vukotic, R. A. Fenner, and K. Symons, “Assessing embodied energy of building structural elements,” *Proc. Inst. Civ. Eng. - Eng. Sustain.*, vol. 158, no. September, pp. 147–158, 2010.

[4] E. Greco, E. Ciliberto, P. D. Verdura, E. Lo Giudice, and G. Navarra, “Nanoparticle-based concretes for the restoration of historical and contemporary buildings: a new way for CO_2 reduction in architecture,” *Appl. Phys. A Mater. Sci. Process.*, vol. 122, no. 5, 2016.

[5] K. M. Reddy, S. V. Manorama, and A. R. Reddy, “Bandgap studies on anatase

titanium dioxide nanoparticles," *Mater. Chem. Phys.*, vol. 78, no. 1, pp. 239–245, 2003.

[6] J. Bico, C. Tordeux, and D. Quéré, "Rough wetting," *Europhys. Lett.*, vol. 55, no. July, pp. 214–220, 2001.

[7] X. Du, X. Liu, H. Chen, and J. He, "Facile fabrication of raspberry-like composite nanoparticles and their application as building blocks for constructing superhydrophilic coatings," *J. Phys. Chem. C*, vol. 113, no. 21, pp. 9063–9070, 2009.

[8] Y. Chen *et al.*, "Transparent superhydrophobic/superhydrophilic coatings for self-cleaning and anti-fogging," *Appl. Phys. Lett.*, vol. 101, no. 3, pp. 7420–7426, 2012.

[9] S. Granger, A. Loukili, G. Pijaudier-Cabot, and G. Chanvillard, "Experimental characterization of the self-healing of cracks in an ultra high performance cementitious material: Mechanical tests and acoustic emission analysis," *Cem. Concr. Res.*, vol. 37, no. 4, pp. 519–527, 2007.

[10] M. Nakahata, Y. Takashima, H. Yamaguchi, and A. Harada, "Redox-responsive self-healing materials formed from host–guest polymers," *Nat. Commun.*, vol. 2, p. 511, 2011.

[11] M. Wu, B. Johannesson, and M. Geiker, "A review: Self-healing in cementitious materials and engineered cementitious composite as a self-healing material," *Constr. Build. Mater.*, vol. 28, no. 1, pp. 571–583, 2012.

[12] B. Ohtani, "Photocatalysis A to Z-What we know and what we do not know in a scientific sense," *J. Photochem. Photobiol. C Photochem. Rev.*, vol. 11, no. 4, pp. 157–178, 2010.

[13] S. G. Kumar and L. G. Devi, "Review on modified TiO_2 photocatalysis under UV/visible light: Selected results and related mechanisms on interfacial charge carrier transfer dynamics," *J. Phys. Chem. A*, vol. 115, no. 46, pp. 13211–13241, 2011.

[14] J. M. Herrmann *et al.*, "Environmental green chemistry as defined by photocatalysis," *J. Hazard. Mater.*, vol. 146, no. 3, pp. 624–629, 2007.

[15] J. H. Seinfeld and S. N. Pandis, *Atmospheric chemistry and physics from air pollution to climate change*. John Wiley & Sons, 1998.

[16] B. Ohtani, O. O. Prieto-Mahaney, D. Li, and R. Abe, "What is Degussa (Evonic) P25? Crystalline composition analysis, reconstruction from isolated pure particles and photocatalytic activity test," *J. Photochem. Photobiol. A Chem.*, vol. 216, no. 2–3, pp. 179–182, 2010.

[17] A. Plassais and L. Guillot, "De-polluting activity assessment of photocatalytic cementbased materials: from laboratory to real scale testing'," in *Tenth international symposium on concrete roads (Brussels/Belgium, 18--22 September 2006)*, 2006, p. 13.

[18] L. Cassar, "Photocatalysis of Materials : Clean Buildings and Clean Air," *MRS Bull.*, no. May 2004, pp. 328–331, 2004.

[19] F. Vallee *et al.*, "Cementitious materials for self-cleaning and de-polluting facade surfaces," in *RILEM International Symposium on Environment-Conscious Materials and Systems for Sustainable Development*, 2004, pp. 337–346.

[20] G. L. Guerrini and E. Peccati, "Photocatalytic cementitious roads for depollution," in *Int. Symp. On photocatalysis, environment and construction materials.*, 2015, pp. 179–186.

[21] T. Maggos, A. Plassais, J. G. Bartzis, C. Vasilakos, N. Moussiopoulos, and L. Bonafous, “Photocatalytic degradation of NO_x in a pilot street canyon configuration using TiO_2-mortar panels,” *Environ. Monit. Assess.*, vol. 136, no. 1–3, pp. 35–44, 2008.

[22] J. Chen and C. sun Poon, “Photocatalytic construction and building materials: From fundamentals to applications,” *Build. Environ.*, vol. 44, no. 9, pp. 1899–1906, 2009.

[23] F. Pacheco-Torgal and S. Jalali, “Nanotechnology: Advantages and drawbacks in the field of construction and building materials,” *Constr. Build. Mater.*, vol. 25, no. 2, pp. 582–590, 2011.

[24] Claus V. Nielsen and Mette Glavind, “Danish Experiences with a Decade of Green Concrete,” *J. Adv. Concr. Technol. Japan Concr. Inst.*, vol. 5, no. 1, pp. 3–12, 2007.

[25] A. Beeldens, “Air purification by road materials: results of the test project in Antwerp,” in *Int. Symp. On photocatalysis, environment and construction materials.*, 2007, pp. 187–194.

[26] L. Cassar, C. Pepe, G. P. Tognon, G. L. Guerrini, and R. Amadelli, “White cement for architectural concrete, possessing photocatalytic properties,” in *Proc. 11th Int. Congress on the Chemistry of Cement (ICCC), Vol. IV*, 2003, p. 2012.

[27] L. Cassar and C. Pepe, “Use of organic additives for the preparation of cementitious compositions with improved properties of constancy of color,” 2000.

[28] G. L. Guerrini, “Photocatalytic performances in a city tunnel in Rome: NOx monitoring results,” *Constr. Build. Mater.*, vol. 27, no. 1, pp. 165–175, 2012.

[29] European Commission, “Communication from the Commission EUROPE 2020 A strategy for smart, sustainable and inclusive growth,” *Com(2010) 2020,* no. 3 March, 2010.

[30] U. Nations, “Kyoto Protocol To the United Nations Framework Kyoto Protocol To the United Nations Framework,” *Rev. Eur. Community Int. Environ. Law*, vol. 7, pp. 214–217, 1998.

[31] UNFCCC, “Paris Agreement,” *Conf. Parties its twenty-first Sess.*, vol. 21932, no. December, p. 32, 2015.

[32] J. W. Anthony, R. a. Bideaux, K. W. Bladh, and M. C. Nichols, “Mineral Data Publishing: Anatase,” *Handb. Mineral.*, no. 2, p. 2005, 2005.

[33] J. W. Anthony, R. a. Bideaux, K. W. Bladh, and M. C. Nichols, “Rutile,” *Miner. Data Publ.*, vol. 10, no. 2, pp. 187–190, 2005.

[34] J. W. Anthony, R. a. Bideaux, K. W. Bladh, and M. C. Nichols, “Mineral Data Publishing: Brookite,” *Handb. Mineral.*, vol. 2, no. 1, pp. 16383–16383, 2005.

[35] D. A. H. Hanaor and C. C. Sorrell, “Review of the anatase to rutile phase transformation,” *J. Mater. Sci.*, vol. 46, no. 4, pp. 855–874, 2011.

[36] U. Diebold, “The surface science of titanium dioxide,” *Surf. Sci. Rep.*, vol. 48, no. 5, pp. 53–229, 2003.

[37] D. P. MacWan, P. N. Dave, and S. Chaturvedi, “A review on nano-TiO_2 sol-gel type syntheses and its applications,” *J. Mater. Sci.*, vol. 46, no. 11, pp. 3669–3686, 2011.

[38] H. M. Lu, W. X. Zhang, and Q. Jiang, “Phase Stability of Nanoanatase,” *Adv. Eng. Mater.*, vol. 5, no. 11, pp. 787–788, 2003.

[39] M. Lazzeri, A. Vittadini, and A. Selloni, “Structure and energetics of stoichiometric TiO_2 anatase surfaces,” *Phys. Rev. B - Condens. Matter Mater. Phys.*, vol. 63, no. 15, pp. 1554091–1554099, 2001.

[40] M. Stir, R. Nicula, and E. Burkel, “Pressure-temperature phase diagrams of pure and Ag-doped nanocrystalline TiO_2 photocatalysts,” *J. Eur. Ceram. Soc.*, vol. 26, no. 9, pp. 1547–1553, 2006.

[41] N. Serpone and a. V. Emeline, “Suggested terms and definitions in photocatalysis and radiocatalysis,” *Int. J. Photoenergy*, vol. 4, no. 3, pp. 91–131, 2002.

[42] U. I. Gaya and A. H. Abdullah, “Heterogeneous photocatalytic degradation of organic contaminants over titanium dioxide: A review of fundamentals, progress and problems,” *Journal of Photochemistry and Photobiology C: Photochemistry Reviews*, vol. 9, no. 1. pp. 1–12, 2008.

[43] R. Leary and A. Westwood, “Carbonaceous nanomaterials for the enhancement of TiO_2 photocatalysis,” *Carbon N. Y.*, vol. 49, no. 3, pp. 741–772, 2011.

[44] A. L. Linsebigler, A. L. Linsebigler, J. T. Yates Jr, G. Lu, G. Lu, and J. T. Yates, “Photocatalysis on TiO_2 Surfaces: Principles, Mechanisms, and Selected Results,” *Chem. Rev.*, vol. 95, no. 3, pp. 735–758, 1995.

[45] G. Liu, L. Wang, H. G. Yang, H.-M. Cheng, and G. Q. (Max) Lu, “Titania-based photocatalysts—crystal growth, doping and heterostructuring,” *J. Mater. Chem.*, vol. 20, no. 5, pp. 831–843, 2010.

[46] A. Wold, “Photocatalytic properties of titanium dioxide (TiO_2),” *Chem. Mater.*, vol. 2912, no. 16, pp. 280–283, 1993.

[47] M. Inokuti and F. Hirayama, “Influence of Energy Transfer by the Exchange Mechanism on Donor Luminescence,” *J. Chem. Phys.*, vol. 43, no. 6, p. 1978, 1965.

[48] B. Liu, X. Zhao, C. Terashima, A. Fujishima, and K. Nakata, “Thermodynamic and kinetic analysis of heterogeneous photocatalysis for semiconductor systems,” *Phys. Chem. Chem. Phys. Phys. Chem. Chem. Phys*, vol. 16, no. 16, pp. 8751–8760, 2014.

[49] X. H. Lin, Y. Miao, and S. F. Y. Li, “Location of photocatalytic oxidation processes on anatase titanium dioxide,” *Catal. Sci. Technol.*, vol. 7, no. 2, pp. 441–451, 2017.

[50] M. Krasowska, J. Zawala, and K. Malysa, “Air at hydrophobic surfaces and kinetics of three phase contact formation,” *Adv. Colloid Interface Sci.*, vol. 147–148, no. C, pp. 155–169, 2009.

[51] R. Benedix, F. Dehn, J. Quaas, and M. Orgass, “Application of titanium dioxide photocatalysis to create self-cleaning building materials,” *Lacer*, vol. 3, pp. 157–168, 2000.

[52] L. Gao and T. J. McCarthy, “The ‘lotus effect’ explained: Two reasons why two length scales of topography are important,” *Langmuir*, vol. 22, no. 7, pp. 2966–2967, 2006.

[53] A. Marmur, “The lotus effect: Superhydrophobicity and metastability,” *Langmuir*, vol. 20, no. 9, pp. 3517–3519, 2004.

[54] H. J. Lee and S. Michielsen, “Lotus effect: Superhydrophobicity,” *J. Text. Inst.*, vol. 97, no. 5, pp. 455–462, 2006.

[55] K. Sunada, Y. Kikuchi, K. Hashimoto, and A. Fujishima, “Bactericidal and Detoxification Effects of TiO_2 Thin Film Photocatalysts,” *Environ. Sci. Technol.*, vol. 32, no. January, pp. 726–728, 1998.

[56] P. Maness, S. Smolinski, D. M. Blake, Z. Huang, E. J. Wolfrum, and W. a Jacoby, “Bactericidal Activity of Photocatalytic TiO_2 Reaction : toward an Understanding of Its Killing Mechanism Bactericidal Activity of Photocatalytic TiO_2 Reaction : toward an Understanding of Its Killing Mechanism,” *Appl. Environ. Microbiol.*, vol. 65, no. 9, pp. 4094–4098, 1999.

[57] L. Zhang, R. Dillert, D. Bahnemann, and M. Vormoor, “Photo-induced hydrophilicity and self-cleaning: models and reality,” *Energy Environ. Sci.*, vol. 5, no. 6, pp. 7491–7507, 2012.

[58] J. Zhao and X. Yang, “Photocatalytic oxidation for indoor air purification: A literature review,” *Build. Environ.*, vol. 38, no. 5, pp. 645–654, 2003.

[59] C. H. Ao and S. C. Lee, “Indoor air purification by photocatalyst TiO_2 immobilized on an activated carbon filter installed in an air cleaner,” *Chem. Eng. Sci.*, vol. 60, no. 1, pp. 103–109, 2005.

[60] M. R. Hoffmann, S. Martin, W. Choi, and D. W. Bahnemann, “Environmental Applications of Semiconductor Photocatalysis,” *Chem. Rev.*, vol. 95, no. 1, pp. 69–96, 1995.

[61] A. Fujishima, T. N. Rao, and D. A. Tryk, “Titanium dioxide photocatalysis,” *J. Photochem. Photobiol. C Photochem. Rev.*, vol. 1, no. 1, pp. 1–21, 2000.

[62] T. Ueda and M. Nishimura, “Photocatalytic active carbon, colored photocatalytic active carbon, coloring active carbon, and deodorant and adsorption product using them,” 2004.

[63] K. Gupta, R. P. Singh, A. Pandey, and A. Pandey, “Photocatalytic antibacterial performance of TiO_2 and Ag-doped TiO_2 against S. Aureus. P. Aeruginosa and E. Coli,” *Beilstein J. Nanotechnol.*, vol. 4, no. 1, pp. 345–351, 2013.

[64] T. Matsunaga, R. Tomoda, T. Nakajima, and H. Wake, “Photoelectrochemical sterilization of microbial cells by semiconductor powders,” *FEMS Microbiol. Lett.*, vol. 29, no. 1, pp. 211–214, 1985.

[65] K. P. Kühn *et al.*, “Disinfection of surfaces by photocatalytic oxidation with titanium dioxide and UVA light,” *Chemosphere*, vol. 53, no. 1, pp. 71–77, 2003.

[66] R. Wang *et al.*, “Light-induced amphiphilic surfaces,” *Nature*, vol. 388, pp. 431–432, 1997.

[67] W. Y. Gan, S. W. Lam, K. Chiang, R. Amal, H. Zhao, and M. P. Brungs, “Novel TiO_2 thin film with non-UV activated superwetting and antifogging behaviours,” *J. Mater. Chem.*, vol. 17, no. 10, pp. 952–954, 2007.

[68] Z. Zhang, X. Zhong, S. Liu, D. Li, and M. Han, “Aminolysis route to monodisperse titania nanorods with tunable aspect ratio,” *Angew. Chemie - Int. Ed.*, vol. 44, no. 22, pp. 3466–3470, 2005.

[69] X. Yan *et al.*, “Controllable synthesis and photocatalytic activities of water-soluble TiO_2 nanoparticles,” *Mater. Lett.*, vol. 64, no. 16, pp. 1833–1835, 2010.

[70] H. Choi, E. Stathatos, and D. D. Dionysiou, “Synthesis of nanocrystalline photocatalytic TiO_2 thin films and particles using sol-gel method modified with nonionic surfactants,” *Thin Solid Films*, vol. 510, no. 1–2, pp. 107–114, 2006.

[71] H. Choi, Y. J. Kim, R. S. Varma, and D. D. Dionysiou, “Thermally stable nanocrystalline TiO_2 photocatalysts synthesized via sol-gel methods modified

with ionic liquid and surfactant molecules," *Chem. Mater.*, vol. 18, no. 22, pp. 5377–5384, 2006.

[72] T. Sreethawong and S. Yoshikawa, "Enhanced photocatalytic hydrogen evolution over Pt supported on mesoporous TiO_2 prepared by single-step sol-gel process with surfactant template," *Int. J. Hydrogen Energy*, vol. 31, no. 6, pp. 786–796, 2006.

[73] X. Chen and S. S. Mao, "Titanium dioxide nanomaterials: Synthesis, properties, modifications and applications," *Chem. Rev.*, vol. 107, no. 7, pp. 2891–2959, 2007.

[74] N. Kopidakis, N. R. Neale, and A. J. Frank, "Effect of an Adsorbent on Recombination and Band-Edge Movement in Dye-Sensitized TiO_2 Solar Cells: Evidence for Surface Passivation," *J. Phys. Chem. B*, vol. 110, no. 25, pp. 12485–12489, 2006.

[75] D. J. Kim, S. H. Hahn, S. H. Oh, and E. J. Kim, "Influence of calcination temperature on structural and optical properties of TiO_2 thin films prepared by sol-gel dip coating," *Mater. Lett.*, vol. 57, no. 2, pp. 355–360, 2002.

[76] S. Musić *et al.*, "Chemical and micro structural properties of TiO_2 synthesized by sol-gel procedure," *Mater. Sci. Eng. B*, vol. 47, no. 1, pp. 33–40, 1997.

[77] Y. F. Zhu, L. Zhang, C. Gao, and L. L. Cao, "The synthesis of nanosized TiO_2 powder using a sol-gel method with $TiCl_4$ as a precursor," *J. Mater. Sci.*, vol. 35, no. 16, pp. 4049–4054, 2000.

[78] J. Jing, J. Feng, W. Li, and W. W. Yu, "Low-temperature synthesis of water-dispersible anatase titanium dioxide nanoparticles for photocatalysis," *J. Colloid Interface Sci.*, vol. 396, pp. 90–94, 2013.

[79] J. Livage, C. Sanchez, M. Henry, and S. Doeuff, “The chemistry of the sol-gel process,” *Solid State Ionics*, vol. 32–33, no. PART 2, pp. 633–638, 1989.

[80] F. Sayilkan and M. Asilturk, “Characterization of TiO_2 Synthesized in Alcohol by a Sol-Gel Process: The Effects of Annealing Temperature and Acid Catalyst,” *Turkish J. …*, vol. 29, no. 2005, pp. 697–706, 2005.

[81] C. Brinker and G. Scherer, “Sol-Gel Science: The Physics and Chemistry of Sol-Gel Processing,” *Advanced Materials*, vol. 3, no. 10. p. 912, 1990.

[82] L. L. Hench and J. K. West, “The sol-gel process,” *Chem. Rev.*, vol. 90, no. 1, pp. 33–72, 1990.

[83] E. Gallegos-Suárez, A. F. Pérez-Cadenas, F. J. Maldonado-Hódar, and F. Carrasco-Marín, “On the micro- and mesoporosity of carbon aerogels and xerogels. The role of the drying conditions during the synthesis processes,” *Chem. Eng. J.*, vol. 181–182, pp. 851–855, 2012.

[84] R. Wu, Y. Wei, and Y. Zhang, “Preparation of nanosized TiO_2 particles by forced hydrolysis from titanium salt,” *Mater. Res. Bull.*, vol. 34, no. 14, pp. 2131–2135, 1999.

[85] E. Greco, E. Ciliberto, A. M. E. Cirino, D. Capitani, and V. Di Tullio, “A new preparation of doped photocatalytic TiO_2 anatase nanoparticles: a preliminary study for the removal of pollutants in confined museum areas,” *Appl. Phys. A Mater. Sci. Process.*, vol. 122, no. 5, 2016.

[86] C. Burda, Y. Lou, X. Chen, A. C. S. Samia, J. Stout, and J. L. Gole, “Enhanced Nitrogen Doping in TiO_2 Nanoparticles,” *Nano Lett.*, vol. 3, pp. 1049–1051, 2003.

[87] W. Y. Choi, A. Termin, and M. R. Hoffmann, “The Role of Metal-Ion Dopants in

Quantum-Sized TiO_2 - Correlation between Photoreactivity and Charge-Carrier Recombination Dynamics," *J. Phys. Chem.*, vol. 98, no. 51, pp. 13669–13679, 1994.

[88] O. Diwald and T. Thompson, "The effect of nitrogen ion implantation on the photoactivity of TiO_2 rutile single crystals," *J. …*, vol. 108, no. 1, pp. 52–57, 2004.

[89] M. A. Fox and M. T. Dulay, "Heterogeneous photocatalysis," *Chem. Rev.*, vol. 93, no. 1, pp. 341–357, 1993.

[90] B. Xin, Z. Ren, P. Wang, J. Liu, L. Jing, and H. Fu, "Study on the mechanisms of photoinduced carriers separation and recombination for Fe^{3+}-TiO_2 photocatalysts," *Appl. Surf. Sci.*, vol. 253, no. 9, pp. 4390–4395, 2007.

[91] M. Gratzel and R. F. Howe, "Electron paramagnetic resonance studies of doped TiO_2 colloids," *J. Phys. Chem.*, vol. 94, no. 7, pp. 2566–2572, 1990.

[92] J. Soria, J. C. Conesa, V. Augugliaro, L. Palmisano, M. Schiavello, and A. Sclafani, "Dinitrogen photoreduction to ammonia over titanium dioxide powders doped with ferric ions," *J. Phys. Chem.*, vol. 95, no. 1, pp. 274–282, 1991.

[93] Z. Luo and Q.-H. Gao, "Decrease in the photoactivity doping with transition metals of TiO_2 pigment on metals," *J. Photochem. Photobiol. A Chem.*, vol. 63, pp. 367–375, 1992.

[94] W. Mu, J. M. Herrmann, and P. Pichat, "Room temperature photocatalytic oxidation of liquid cyclohexane into cyclohexanone over neat and modified TiO_2," *Catal. Letters*, vol. 3, no. 1, pp. 73–84, 1989.

[95] K. Mizushima, M. Tanaka, and S. Iida, "Energy Levels of Iron Group Impurities in TiO2," *J. Phys. Soc. Japan*, vol. 32, no. 6, pp. 1519–1524, 1972.

[96] K. Mizushima, M. Tanaka, A. Asai, S. Iida, and J. B. Goodenough, “Impurity levels of iron-group ions in TiO_2(II),” *J. Phys. Chem. Solids*, vol. 40, no. 12, pp. 1129–1140, 1979.

[97] P. Triggs, “Electronic and structural properties of single crystals in the system TiO_2-RuO_2,” *Helv. Phys. Acta*, vol. 58, pp. 657–714, 1985.

[98] M. Gratzel, *Energy resources through photochemistry and catalysis*. Elsevier, 2012.

[99] J. Gautron, P. Lemasson, and J.-F. Marucco, “Correlation between the non-stoichiometry of titanium dioxide and its photoelectrochemical behaviour,” *Faraday Discuss. Chem. Soc.*, vol. 70, p. 81, 1980.

[100] L. Brus, “Electronic wave functions in semiconductor clusters: experiment and theory,” *J. Phys. Chem.*, vol. 90, no. 12, pp. 2555–2560, 1986.

[101] U. Kölle, J. Moser, M. Graetzel, U. Koelle, M. Jacques, and M. Graetzel, “Dynamics of interfacial charge-transfer reactions in semiconductor dispersions. Reduction of cobaltoceniumdicarboxylate in colloidal titania,” *Inorg. Chem.*, vol. 24, no. 14, pp. 2253–2258, 1985.

[102] D. Bahnemann, A. Henglein, J. Lilie, and L. Spanhel, “Flash photolysis observation of the absorption spectra of trapped positive holes and electrons in colloidal titanium dioxide,” *J. Phys. Chem.*, vol. 88, no. 4, pp. 709–711, 1984.

[103] G. Rothenberger, J. Moser, M. Gratzel, N. Serpone, and D. K. Sharma, “Charge carrier trapping and recombination dynamics in small semiconductor particles,” *J. Am. Chem. Soc.*, vol. 107, no. 26, pp. 8054–8059, 1985.

[104] J. Moser, M. Grätzel, and R. Gallay, “Inhibition of Electron-Hole Recombination

in Substitutionally Doped Colloidal Semiconductor Crystallites," *Helv. Chim. Acta*, vol. 70, no. 6, pp. 1596–1604, 1987.

[105] Y. Matsumoto, M. Murakami, and T. Shono, "Room-Temperature Ferromagnetism in Transparent Transition Metal – Doped Titanium Dioxide," *Science (80-.).*, vol. 854, pp. 854–857, 2001.

[106] M. Bellardita, M. Addamo, A. Di Paola, and L. Palmisano, "Photocatalytic behaviour of metal-loaded TiO_2 aqueous dispersions and films," *Chem. Phys.*, vol. 339, no. 1–3, pp. 94–103, 2007.

[107] S. M. Gupta and M. Tripathi, "A review of TiO_2 nanoparticles," *Chinese Sci. Bull.*, vol. 56, no. 16, pp. 1639–1657, 2011.

[108] P. Yang, C. Lu, N. Hua, and Y. Du, "Titanium dioxide nanoparticles co-doped with Fe^{3+} and Eu^{3+} ions for photocatalysis," *Mater. Lett.*, vol. 57, no. 4, pp. 794–801, 2002.

[109] P. H. J. Turkevich, John; Cooper, "A study of the nucleation and growth process in the synthesis of colloidal gold," *Discuss. Faraday Soc.*, vol. 55, no. c, pp. 55–75, 1951.

[110] G. Frens, "Controlled Nucleation for the Regulation of the Particle Size in Monodisperse Gold Suspensions," *Nat. Phys. Sci.*, vol. 241, no. 105, pp. 20–22, 1973.

[111] X. Ji, X. Song, J. Li, Y. Bai, W. Yang, and X. Peng, "Size control of gold nanocrystals in citrate reduction: The third role of citrate," *J. Am. Chem. Soc.*, vol. 129, no. 45, pp. 13939–13948, 2007.

[112] I. Ojea-Jiménez and J. Campanera, "Molecular modeling of the reduction

mechanism in the citrate-mediated synthesis of gold nanoparticles," *J. Phys. Chem. C*, vol. 116, pp. 23682–23691, 2012.

[113] N. G. Bastús, J. Comenge, and V. Puntes, "Kinetically controlled seeded growth synthesis of citrate-stabilized gold nanoparticles of up to 200 nm: Size focusing versus ostwald ripening," *Langmuir*, vol. 27, no. 17, pp. 11098–11105, 2011.

[114] W. Haiss, N. T. K. Thanh, J. Aveyard, and D. G. Fernig, "Determination of size and concentration of gold nanoparticles from UV-Vis spectra," *Anal. Chem.*, vol. 79, no. 11, pp. 4215–4221, 2007.

[115] V. Štengl, S. Bakardjieva, J. Šubrt, and L. Szatmary, "Titania aerogel prepared by low temperature supercritical drying," *Microporous Mesoporous Mater.*, vol. 91, no. 1–3, pp. 1–6, 2006.

[116] J. Wang *et al.*, "Heat treatment of nanometer anatase powder and its photocatalytic activity for degradation of acid red B dye under visible light irradiation," *Inorg. Mater.*, vol. 44, no. 6, pp. 608–614, 2008.

[117] S. Brunauer, P. H. Emmett, and E. Teller, "Adsorption of Gases in Multimolecular Layers," *J. Am. Chem. Soc.*, vol. 60, no. 1, pp. 309–319, 1938.

[118] G. Pickett, "Modification of the Brunauer Emmett Teller Theory of Multimolecular Adsorption," *J. Am. Chem. Soc.*, vol. 67, no. 11, pp. 1958–1962, 1945.

[119] R. B. Anderson, "Modifications of the Brunauer, Emmett and Teller equation.," *J. Am. Chem. Soc.*, vol. 70, no. 5, pp. 1727–1734, 1948.

[120] L. D. Gelb and K. E. Gubbins, "Characterization of Porous Glasses: Simulation Models, Adsorption Isotherms, and the Brunauer-Emmett-Teller Analysis

Method," *Langmuir*, vol. 14, no. 8, pp. 2097–2111, 1998.

[121] E. P. Barrett, L. G. Joyner, and P. P. Halenda, "The determination of pore volume and area distributions in porous substances. I. computations from nitrogen isotherms," *J. Am. Chem. Soc.*, vol. 73, no. 1, pp. 373–380, 1951.

[122] P. Scherrer, "Bestimmung der Grosse und der inneren Struktur von Kolloidteilchen mittels Rontgenstrahlen," *Nachrichten von der Gesellschaft der Wissenschaften zu Gottingen, Math. Klasse*, vol. 1918, pp. 98–100, 1918.

[123] A. Monshi, M. R. Foroughi, and M. R. Monshi, "Modified Scherrer equation to estimate more accurately nano-crystallite size using XRD," *World J. Nano Sci. Eng.*, vol. 2, no. 3, p. 154, 2012.

[124] J. B. Condon, *Surface Area and porosity Determinations bu Phisisortion, measurements and Theory*, vol. 53, no. 9. 2013.

[125] S. Lowell, J. E. Shields, M. A. Thomas, and M. Thommes, *Characterization of porous solids and powders: surface area, pore size and density*. 2004.

[126] R. J. Hunter, *Zeta potential in colloid science: principles and applications*, vol. 2. Academic press, 2013.

[127] B. Derjaguin and L. Landau, "Theory of the stability of strongly charged lyophobic sols and of the adhesion of strongly charged particles in solution of eletrolytes.," *Acta Physicochim. URSS*, vol. 14, pp. 633–662, 1941.

[128] E. J. W. Verwey, J. T. G. Overbeek, and J. T. G. Overbeek, *Theory of the stability of lyophobic colloids*. Courier Corporation, 1999.

[129] J. A. V. BUTLER, "Theory of the Stability of Lyophobic Colloids," *Nature*, vol. 162, no. 4113, pp. 315–316, 1948.

[130] D. Lin, X. Tian, F. Wu, and B. Xing, “Fate and transport of engineered nanomaterials in the environment.,” *J. Environ. Qual.*, vol. 39, no. 6, pp. 1896–1908, 2010.

[131] K. Bourikas, T. Hiemstra, and W. H. Van Riemsdijk, “Ion pair formation and primary charging behavior of titanium oxide (anatase and rutile),” *Langmuir*, vol. 17, no. 3, pp. 749–756, 2001.

[132] G. Xu, J. Zhang, G. Li, and G. Song, “Effect of complexation on the zeta potential of titanium dioxide dispersions,” *J. Dispers. Sci. Technol.*, vol. 24, no. 3–4, pp. 527–535, 2003.

[133] J. Davis, R. James, and J. Leckie, “Surface ionization and complexation at the oxide / water interface I. Computation of electrical double layer properties in simple electrolytes,” *J. Colloid Interface Sci.*, vol. 63, no. 3, pp. 480–499, 1978.

[134] T. C. Farrar and E. D. Becker, *Pulse and Fourier Transform NMR*, 1st ed. New York: Academic Press, 1971.

[135] F. H. Larsen, H. J. Jakobsen, P. D. Ellis, and N. C. Nielsen, “Sensitivity-Enhanced Quadrupolar-Echo NMR of Half-Integer Quadrupolar Nuclei. Magnitudes and Relative Orientation of Chemical Shielding and Quadrupolar Coupling Tensors,” *J. Phys. Chem. A*, vol. 101, no. 46, pp. 8597–8606, 1997.

[136] P. Kubelka and F. Munk, “An Article on Optics of Paint Layers (engl. Übersetzung),” *Z. Tech. Phys*, vol. 12, no. 1930, pp. 593–601, 1931.

[137] R. Wang *et al.*, “Photogeneration of Highly Amphiphilic TiO_2 Surfaces ,” *Adv. Mater.*, vol. 10, no. 2, pp. 135–138, 1998.

[138] R. Wang, N. Sakai, a Fujishima, T. Watanabe, and K. Hashimoto, “Studies of

surface wettability conversion on TiO_2 single-crystal surfaces," *J. Phys. Chem. B*, vol. 103, no. 12, pp. 2188–2194, 1999.

[139] Y. Gao, Y. Masuda, and K. Koumoto, "Light-Excited Superhydrophilicity of Amorphous TiO_2 Thin Films Deposited in an Aqueous Peroxotitanate Solution," *Langmuir*, vol. 20, no. 8, pp. 3188–3194, 2004.

[140] E. Hosono, H. Matsuda, I. Honma, M. Ichihara, and H. Zhou, "Synthesis of a perpendicular TiO_2 nanosheet film with the superhydrophilic property without UV irradiation," *Langmuir*, vol. 23, no. 14, pp. 7447–7450, 2007.

[141] J. Liggio, S. M. Li, and R. McLaren, "Reactive uptake of glyoxal by particulate matter," *J. Geophys. Res. D Atmos.*, vol. 110, no. 10, pp. 1–13, 2005.

[142] M. Possanzini, V. Di Palo, and A. Cecinato, "Sources and photodecomposition of formaldehyde and acetaldehyde in Rome ambient air," *Atmos. Environ.*, vol. 36, no. 19, pp. 3195–3201, 2002.

[143] Y. Liu *et al.*, "Impact of pollution controls in Beijing on atmospheric oxygenated volatile organic compounds (OVOCs) during the 2008 olympic games: Observation and modeling implications," *Atmos. Chem. Phys.*, vol. 15, no. 6, pp. 3045–3062, 2015.

[144] J. T. Jayne, D. R. Worsnop, C. E. Kolb, E. Swartz, and P. Davidovits, "Uptake of Gas-Phase Formaldehyde by Aqueous Acid Surfaces," *J. Phys. Chem.*, vol. 100, no. 95, pp. 8015–8022, 1996.

[145] L. T. Iraci and M. A. Tolbert, "Heterogeneous interaction of formaldehyde with cold sulfuric acid: Implications for the upper troposphere and lower stratosphere," *J. Geophys. Res. Atmos.*, vol. 102, no. D13, pp. 16099–16107, 1997.

[146] S. Carlos-Cuellar, P. Li, A. P. Christensen, B. J. Krueger, C. Burrichter, and V. H. Grassian, “Heterogeneous uptake kinetics of volatile organic compounds on oxide surfaces using a Knudsen cell reactor: Adsorption of acetic acid, formaldehyde, and methanol on Fe_2O_3, Al_2O_3, and SiO_2,” *J. Phys. Chem. A*, vol. 107, no. 21, pp. 4250–4261, 2003.

[147] B. Xu, J. Shang, T. Zhu, and X. Tang, “Heterogeneous reaction of formaldehyde on the surface of gamma-Al_2O_3 particles,” *Atmos. Environ.*, vol. 45, no. 21, pp. 3569–3575, 2011.

[148] C. D. Hatch, R. V Gough, and M. A. Tolbert, “Heterogeneous uptake of the C 1 to C 4 organic acids on a swelling clay mineral,” *Atmos. Chem. Phys.*, vol. 7, pp. 4445–4458, 2007.

[149] M. Sassine, L. Burel, B. D’Anna, and C. George, “Kinetics of the tropospheric formaldehyde loss onto mineral dust and urban surfaces,” *Atmos. Environ.*, vol. 44, no. 40, pp. 5468–5475, 2010.

[150] Z. Li, A. N. Schwier, N. Sareen, and V. F. McNeill, “Reactive processing of formaldehyde and acetaldehyde in aqueous aerosol mimics: Surface tension depression and secondary organic products,” *Atmos. Chem. Phys.*, vol. 11, no. 22, pp. 11617–11629, 2011.

[151] X. Shen, Y. Zhao, Z. Chen, and D. Huang, “Heterogeneous reactions of volatile organic compounds in the atmosphere,” *Atmos. Environ.*, vol. 68, pp. 297–314, 2013.

[152] Y. Chen, J. Liu, J. Shang, and T. Zhu, “Simulated reaction of formaldehyde and ambient atmospheric particulate matter using a chamber,” *J. Environ. Sci. (China)*, vol. 56, pp. 45–51, 2017.

[153] P. Bisgaard, M. Lars, B. Rietz, and P. Wilhardt, “Quantitative Determination of Formaldehyde In Air Using the Acetylacetone Method,” *Anal. Lett.*, vol. 16, no. 17,18, pp. 1457–1468, 1983.

[154] X. D. Wu, S. G. Liu, Y. Z. Liang, and X. J. Gong, “Study on the product for the determination of formaldehyde with acetylacetone,” *Chinese J. Anal. Chem.*, vol. 30, no. 12, pp. 1463–1465, 2002.

[155] I.-S. Kim, M. Baek, and S.-J. Choi, “Comparative Cytotoxicity of Al_2O_3 , CeO_2 , TiO_2 and ZnO Nanoparticles to Human Lung Cells,” *J. Nanosci. Nanotechnol.*, vol. 10, no. 5, pp. 3453–3458, 2010.

[156] G. Oberdörster *et al.*, “Acute pulmonary effects of ultrafine particles in rats and mice.,” *Res. Rep. Health. Eff. Inst.*, no. 96, pp. 5–74, 2000.

[157] D. B. Warheit, T. R. Webb, C. M. Sayes, V. L. Colvin, and K. L. Reed, “Pulmonary instillation studies with nanoscale TiO_2 rods and dots in rats: Toxicity is not dependent upon particle size and surface area,” *Toxicol. Sci.*, vol. 91, no. 1, pp. 227–236, 2006.

[158] R. Duffin, L. Tran, D. Brown, V. Stone, and K. Donaldson, “Proinflammogenic effects of low-toxicity and metal nanoparticles in vivo and in vitro: highlighting the role of particle surface area and surface reactivity.,” *Inhal. Toxicol.*, vol. 19, no. 10, pp. 849–856, 2007.

[159] K. P. Lee, H. J. Trochimowicz, and C. F. Reinhardt, “Pulmonary Response of Rats Exposed to Titanium by Inhalation for Two Years Dioxide (TiO_2),” *Toxicol. Appl. Pharmacol.*, vol. 79, pp. 179–192, 1985.

[160] H. A. Jeng and J. Swanson, “Toxicity of metal oxide nanoparticles in mammalian cells,” *J Env. Sci Heal. A Tox Hazard Subst Env. Eng*, vol. 41, no. 12, pp. 2699–

2711, 2006.

[161] A. V. Peskin and C. C. Winterbourn, “A microtiter plate assay for superoxide dismutase using a water-soluble tetrazolium salt (WST-1),” *Clin. Chim. Acta*, vol. 293, no. 1–2, pp. 157–166, 2000.

[162] M. V. Berridge, P. M. Herst, and A. S. Tan, “Tetrazolium dyes as tools in cell biology: New insights into their cellular reduction,” *Biotechnol. Annu. Rev.*, vol. 11, no. SUPPL., pp. 127–152, 2005.

[163] A. R. Johnsen, K. Bendixen, and U. Karlson, “Detection of Microbial Growth on Polycyclic Aromatic Hydrocarbons in Microtiter Plates by Using the Respiration Indicator WST-1.,” *Appl. Environ. Microbiol.*, vol. 68, no. 6, p. 2683–2689., 2002.

[164] D. B. Mitchell, K. S. Santone, and D. Acosta, “Evaluation of cytotoxicity in cultured cells by enzyme leakage,” *J. Tissue Cult. Methods*, vol. 6, no. 3–4, pp. 113–116, 1980.

[165] X. Huang, I. H. El-Sayed, X. Yi, and M. A. El-Sayed, “Gold nanoparticles: Catalyst for the oxidation of NADH to NAD^+,” *J. Photochem. Photobiol. B Biol.*, vol. 81, no. 2, pp. 76–83, 2005.

[166] K. Hikosaka, J. Kim, M. Kajita, A. Kanayama, and Y. Miyamoto, “Platinum nanoparticles have an activity similar to mitochondrial NADH:ubiquinone oxidoreductase,” *Colloids Surfaces B Biointerfaces*, vol. 66, no. 2, pp. 195–200, 2008.

[167] S. S. Karajanagi, A. A. Vertegel, R. S. Kane, and J. S. Dordick, “Structure and function of enzymes adsorbed onto single-walled carbon nanotubes,” *Langmuir*, vol. 20, no. 26, pp. 11594–11599, 2004.

[168] T. Cedervall *et al.*, “Detailed identification of plasma proteins adsorbed on copolymer nanoparticles,” *Angew. Chemie - Int. Ed.*, vol. 46, no. 30, pp. 5754–5756, 2007.

[169] S. Linse *et al.*, “Nucleation of protein fibrillation by nanoparticles.,” *Proc. Natl. Acad. Sci. U. S. A.*, vol. 104, no. 21, pp. 8691–8696, 2007.

[170] X. Han *et al.*, “Validation of an LDH assay for assessing nanoparticle toxicity,” *Toxicology*, vol. 287, no. 1–3, pp. 99–104, 2011.

[171] Y. P. Zhang, A. P., Sun, “Photocatalytic killing effect of TiO_2 nanoparticles on Ls-174-t human colon carcinoma cells,” *World J. Gastroenterol.*, vol. 21, no. 10, pp. 3191–3193, 2004.

[172] Thermo Scientific, “Pierce LDH Cytotoxicity Assay Kit,” vol. 747, no. 88953, p. 7, 2016.

[173] D. Y. Lyon, L. Brunet, G. W. Hinkal, M. R. Wiesner, and P. J. J. Alvarez, “Antibacterial activity of fullerene water suspensions (nC60) is not due to ROS-mediated damage,” *Nano Lett.*, vol. 8, no. 5, pp. 1539–1543, 2008.

[174] A. Kumar, A. K. Pandey, S. S. Singh, R. Shanker, and A. Dhawan, “Engineered ZnO and TiO_2 nanoparticles induce oxidative stress and DNA damage leading to reduced viability of Escherichia coli,” *Free Radic. Biol. Med.*, vol. 51, no. 10, pp. 1872–1881, 2011.

[175] J. Zielonka, T. Sarna, J. E. Roberts, J. F. Wishart, and B. Kalyanaraman, “Pulse radiolysis and steady-state analyses of the reaction between hydroethidine and superoxide and other oxidants,” *Arch. Biochem. Biophys.*, vol. 456, 39–47, 2006.

Acknowledgements

Firstly, I would like to express my sincere gratitude to my supervisor Prof. Enrico Ciliberto for the continuous support of my PhD study and related research, for his patience, motivation, and immense knowledge. His guidance helped me in all the time of research and writing of this thesis. I could not have imagined having a better advisor and mentor for my PhD study and for my life.

Besides my supervisor, I would like to thank my PhD coordinator Prof. Salvatore Sortino and the director of the department of Chemical Sciences of University of Catania Prof. Roberto Purrello. I thank Prof. Örjan Hansson (University of Gothenburg, Sweden) for his mid-term thesis review. A special thank is reserved for my thesis

reviewers: Prof. Geoffrey Allen (University of Bristol, UK), Prof. Renzo Bertoncello (University of Padua, Italy), Prof. Abdessadek Lachgar (Wake Forest University, US), Prof. Jing Shang (Peking University, China), and Prof. Stéphane Viel (Aix-Marseille University, France) for their insightful comments and encouragements, but also for the hard questions which incented me to widen my research from various perspectives.

My sincere thanks also goes Dr. Donatella Capitani and Dr. Valeria Di Tullio (CNR-IMC, Italy), Prof. Stéphane Viel and Dr. Fabio Ziarelli (Aix-Marseille University and CNRS, France), to Prof. Jing Shang and her research group (Peking University, China), and Prof. Ioannis Gelis and Prof. Davide Tanasi and all the USF people (University of South Florida, US) who provided me excellent opportunities to join their team as visiting PhD candidate, and who gave me access to the laboratory and research facilities. Without they precious support it would not be possible to conduct this research.

I also thank Prof. Giuseppe Compagnini, Prof. Giuseppe Maccarrone, Prof. Paolo Mazzoleni, and Dr. Giulia Malaguarnera (University of Catania), Dr. Domenico Mello and Dr. Ezio Viscuso (ST

Microelectronics, Catania) for their help in the use of some facilities, to set-up specific syntheses and in the statistical data treatment.

I am also thankful to Aurélien Tafani, Brittany Schaum, Lawrence M. Shaw, and Stephan Hassam for their precious help in the linguistic revision of the thesis.

A special mention is for Ms. Sabrina Tosto for her precious skills to organize all our activities and solve our bureaucratic issues.

I thank my fellow labmates, colleagues and friends for the stimulating discussions, for the sleepless nights we were working together before deadlines, and for all the fun we have had in the last three years, in particular: my collaborators that worked in this project Antonio M.E. Cirino, Andrea S. Balsamo and James Romeo; all the colleagues of the PhD course in Chemical Sciences of University of Catania, especially the XXX cycle Francesca Nicoletta, Roberto Fiorenza, Luana Pulvirenti and Marta Perez Lloret; the 'Pulmino' team Maria Grazia Greco, Ivana Di Bari, Brunella Capace and Fabiana Cairone I will miss all the wasted time in the traffic jams with them every morning; the big family of ADI Catania and in particular the directors committee (Carmela Bonaccorso, Giulia Malaguarnera, Carlo Castruccio Castracani, Giancarlo Spedalieri and

Nadia Giuffrida) which I had the honor to chairing for more than one year; the ‘Egyptian team’ including Prof. Filippo Stanco, Dr. Ezio Viscuso, Dr. Maha Ahmed Alì and all the guys of the UNICT-Helwan Master course; Stefania Vitale, Emanuele A. Zappalà, Filippo L.M. Milotta, Gianpiero Caso, Aurélien Tafani, Brittany Schaum, Francesca Nicoletta and Alessandra Cunsolo for our adventures around the United States, Chao Huang, Xiang Feng, Yueyue Chen, Tingting Xing, Xuejiao Wang, Federica Busana, Giada Massimino, Giulia Manitta, Bernd Kroell for having made me discover China and making me fall in love with that part of the world; Alessandra Salomone, Fabrizio Schirru and all the other friends around the world who have made these years unforgettable and full of experiences that have changed my life forever.

Last but not the least, I would like to thank my family: my parents, my parents in law, my sister for supporting me, and especially my life partner Antonella Chiarandà for her patience and her love.